THE ROLE OF MAGNETIC FIELDS IN STAR FORMATION, FROM CLOUD TO DISK SCALES

Renato Mazzei
Londonderry, NH (9 years) → Ashburn, VA (9 years)→ Charlottesville, VA (11 years)

B.S. Astronomy-Physics, University of Virginia, 2017
M.S. Astronomy, University of Virginia, 2018

A Dissertation Presented to the
Graduate Faculty of the
University of Virginia
in Candidacy for the Degree of
Doctor of Philosophy

Department of Astronomy

University of Virginia
May 2024

Committee Members:
Zhi-Yun Li
L. Ilsedore Cleeves
Crystal Brogan
Ajay Limaye
Laura Fissel

ABSTRACT

In this thesis I present three works concerning the modeling of polarized emission in star forming environments. Apropos to the thesis title, each of these projects focuses on a different physical scale, spanning the range from a molecular cloud (∼5 pc), to Class 0/I disk-envelope systems (∼1000+ au), to a Class II evolved protoplanetary disk (∼200 au). In each project I develop a model for the 3-dimensional physical environment of interest, either through analytic modeling or with magnetohydrodynamic (MHD) simulations, then use radiative transfer software to simulate emission that an observer would see from a detector placed some appropriate distance away from the source.

In Chapter 1, I provide a concise summary of the astrophysical picture of star formation theory. I also discuss some of the key physics behind the magnetohydrodynamics that underpin the simulation work that was used as the basis for many of my synthetic observations. I then go on to introduce the observational techniques that are used to probe magnetic fields, with particular focus on the methods modeled in my thesis. This includes linearly polarized far-infrared and (sub)millimter emission from dust grains that align orthogonal to the magnetic field and the circularly polarized line emission that arises from the splitting of energy levels (i.e., the Zeeman Effect) for some molecular species in the presence of a magnetic field. To provide observational context, this is followed by a brief introduction to several observing facilities that have been used to study polarization in star forming environments. Finally, I describe the general modeling approach and workflow that I use for each of my projects.

In Chapter 2, I present modeled results for Zeeman Effect observations of a typical protoplanetary disk. First we construct an analytic 3D disk model based on AS 209, a typical nearby Class II disk with known emission of cyanide (CN, a molecular species that is sensitive to the Zeeman Effect). We then use the POLARIS radiative transfer code to produce synthetic circular polarization observations for several disk setups and observational scenarios to test how different parameterizations affect the results. We find that different magnetic field configurations (e.g., purely vertical versus purely toroidal) are distinguishable based on the morphology of the circularly polarized emission. Spatially resolved Stokes V channel maps are particularly useful for this purpose. We also note that the traditional method for inferring magnetic field strength from Zeeman observations, by fitting the Stokes V signal to the derivative of the Stokes I, should be approached with caution in protoplanetary disk environments due to substructure in the magnetic field. This work was in part motivated by the newly available circular polarization mode on the Atacama Large Millimeter/submillimeter Array (ALMA), so we also beam convolve our results to offer a more direct comparison with anticipated data.

In Chapter 3, I present molecular cloud scale linear polarization modeling work that I performed in collaboration with the Balloon-borne Large-Aperture Submillimeter Telescope (BLAST) team. We compare the orientation of magnetic field structure as inferred from synthetic dust polarization with the orientation of molecular gas structure inferred from radiative transfer simulations of rotational line emission in 3-dimensional, turbulent collapsing-cloud MHD simulations. To quantitatively compare the results for each of the nine molecular tracers we simulated, we apply the histogram of relative orientations (HRO) technique. We then beam convolve our results and compare with observational work done by the BLAST team of the Vela C molecular cloud. Our simulated HROs suggest that Vela C data are consistent with a dynamically important magnetic field.

In Chapter 4, I present more Zeeman Effect CN modeling, this time using MHD models of the envelope of a stellar mass protostar and a massive protostar. One of the principal conclusions of our disk-scale Zeeman work (Chapter 2 of this thesis) is that toroidal magnetic substructure in the disk can significantly reduce the intensity of the circularly polarized emission due to cancellation in the line-of-sight component of the magnetic field. This is liable to make the task of detecting disk-scale Zeeman emission with current instruments (i.e., ALMA) a very difficult enterprise. However, in the envelopes of younger (Class 0/I) sources we expect the magnetic field to perhaps be more uniform, subverting this complication. In this work we find that, indeed, the envelopes of our simulated disk-envelope systems have more favorable conditions for producing detectable emission with fractional polarization above the nominal 1.8% limit of the ALMA circular polarimeter. This suggests that Zeeman programs that target the envelopes of deeply-embedded sources, especially those with known CN emission, can be a fruitful way to access magnetic field information in young stellar objects.

In Chapter 5, I give a short summary of the thesis as a whole and discuss some potential related avenues for future study.

ACKNOWLEDGEMENTS

First, to my parents. Without them I never would have been here. The mid 90s were a wild time!

Second, to everyone I work with. Without them I never would have gotten this far. Li, Ilse, Laura, and Che-Yu, thanks for being supportive, caring, and understanding advisors and collaborators. Thanks for giving me lots of great ideas and helping me learn how to be a professional astronomer! And thanks to Crystal for helping keep me on track at all those committee meetings.

Third, to my friends. Without them I would have left a long time ago...

To Nick, Daniel, Hannah, Bri, Samer ($\frac{1}{2}$), Abby, and Andy (and Molly and Xiaoshan...what year am I again?) — thanks for helping me get through grad school, and just generally being a great cohort to hang out with! Thanks for the potlucks. And the corn dog nights. And the late nights at Nelly's. Shoutout to Mango Cart.

To Bruce — thanks for the $3. Sorry about the jalapeños.

To the Older Grad Students — thanks for grilling and chilling all those years. Shoutout to Matt's grill.

To the Diffraction Spikes, the Moonshots, and the Spherical Cows — thanks for consistently overloading my life with physical activity.

To Blake — thanks for showing me what climbing is.
To Deryl — thanks for being my first ever friend (ostensibly).
To Jack — thanks for the Primo chalk and the Pantone 7737.
To Adrian — thanks for inspiring me to commit to the send.
To the Chads — never stop Chadding.

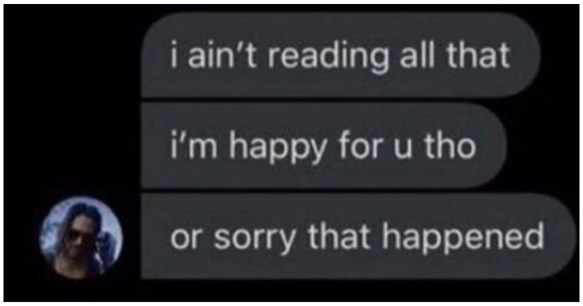

i ain't reading all that

i'm happy for u tho

or sorry that happened

Figure 1: Probably what you're thinking right now.

Table of Contents

List of Figures

List of Tables

Chapter 1

Introduction

From a typical dark sky site on Earth (for example — Fan Mountain Observatory, roughly 20 miles south of Charlottesville, VA!) it is possible to see about 5,000 stars with the naked eye, simply by looking up. For millennia this tapestry of light has proven of great use to humanity, for purposes extending from timekeeping to navigation. There is much more to the story of the stars, however, beyond the uses of the few thousand that met the eye of the ancients. In the early 1600s Galileo Galilei pointed his recently invented refracting telescope toward the sky, and in doing so unlocked a powerful tool for studying outer space, allowing astronomers and laypeople alike to peer deeper into the heavens. Today, we know that our Sun is just one of hundreds of billions of stars in the Milky Way galaxy. Further still, the Milky Way itself is just one galaxy in a web of trillions that make up the large scale structure of the Universe. Each of these galaxies contains billions of stars!

Though from our perspective the stars may seem eternal, etched in the sky as unyielding beacons of light, they are not forever. Like each and every one of us, they will eventually die. In fact, many generations of stars have already died, and it is thanks to this fact that we are even around! All elements heavier than hydrogen, helium, and lithium exist only because they were fused in the cores of earlier generations of stars. When a low-mass (less than about 8 times the mass of the Sun) star dies it sheds its outer layers in a planetary nebula, leaving behind an inert CO core remnant known as a white dwarf. Meanwhile, high-mass stars undergo more violent explosions called supernovae. This has the effect of depositing the material fused in their cores across vast regions of space. Eventually, this gas becomes part of the stellar nurseries that harbor the formation of the next generations of stars and planets, and the cycle begins anew.

The stellar birth environment has enormous dynamical and chemical complexity, so the task of understanding the star formation process in detail is a challenging one. In addition to recycled gas, regions of star formation are also threaded by magnetic fields that impart pressure and tensions forces on the gas. Star formation therefore involves a complex balance of turbulence, gravity, and magnetic forces. Furthermore, the physics of interest occur over a huge range scales, spanning from parsec-sized molecular clouds down to au-scale disk features.

Given its complexity, star formation is a topic that is well-suited for numerical modeling. In this thesis I use numerical simulations and radiative transfer modeling to study the role of magnetic fields in a variety of star formation environments. Ultimately, I produce three pieces of work that contribute to the literature. Before proceeding to detailed accounts of those works, however, we must first introduce the problem of star formation in some detail and discuss the current state of the field.

1.1 Star Formation, From Clouds to Disks

1.1.1 Molecular Clouds

The star formation process begins in molecular clouds, over-dense (relative to the diffuse medium) volumes of gas and dust typically of length $L \sim$ a few to tens of parsecs, mass $M \gtrsim 10^4\ M_\odot$, ambient magnetic field strength $B \gtrsim 10\ \mu$G, and temperature $T_{gas} = T_{dust} \approx 10$ K corresponding to sound speed $c_s \approx 0.2(T/10\ \mathrm{K})^{1/2}$ km/s with a helium-to-hydrogan number density ratio of $n_{He}/n_H = 0.1$ (Tan et al., 2013). They are roughly in radiative equilibrium, with heating primarily supplied by cosmic rays (especially deep in the cloud) and cooling primary by molecular line and dust radiation. Mechanical sources of heating (e.g., shocks) can have local temperature effects, but do not have a substantial effect on the global cloud temperature because the heating timescale is much longer than the timescale for radiative cooling.

Molecular clouds are named as such because their physical conditions foster the formation of molecules, the most abundant of which is universally H_2, followed by CO ($n(\mathrm{CO}) \sim 1.3\times10^{-4}\ n(\mathrm{H_2})$; Ripple et al., 2013). The densest parts of molecular clouds (where $n_H \gtrsim 10^4\ \mathrm{cm}^{-3}$) are alternatively referred to as dark nebulae due to their characteristically high visual extinction ($A_v \geq 1$; Bergin & Tafalla, 2007), wherein gas and dust block background starlight and prevent accessibility with optical telescopes. Molecular clouds are therefore primarily observed by way of far-infrared ($\sim 20 - 500$ μm) dust emission, sub-mm/mm continuum, and rotational line transitions in the radio.

Molecular clouds form from collisions of turbulent flows in the ambient medium. Often these collisions are dominated by overwhelmingly large kinetic energy and the flows dissipate, but in some cases the gas becomes bound to form self-gravitating molecular clouds. If a cloud has a non-axisymmetric gravitational potential or turbulent motion, it may then fracture into several pre-stellar cores on a $\sim$few megayear timescale, each with total mass $M \sim 1 - 100\ M_{\odot}$ and $L \sim 0.1$ pc (André et al., 2009). Runaway gravitational collapse of core gas then leads to the birth of stars. The driving mechanism by which this process ultimately proceeds is dependent on the cloud's balance of gravitational, magnetic, and turbulent energy. In the case that magnetic fields are sufficiently weak so that the mass of the molecular cloud is supercritical, $M > M_{\phi} = \phi/2\pi\sqrt{G}$, where ϕ is magnetic flux and M_{ϕ} is the critical mass, gravity is strong enough to overwhelm magnetic support and allow star formation on roughly the free-fall timescale $t_{ff} \sim 1/\sqrt{G\overline{\rho}}$ (Elmegreen, 2000). For a subcritical ($M < M_{\phi}$) cloud, magnetic pressure is large enough to resist the collapse of gas. As we will see in Section 1.2, the gas in molecular clouds is well modeled as a magnetohydrodynamic (MHD) fluid, and in the so-called “ideal" case the magnetic fields are “frozen-in" to the fluid. Strong-field models therefore must rely on “non-ideal" MHD effects, such as ambipolar diffusion, for the final stages of star formation to proceed.

The nature of a molecular cloud's turbulent motions can also play an important role in dictating the morphology of the forming cores. In the case of a relatively weak turbulent energy component compared to the gravitational and magnetic energies, random kinetic motions will dissipate roughly on the free-fall timescale of the cloud, t_{ff}, and only be important at early-times (Mac Low et al., 1998). Simulation work has shown that strong turbulence can persist longer, and act to reduce the time for stars to form in subcritical cores (Nakamura & Li, 2005) and enhance ambipolar diffusion, even becoming the primary driver on small scales (Zweibel, 1988).

1.1.2 Core Collapse

Since molecular clouds do not have perfect spherical symmetry and are subject to quasi-random gas motions (e.g. from turbulence), regions of local collapse naturally occur. A typical core has a density of $\sim 10^5$ cm^{-3} and is cold ($T \sim 10$ K, similar to the temperature of global cloud environment). Because thermal cooling (from dust grains) is efficient at low densities, the initial collapse is isothermal. Ambipolar diffusion may be required to overcome magnetic support. Eventually, as density increases, the core becomes optically thick and cooling is no longer efficient. As a result the temperature increases to the point that thermal support is roughly able to balance gravity. This produces a somewhat long-lived ($\sim 10^4$ yrs) equilibrium object known as the first hydrostatic core (FHSC). However, the equilibrium is not exact and material from outside the core continues to slowly funnel in. This allows the temperature to gradually increase. At this point the clump of gas is still mostly in the form of H_2. When $T \sim 2000$ K is reached, collisional dissociation of H_2 starts to occur. This removes much of the pressure support, leading to very rapid second collapse that only lasts a few years.

1.1.3 Disk Formation

As a sub-core of mass between $\lesssim 1\ M_\odot$ and $\sim 100\ M_\odot$ undergoes runaway center-seeking collapse, small angular momentum inhomogeneities in the initial core configuration are amplified and a preferred axis of rotation is established. This results in the formation of a protoplanetary disk around the central point source (i.e. the protostar). Numerical studies suggest that disks form rapidly (in $\sim 10^4$ yr) for weakly magnetized cores (Hueso & Guillot, 2005), with the final mass and size ($R(t) \propto \Omega^2 t^3$) strongly dependent on core infall time (Terebey et al., 1984). In more strongly magnetized cores, disk formation can be strongly affected, even suppressed, by magnetic braking (Li et al., 2014). Most mass-accretion onto the protostar occurs quickly, with the star reaching half of its final mass within $\sim 10^4$ yr (Evans et al., 2009).

In an observational context, star/disk systems are canonically referred to as young stellar objects (YSOs), further partitioned into classes (0,I,II,III) based on their IR spectral index (Lada, 1987). It turns out that these classes roughly correspond to an age sequence, with Class I objects having strong (and rising in wavelength space) IR excess due to a thick disk and significant envelope, Class II having a substantial (but declining) excess due to continued accretion from the disk, and Class III characterized by minimal accretion and very little IR excess. Class 0s are the youngest sources, with spectral energy distributions peaking in the far-IR to mm range. Since young (Class 0 and I) disks are deeply embedded, they are most fruitfully observed with long wavelength interferometers.

1.1.4 Magnetic Fields

At all stages in this evolutionary process, from cloud to disk scales, the star formation environment is threaded by pervasive magnetic fields. On the cloud scale $B_{0,cloud} \gtrsim 10$ μG, and this becomes amplified to $B_{0,disk} \gtrsim 10$ mG as the field is pinched and dragged by frozen-in matter that collapses to form a disk. Since the field and matter interact directly and magnetic fields can strongly influence gas dynamics, developing intuition for the physics of star formation on all scales relies heavily on parsing the magnetic field configuration (i.e. strength and spatial orientation) such that its physical contribution to the system may be disentangled. In the environments of interest here, magnetic fields are best accessed through polarization studies. This is discussed in more detail in Section 1.3 below.

1.2 Magnetohydrodynamics in Star Forming Clouds

Given their important role in regulating gas dynamics, magnetic fields must be understood if we wish to develop a clear intuitive understanding of clouds and disks and the intervening star formation process. Observational tools are a key piece of this puzzle, but they are naturally limited by projection effects and uncertain distance information. It is therefore useful to produce and study theoretical models of star formation environments. For many purposes it is sufficient to simply construct an analytic model, often making use of empirically derived constraints to justify one's choices. I do this for my work in Chapter 2 of this thesis, for example, to model how the morphology of circularly polarized emission can change based on simple changes to the geometry of magnetic fields in a protoplanetary disk. However, other times it is the case that we wish to understand the dynamics in a more complex manner or are studying an environment that is of sufficient physical complexity that analytic modeling is impractical. Star forming clouds, wherein the gas dynamics are affected by a delicate balance of turbulence, gravity, and magnetic fields, are one such environment. For this purpose we may turn to the study of magnetohydrodynamics (MHD).

1.2.1 Hydrodynamics

The dynamics of fluid flows are well described by the Navier-Stokes equations. These consist of an equation of mass conservation,

$$\frac{\partial \rho}{\partial t} + \nabla \cdot (\rho \boldsymbol{v}) = 0\,, \tag{1.1}$$

and momentum conservation,

$$\frac{\partial \rho \boldsymbol{v}}{\partial t} + \nabla \cdot (\rho \boldsymbol{v}\boldsymbol{v} + P) = -\rho \nabla \Phi_g \,. \tag{1.2}$$

In these equations ρ is the mass density of the fluid, $\boldsymbol{v}$ is the fluid velocity, and P is the pressure. The (self-)gravitational potential Φ_g may be computed from Poisson's equation,

$$\nabla^2 \Phi_g = 4\pi G \rho \,. \tag{1.3}$$

For these equations to function as a framework for evolving the dynamics of a fluid, an equation of state for the pressure $P = P(\rho, T)$ must be supplied. In general an equation for the temperature is also required, but since star forming clouds are approximately in radiative equilibrium ($T \approx 10$ K) it is standard practice to model them using an isothermal equation of state:

$$P = \rho c_s^2 \,. \tag{1.4}$$

1.2.2 MHD

MHD expands on this foundation to describe the dynamics of a conducting fluid threaded by a magnetic field $\boldsymbol{B}$. The qualifier used here — conducting — encapsulates an essential property of the fluid: it must be able to carry electrical current. This qualification excludes some media, a familiar example being pure water under typical conditions. Pure water is an excellent insulator, because it is made up of neutral molecules without any charge (H_2O). Gas in molecular clouds, on the other hand, is lightly ionized and therefore suitably modeled by MHD.

As observed by Ohm, there is a local relationship between electrical current $\boldsymbol{j}$ and electric field $\boldsymbol{E}$, which for a medium at rest may be written as

$$\boldsymbol{j} = \sigma \boldsymbol{E} \, , \tag{1.5}$$

where σ is the electrical conductivity. Here we can see why the medium must be conducting; for a perfect insulator $\sigma = 0$, and it follows that $\boldsymbol{j} = 0$ as well in that case.

Electrical current is the flow rate of electrical charge relative to a given point and has dimensionality

$$[\boldsymbol{j}] = [\frac{\text{charge}}{\text{volume}} \times \boldsymbol{velocity}] \, . \tag{1.6}$$

Therefore, to have non-zero $\boldsymbol{j}$ we must have charge carrying species' in the fluid, and they must be moving relative to each other. A basic example to consider when thinking of this situation is a simple electrical circuit consisting of a battery and resistor connected by a thin wire that contains protons and electrons. As we know from classical E&M, in this circuit current 'flows' from the positive terminal of the battery to the negative terminal of the battery. However, since $m_p \gg m_e$ we can to very good approximation think of the protons as stationary, with the electrons flowing at velocity $\boldsymbol{u}_e$ in the opposite direction of the current 'flow.' For an electron number density n_e, the current is therefore $\boldsymbol{j} = -n_e q \boldsymbol{u}_e$, where q is the charge of a proton (so $-q$ is the charge of an electron). In the case of a general fluid we should also consider the motion of the positively charged ions, with number density n_i traveling at velocity $\boldsymbol{u}_i$. Assuming global neutrality of the medium and that most of the ions are single-ionized species, which is reasonable in our astrophysical context, we can set

$n_i = n_e$ and finally write

$$\boldsymbol{j} = n_e q(\boldsymbol{u}_i - \boldsymbol{u}_e)\,. \tag{1.7}$$

Returning to Ohm's law, we now can clearly see that for a fluid to be conducting ($\sigma > 0$) we must also have $n_e > 0$. That is, for electrical conduction to occur, and therefore for MHD to apply, the medium must be ionized. The degree of ionization required is generally not large in astrophysical environments.

We can now summarize the basic assumptions that comprise the MHD approximation, and see that this applies well to our astrophysical context (e.g., star forming clouds):

1. The environment of interest can be well described as a fluid. This means that there must be many many particles present, allowing us to define continuous properties like fluid pressure, density, and velocity at the length scales of interest. Local thermodynamic properties must be definable and slow-varying.

2. We must be able to write Ohm's Law for our fluid (on the scales of interest). Equivalently, our medium must be ionized.

3. The fluid must be globally electrically neutral.

1.2.3 The MHD Equation

In this section we derive an equation for the time evolution of the magnetic field in a hydrodynamic fluid. As MHD is a theory for magnetized flows of matter, the equations central to hydrodynamics (Section 1.2.1) must be supplemented by Maxwell's equations:

$$\nabla \cdot \boldsymbol{D} = 4\pi\rho \qquad \textbf{Coulomb's Law}\,, \tag{1.8}$$

$$\nabla \cdot \boldsymbol{B} = 0 \qquad \textbf{No Magnetic Monopoles}\,, \tag{1.9}$$

$$\nabla \times \boldsymbol{E} = -\frac{1}{c}\frac{\partial \boldsymbol{B}}{\partial t} \qquad \textbf{Faraday's Law}\,, \tag{1.10}$$

$$\nabla \times \boldsymbol{H} = \frac{4\pi}{c}\boldsymbol{j} + \frac{1}{c}\frac{\partial \boldsymbol{D}}{\partial t} \qquad \textbf{Ampere's Law}\,, \tag{1.11}$$

where $\boldsymbol{D} = \epsilon\boldsymbol{E}$ and $\boldsymbol{H} = \boldsymbol{B}/\mu$. In astrophysical situations it is usually the case that we can ignore the dialectric properties and magnetic permeability of our fluid and write $\epsilon = \mu = 1$.

From these equations we can also easily recover charge conservation by taking the time derivative of Coulomb's Law (1.8) and taking the dot product of Ampere's Law (1.11), then combining to obtain

$$\frac{\partial \rho}{\partial t} = -\nabla \cdot \boldsymbol{j} \qquad \textbf{Charge Conservation}\,. \tag{1.12}$$

There are a few approximations we can further still make to reduce Maxwell's equations to a more manageable set for our treatment of fluid flows in star forming clouds.

First, $\frac{1}{c}\frac{\partial \boldsymbol{E}}{\partial t}$ is small compared to the other terms in Ampere's Law. This is commonly referred to as the approximation of slow time varying fields or the "low wavelength" approximation, and it allows us to drop the displacement current from equation 1.11. Namely, in the observer frame $E \sim \frac{u}{c}B$, so we can safely apply this to non-relativistic environments. Note that under this approximation we implicitly state that electrical currents are the only source of magnetic fields.

Second, the drift velocity $\boldsymbol{v}_{\mathrm{d}} = \boldsymbol{u}_i - \boldsymbol{u}_e$ between ions and electrons is very small, and can be ignored after being used to calculate $\boldsymbol{j}$. Equation 1.7 tells us that $\boldsymbol{j} \propto \boldsymbol{v}_{\mathrm{d}}$, so we must have some drift between the positive and negatively charged species in our fluid for the MHD approximation to be valid. However, production of magnetic fields with strengths typical for molecular clouds ($B \sim 10\ \mu$G) only requires tiny drift velocities. We can estimate v_d using Ampere's Law (1.11), which in a dimensional sense may be written as

$$v_d \sim \frac{cB}{4\pi n_e q L}\,, \tag{1.13}$$

where we've used equation 1.7 to plug in $j = n_e q v_d$. Taking a typical length scale of $L \approx 0.1$ pc and $n_e \approx 10^3$ cm^{-3} for cloud scale dynamics, we obtain $v_d \approx 10^{-7}$ cm s^{-1} $\approx 10^{-12}$ pc Myr^{-1}. This is very small, and tells us that for our clouds on this scale is acceptable to ignore the mean motions between electrons and ions and use a single gas velocity $\boldsymbol{u}$ for dynamics calculations. However, in smaller-scale environments (e.g., cores) this particular assumption must be relaxed so that neutrals can slip through the ionized fluid, allowing for the formation of a large Keplerian disk without a catastrophic build-up of magnetic flux near the center (see Section 1.2.5 for details).

Third, we can rewrite the current $\boldsymbol{j}$ in terms of other variables. In the frame of reference of the fluid (moving at non-relativistic velocity $\boldsymbol{u}$) we can write Ohm's Law as

$$\boldsymbol{j}' = \sigma \boldsymbol{E}'\,, \tag{1.14}$$

where primes denote the changes to the frame co-moving with the fluid. Furthermore,

$$\boldsymbol{j}' = \boldsymbol{j} \tag{1.15}$$

since the relative velocity between neutrals and ions is not affected by the change of frame, and

$$\boldsymbol{E}' = \boldsymbol{E} + \big(\frac{\boldsymbol{u}}{c} \times \boldsymbol{B}\big)\,. \tag{1.16}$$

Combining Equations 1.14, 1.15, and 1.16 allows us to write an expression for $\boldsymbol{j}$ in the original frame:

$$\boldsymbol{j} = \sigma\big(\frac{\boldsymbol{u}}{c} \times \boldsymbol{B}\big)\,. \tag{1.17}$$

Substituting this expression into Ampere's Law (Eq. 1.11), then invoking Faraday's Law to replace $\boldsymbol{E}$, we finally arrive at an expression for the temporal evolution of the magnetic field:

$$\frac{\partial \boldsymbol{B}}{\partial t} = \nabla \times (\boldsymbol{u} \times \boldsymbol{B}) - \nabla \times \big(\frac{c^2}{4\pi\sigma} \nabla \times \boldsymbol{B}\big)\,. \tag{1.18}$$

1.2.4 Ideal MHD

Notably, the final term of Equation 1.18, sometimes called the "Ohmic dissipation" term, contains the conductivity of the fluid. In molecular clouds it turns out that a fully conductive assumption is appropriate, as the neutral particles are well-coupled to the ions and magnetic diffusion is relatively slow compared to dynamical timescales of interest. This allows us to eliminate this term containing σ in the denominator, leaving us with the so-called "ideal-MHD" equation:

$$\frac{\partial \boldsymbol{B}}{\partial t} = \nabla \times (\boldsymbol{u} \times \boldsymbol{B}) \,. \tag{1.19}$$

Incidentally this form of the equation implies a phenomenon called "flux-freezing," and the fluid is coupled entirely to the magnetic field lines. Particularly, it can be shown that for magnetic flux Φ threading through a closed loop A,

$$\Phi = \int_A \boldsymbol{B} \cdot \hat{\boldsymbol{n}} dA \,, \tag{1.20}$$

the ideal-MHD equation yields $d\Phi/dt = 0$. From this result we see that for a medium where the "infinity conductivity" assumption applies well (e.g., a star forming cloud!), the fluid dynamics are tied directly to the magnetic field. This makes it clear that to understand the process of star forming from collapsing gas, we (essentially, by definition) must also understand the magnetic field.

Now we have a simple expression (and intuitive picture) for the time evolution of the magnetic field in a star forming cloud. To write down the full set of equations required to model the dynamics of our MHD fluid, we must also remember that electromagnetic fields impart forces on the charged particles in the medium by way of the Lorentz Force:

$$\boldsymbol{F}_L = q\big(\boldsymbol{E} + \frac{\boldsymbol{u}}{c} \times \boldsymbol{B}\big) \,. \tag{1.21}$$

Since the Lorentz force acts on both ions and electrons, we can also write a Lorentz force per unit volume that explicitly accounts for both:

$$\boldsymbol{f}_L = qn_i\big(\boldsymbol{E} + \frac{\boldsymbol{u}_i}{c} \times \boldsymbol{B}\big) - qn_e\big(\boldsymbol{E} + \frac{\boldsymbol{u}_e}{c} \times \boldsymbol{B}\big)\,. \tag{1.22}$$

Recalling now our definition for $\boldsymbol{j}$ in Equation 1.7, this is equivalent to

$$\boldsymbol{f}_L = \frac{1}{c}\boldsymbol{j} \times \boldsymbol{B}\,, \tag{1.23}$$

or, using Ampere's Law,

$$\boldsymbol{f}_L = \frac{1}{4\pi}(\nabla \times \boldsymbol{B}) \times \boldsymbol{B}\,. \tag{1.24}$$

Using simple trigonometric identities, this can further be rewritten as

$$\boldsymbol{f}_L = \frac{1}{4\pi}(\boldsymbol{B} \cdot \nabla)\boldsymbol{B} - \frac{1}{8\pi}\nabla B^2\,. \tag{1.25}$$

Here we have decomposed the Lorentz force into terms that can qualitatively be thought of as a magnetic tension term (first term) and a magnetic pressure term (second term).

Incorporating the magnetic tension and pressure forces into the hydrodynamics equations, we are now ready to write the full set of equation for the evolution of the fluid and magnetic fields in ideal-MHD:

$$\frac{\partial \rho}{\partial t} + \nabla \cdot (\rho \boldsymbol{v}) = 0 \qquad \textbf{Continuity}\,, \tag{1.26}$$

$$\frac{\partial \rho \boldsymbol{v}}{\partial t} + \nabla \cdot \big(\rho \boldsymbol{v}\boldsymbol{v} + P + \frac{B^2}{8\pi} - \frac{\boldsymbol{B}\boldsymbol{B}}{4\pi}\big) = -\rho \nabla \Phi_g \qquad \textbf{Conservation of Momentum}\,, \tag{1.27}$$

$$\frac{\partial E}{\partial t} + \nabla \cdot [\big(E + P + \frac{B^2}{8\pi}\big)\boldsymbol{v} - \frac{\boldsymbol{B}(\boldsymbol{B} \cdot \boldsymbol{v})}{4\pi}] = -\rho \boldsymbol{v} \cdot \nabla \Phi_g \qquad \textbf{Conservation of Energy}\,, \tag{1.28}$$

$$\frac{\partial \boldsymbol{B}}{\partial t} - \nabla \times (\boldsymbol{v} \times \boldsymbol{B}) = 0 \qquad \textbf{Ideal-MHD Equation}\,. \tag{1.29}$$

Conceptually, tension and pressure are the ways that magnetic fields can enact forces on the fluid. Essentially the “desired state” for the magnetic field is to be fully uniform and with straight field lines, and the Lorentz force will impart forces on the gas as the magnetic fields attempt to redistribute in this way. Of course, in addition to magnetic energy the dynamics of the star forming environment are also affected by turbulent energy and gravitational energy. In practice the magnetic fields never actually reach the desired uniform configuration, but rather continuously act to resist the collapse of gas under the influence of gravity. A schematic illustration of these magnetic force components is presented in Figure 1.1.

We have now, to suitable detail for the purposes of this thesis, introduced the theoretical framework for ideal MHD. Indeed, for our work in Chapter 3 we use a code that evolves the dynamics of a molecular cloud using Equations 1.26-1.29 to study magnetohydrodynamic flows during the early stages of dense structure formation in the star formation process. A short introduction to the MHD codes used for the work in this thesis is given in Section 1.5.1.

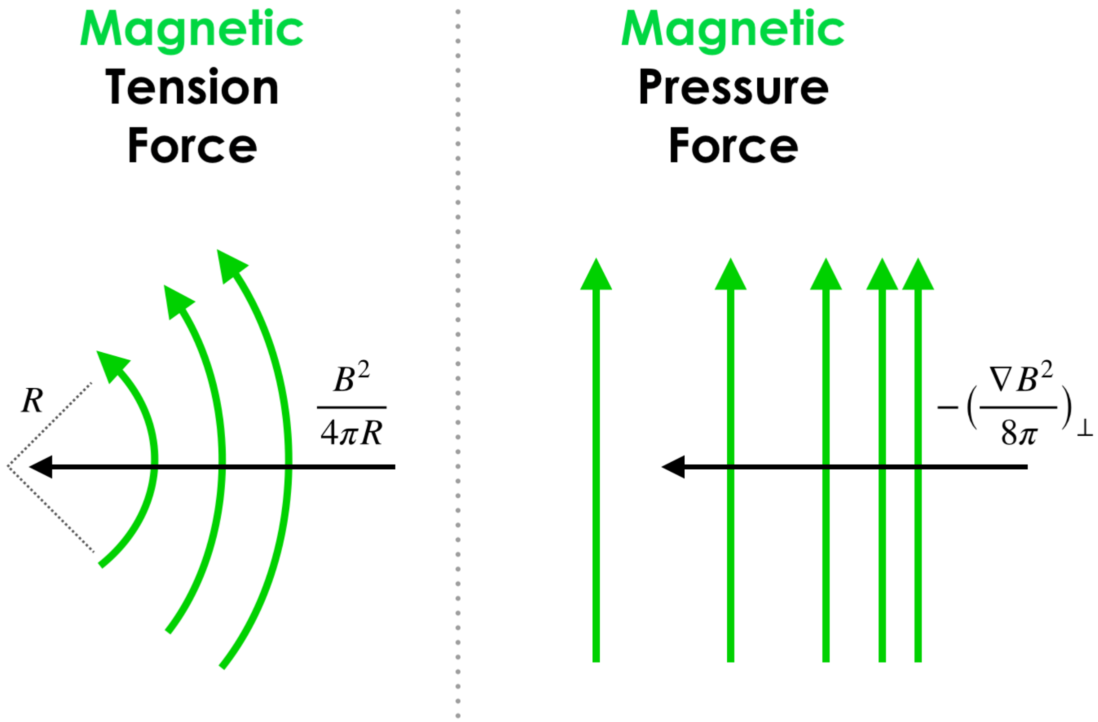

Figure 1.1: A schematic visualization of the magnetic tension and magnetic pressure forces.

1.2.5 Non-ideal MHD

At smaller (i.e., core and sub-core) scales, the ideal-MHD assumption faces a catastrophic breakdown. Ideal-MHD simulations of collapsing cores result in a large buildup of magnetic flux at the center. Though a so-called "pseudo-disk" is able to form initially, as gas flows preferentially along the field lines (instead of orthogonal to field lines, due to magnetic forces), this process leads to significant magnetic field line pinching at the midplane as the magnetic field is pulled along with frozen-in gas under the influence of gravity. Ultimately, this flux buildup produces a strong magnetic tension force that pushes angular momentum outward and prevents a bona fide disk from forming. This result is in conflict with empirical data, since disks around YSOs are nearly ubiquitous.

To get past this problem, we must introduce additional physics into our core- and disk-scale simulations. We can do this by entering the domain of non-ideal MHD. Generally, non-ideal effects include Ohmic dissipation, the Hall effect, and ambipolar diffusion. Though Ohmic dissipation and the Hall effect can in principle be important at very high density, for our purposes it is only important to introduce ambipolar diffusion.

To do this, we must remember that our magnetohydrodynamic fluid contains neutrals, ions, and electrons (ignoring dust grains for simplicity), and only the charged particles are tied to the magnetic field. The neutrals are, therefore, only affected by the magnetic field through a drag force imparted from direct interaction with the ions (Shu, 1991). This allows the neutrals to slip through magnetic field lines, facilitating gas collapse without too much magnetic flux buildup. Though the magnetic field may still be pinched to some extent, the effect of this ambipolar diffusion is that it allows the rate of change of gravitational energy density in the cloud core to exceed that of the magnetic energy density (Crutcher, 2012), prescribing magnetic flux loss on timescale $t_{AD} \sim L/v_D > t_{ff}$, where v_D is the drift speed of neutrals against ions.

By developing of formalism for ambipolar diffusion, we can write a new equation for the time evolution of the magnetic field. First, since the only the ions are frozen-in to the magnetic field we may rewrite Equation 1.29 as

$$\frac{\partial \boldsymbol{B}}{\partial t} + \nabla \times (\boldsymbol{B} \times \boldsymbol{u}_i) = 0\,, \tag{1.30}$$

where $\boldsymbol{u}_i$ is velocity of the ion plasma. To connect this back to the neutral velocity $\boldsymbol{v}$, we then write down the per unit volume drag force they face from the ions:

$$\boldsymbol{f}_{\text{drag}} = \gamma \rho \rho_i (\boldsymbol{u}_i - \boldsymbol{u})\,, \tag{1.31}$$

where γ is a drag coefficient with value $\gamma \approx 3.5 \times 10^{13}$ cm^3 g^{-1} s^{-1} in a star forming cloud (Draine et al., 1983).

In these clouds, the fractional ionization is fairly low ($n_i/n \sim 10^{-7}$). This implies that the forces on the charged particles in the medium are dominated by the Lorentz force and the drag force. These forces must therefore sum to zero ($\boldsymbol{f}_L = -\boldsymbol{f}_{\text{drag}}$). Using the form of the Lorentz force in Equation 1.24, this gives us the following expression for the ion-neutral drift velocity:

$$\boldsymbol{u}_i - \boldsymbol{u} = \frac{1}{4\pi\gamma\rho\rho_i} (\nabla \times \boldsymbol{B}) \times \boldsymbol{B}\,. \tag{1.32}$$

We can now use this equation to eliminate u_i from Equation 1.33, leaving us with an equation for the evolution of the magnetic field in terms of the neutrals:

$$\frac{\partial \boldsymbol{B}}{\partial t} + \nabla \times (\boldsymbol{B} \times \boldsymbol{u}) = \nabla \times \{\frac{\boldsymbol{B}}{4\pi\gamma\rho\rho_i} \times [\boldsymbol{B} \times (\nabla \times \boldsymbol{B})]\} . \tag{1.33}$$

This is the form of the inductance equation used to evolve the dynamics of the envelope systems studied in Chapter 4 of this thesis.

1.3 OBSERVATIONAL PROBES OF MAGNETIC FIELDS

Since magnetic fields are important drivers of dynamics in star forming environments, they are naturally of great observational interest. However, observational signatures of magnetic fields are difficult to obtain. Over the past several decades much work has gone into developing methods for accessing magnetic information in star forming clouds, cores, and protoplanetary disks. To that end, there are two main techniques commonly leveraged to obtain magnetic field information in these environments. Both of these techniques, the Zeeman effect and linear dust polarization observations, rely on having instruments that are capable of processing polarized light.

Below I provide an overview of these two techniques, including an introduction to the fundamental physics underscoring each and the observational information they afford us. It is also the case that observers can combine these polarization data with kinematic information to develop other powerful tools for studying the magnetic field. This includes the Chandrasekhar-Fermi (C-F) method (Chandrasekhar & Fermi, 1953) and the velocity gradient technique (González-Casanova & Lazarian, 2017). I give some physical background on the C-F method in Section 1.3.3 below.

1.3.1 The Zeeman Effect (Circular Polarization)

The Zeeman Effect is the only method available for directly detecting astrophysical magnetic fields and measuring their strengths. The technique relies on the fact that the energy levels of some atomic and molecular species (including H I, OH, and CN) are split into multiple sub-levels in the presence of a magnetic field. These affected molecules are hydrogenic with an odd (unpaired) election, allowing for splittings that are large enough to be detectable. The degree of splitting is proportional to the local magnetic field strength, with Zeeman-split lines producing emission at frequencies

$$\nu = \nu_0 \pm \frac{\mu_B B}{h} \tag{1.34}$$

below and above the original rest frequency ν_0. Here μ_B is a constant known as the Bohr magneton, with value $\mu_B = 9.2732 \times 10^{-21}$ erg/G.

The Zeeman Effect results in circularly polarized emission. As electrons orbit around magnetic field lines, their accelerations produce electromagnetic radiation orthogonal to the electron orbit. This means that the circularly polarized radiation is only visible to the observer for magnetic field components along the observer's line-of-sight. Each individual electron produces only one component, but in practice we observe the emission from many electrons at a time. Therefore, the Zeeman Effect results in equal emission at both the lower and higher frequency.

We perform modeling of CN $J = 1-0$ Zeeman emission in Chapter 2 and Chapter 4 of this thesis. An additional primer with more details on the basics of the Zeeman Effect is given in Section 2.2.

1.3.2 Linear Dust Polarization

Another method for accessing magnetic field information in star forming clouds relies on the fact that, in addition to gas, some fraction of the material is also in the form of dust. In fact, it is predicted that in the interstellar medium about ∼1% of the mass is dust. Interstellar dust comes mainly in the form of carbonaceous grains and silicates. The silicates are paramagnetic, and therefore may be coupled to the ambient magnetic field. As we will see below, through a series of alignment mechanisms these grains are expected to become oriented with their long axes perpendicular to the magnetic field. This is collectively known as the theory of radiative alignment torques (RAT) (Lazarian & Hoang, 2007).

The process of grain alignment, according to the RAT theory, occurs in two stages; "internal" alignment, followed by "external" alignment. Interstellar dust grains are non perfectly spherical. Rather, they have many irregularities in their shapes, which leads them naturally to have some degree of helicity. This means that radiation that impinges on a grain will eventually cause it to spin about some axis due to the torque (this is the so-called radiative torque). Once a grain is spinning, the alignment process may begin. For internal alignment, some source of friction must exist to internally dissipate energy. In the case of paramagnetic grains the most efficient mechanism is the Barnett effect, a magnetic relaxation mechanism that results in the grain's angular momentum vector aligning with its axis of greatest inertia (Purcell, 1979).

After internal alignment is achieved, external alignment proceeds. This requires the grains to obtain some net internal magnetization, which for a silicate grain occurs through quantum mechanical spin-flips (Barnett, 1915). At this point the grain has a magnetic dipole moment $\boldsymbol{\mu}$, so it can interact with the ambient magnetic field. Particularly, the magnetic field exerts a torque on the grain ($\boldsymbol{\tau} = \boldsymbol{\mu} \times \boldsymbol{B}$) that leads

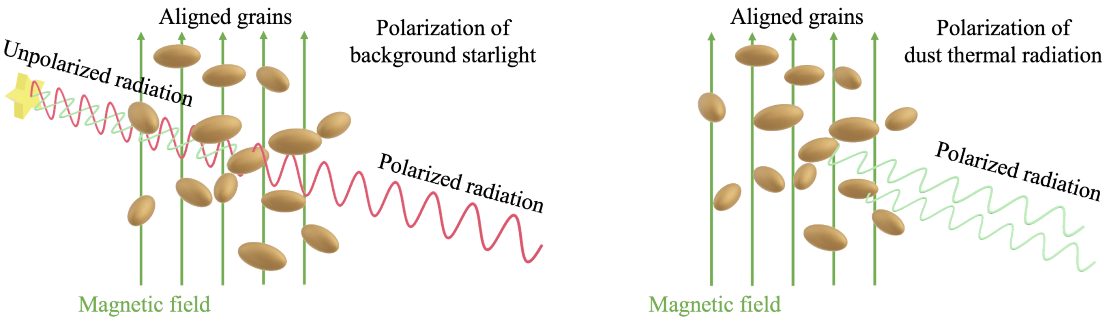

Figure 1.2: A schematic illustration of dust grain alignment with the local magnetic field and the resulting polarized emission. In addition to the far-infrared emission being polarized (right), emission from background starlight also becomes polarized due to extinction (left). This effect can be useful in low optical depth regions, like the edges of clouds ($A_v \lesssim 2-3$). This figure is adapted from Lazarian (2007).

the grain to align with its angular moment axis parallel to the magnetic field through a series of Larmor precessions.

From an observational point of view, the result of this alignment is that the thermal far-infrared emission from dust grains is polarized with E-field vectors orthogonal to the local plane-of-the-sky magnetic field direction. A schematic illustration of this is given in Figure 1.2. Polarimetric observations can therefore be used to infer the mean (density-weighted) plane-of-the-sky magnetic field direction, simply by computing the far-IR/(sub)mm E-field vectors and rotating them 90 degrees. As I discuss in Section 1.4 of this introduction, this technique has been used by many facilities to probe magnetic fields in star forming environments. In Chapter 3 of this thesis, we use a standard optically-thin prescription to model dust polarization in a molecular cloud. More details on our setup for this are discussed in Section 3.3.

1.3.3 The Chandrasekhar-Fermi (C-F) Method

The Chandrasekhar-Fermi method aims to take advantage of both kinematic and polarization information to infer the strength the magnetic field in a turbulent fluid.

The Alfvén Mach number quantifies the strength B of the magnetic field relative to the velocity v_σ of turbulent motions of the fluid. It is square root of the ratio between turbulent and magnetic energy densities and may be written as

$$M_A = \frac{\sqrt{4\pi\rho}v_\sigma}{B}\,. \tag{1.35}$$

To apply the C-F method, we assume that M_A is constant and we are in a piece of fluid that has constant density ρ_0. In ideal-MHD, a magnetic field perturbation δB requires a corresponding velocity perturbation. In the case of Alfvénic turbulence (i.e., when the overall turbulent velocity perturbations occurring in the medium are dominated by Alfvén waves), then we can write

$$1 \propto \frac{\delta v}{\delta B}\,, \tag{1.36}$$

where δv is the overall velocity fluctuation.

Linear polarization observations give us access to plane-of-the-sky magnetic information. We can usefully frame the plane-of-the-sky field strength in terms of a mean strength across the observational domain, $B_{\mathrm{avg,POS}}$, plus perturbations away from that value. Multiplying through by $B_{\mathrm{avg,POS}}$, we can write

$$B_{\mathrm{avg,POS}} \propto \frac{\delta v}{\delta B / B_{\mathrm{avg,POS}}}\,. \tag{1.37}$$

To proceed, we now make an assumption that is central to the C-F method: the velocity and magnetic field fluctuations are isotropic. Under this assumption, we can then write

$$\frac{\delta v}{\delta B} = \frac{\delta v_{\text{arbitrary direction 1}}}{\delta B_{\text{arbitary direction 2}}}\,. \tag{1.38}$$

We can then make the following contrived choices to allow us to leverage observational data in this equation. First, we choose the direction along the line-of-sight as the velocity perturbation direction (from the line-of-sight Doppler effect). Next, we choose the direction in the plane-of-the-sky orthogonal to direction of the mean field (as projected on the plane-of-the-sky) as the magnetic perturbation direction. This lets us re-write equation 1.37 as

$$B_{\text{avg,POS}} \propto \frac{\delta v_{\text{LOS}}}{\delta B_{\perp,\text{avg,POS}}/B_{\text{avg,POS}}}\,. \tag{1.39}$$

Defining ϕ to be the angle between a given magnetic field plane-of-the-sky vector and the mean plane-of-the-sky vector, we obtain our final relationship

$$B_{\text{avg,POS}} = \xi\sqrt{4\pi\rho_0}\frac{\delta v_{\text{LOS}}}{\delta\tan\phi}\,, \tag{1.40}$$

where $\xi \sim 0.5$ is an empirical correction factor (derived from simulations). In the case that there are multiple cells (eddies) of turbulence along the line-of-sight, the value of $\delta B_{\perp,\text{avg,POS}}$ inferred from observations is somewhat suppressed. This can be corrected for by multiplying by a factor of $\sim \sqrt{L_{\text{cell}}/L_{\text{LOS}}}$ (Cho & Yoo, 2016).

1.4 THE OBSERVATIONAL LANDSCAPE

In this section I introduce some of the important facilities that have been used to study magnetic fields in star forming environments using polarization. I begin at the largest (galactic) scale linear polarization, then proceed to discuss core- and disk-scale

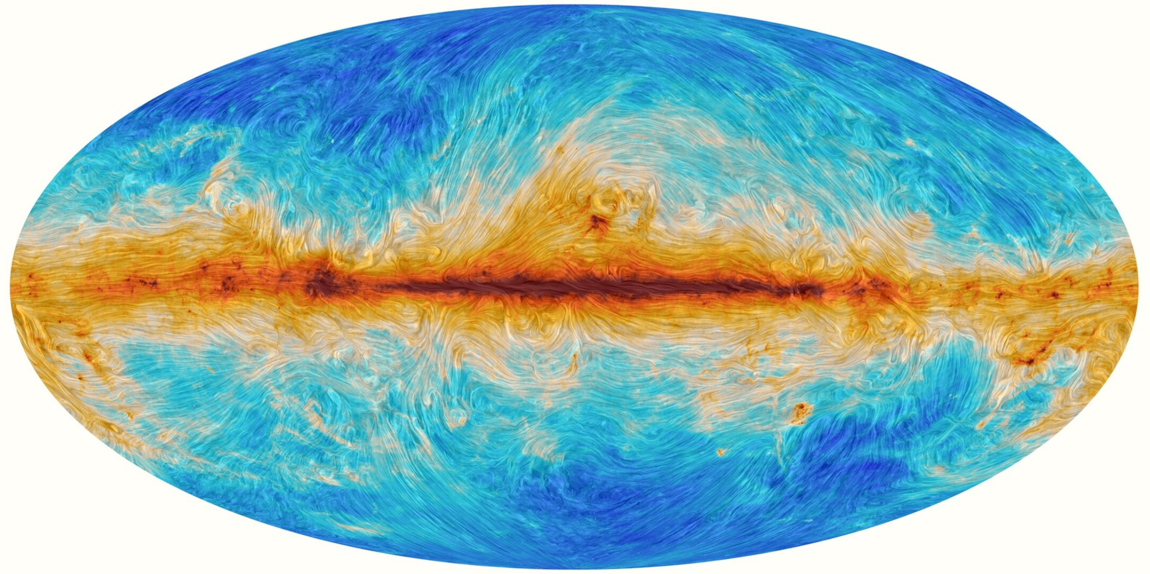

Figure 1.3: The *Planck* dust polarization map of the Milky Way. Credit: ESA/*Planck*

work as well. I also briefly discuss the history of Zeeman observations and their use to constrain magnetic field strengths in cores.

1.4.1 Planck

Planck was a European Space Agency (ESA) space-based mission that observed polarized emission across the whole sky in far-infrared and millimeter wavelengths. The main science goal was to map radiation from the Cosmic Microwave Background (CMB) to better understand the early Universe, but *Planck* also picked up foreground sources of polarization. This included polarization from dust in the Milky Way, allowing the mission to compute the plane-of-the-sky orientation of galactic-scale magnetic fields (Planck Collaboration et al., 2015a, 2016). A map of these results is given in Figure 1.3.

1.4.2 BLAST

The Balloon-borne Large-aperture Submillimeter Telescope (BLAST) collaboration is an experiment that has undertaken several high-altitude ballooning flights to

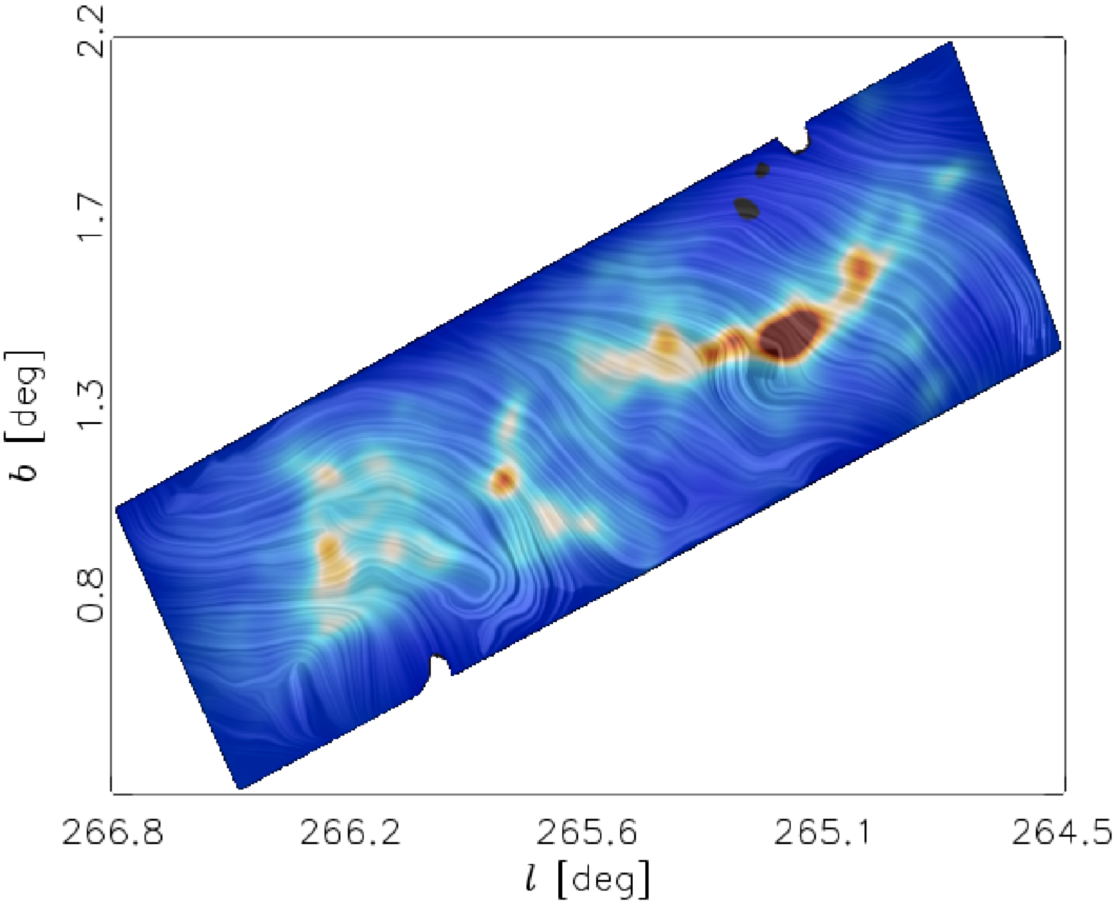

Figure 1.4: The *BLASTPol* dust polarization map of Vela C, from Fissel et al. (2016).

map molecular clouds at submillimeter wavelengths. In 2012, a polarimeter version of BLAST called *BLASTPol* was launched from Antaractica, and over a two-week mission mapped the Vela C cloud complex in high resolution, producing thousands of magnetic field pseudo-vectors at 250 μm, 350 μm, and 500 μm (Galitzki et al., 2014). Figure 1.4 shows a map of Vela C as observed with *BLASTPol*. To analyze molecular gas structure the BLAST team also observed millimeter line transitions for several molecules in Vela C with Mopra, a 22-m single dish telescope in Australia (Fissel et al., 2019). Together, these *BLASTPol* and Mopra results are used as a direct point of comparison for the work performed in Chapter 3 of this thesis.

1.4.3 SOFIA

The Stratospheric Observatory For Infrared Astronomy (SOFIA) was a 2.5-meter telescope periodically flown aboard a Boeing 747 from Palmdale Airport in California, US and Christchurch International Airport in New Zealand. The telescope, a 2.5-meter Cassegrain reflector, included instruments for observing in the infrared and far-infrared, suitable for studying star forming environments. One of these instruments was the High-resolution Airborne Wide-band Camera (HAWC+) that could perform polarized flux imaging in five bands between 50 μm and 240 μm with a spatial resolution of $\sim$5-20 arcseconds.

Among the polarization work done with SOFIA includes, for example, observations of the OMC-1 star forming region in the Orion Nebula. The HAWC+ polarimeter was used to map magnetic field structure at four far-infrared frequencies between 53 μm and 214 μm. Figure 1.5, taken from Chuss et al. (2019), shows the large-scale polarization as well as the pinching of the magnetic field seen in the inner regions. This “hourglass" morphology is especially clear at longer wavelengths. Meanwhile, the shorter wavelength data may be partially tracing molecular outflows. On a separate note, SOFIA has also been used to observe polarization in galaxies. Work by Lopez-Rodriguez et al. (2020) showed magnetic field vectors in NGC 1068 that closely followed the spiral arms of the galaxy, as inferred from 89 μm dust polarization.

1.4.4 JCMT

The James Clerk Maxwell Telescope (JCMT) is a submillimeter telescope located in Hawaii, US at Mauna Kea Observatory. One of the instruments on JCMT is SCUBA-2, a camera that operates in the far-IR/mm wavelengths. Operating in conjunction with SCUBA-2 is the POL-2 linear polarimeter, allowing JCMT to be used

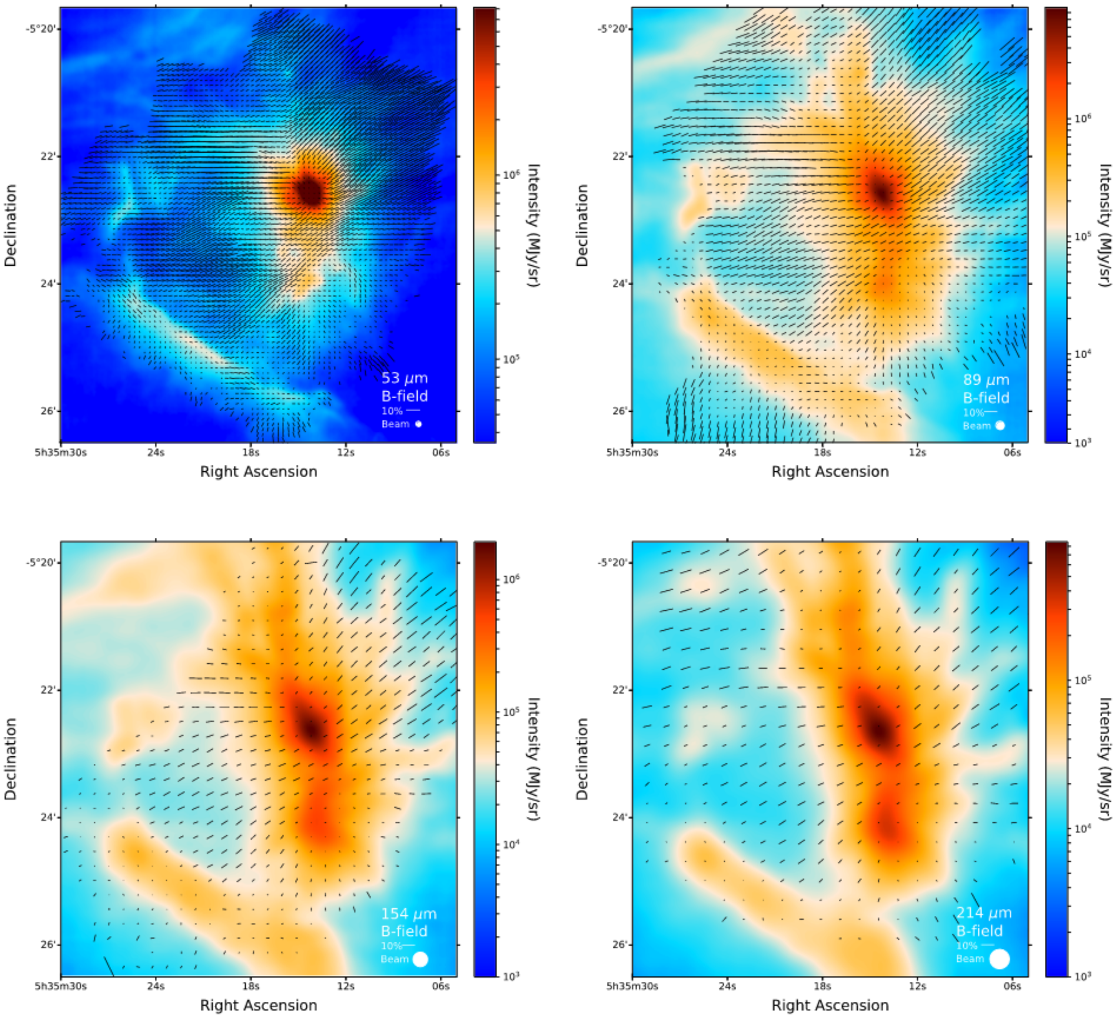

Figure 1.5: Multiband SOFIA/HAWC+ observations of OMC-1, from Chuss et al. (2019).

for dust polarization observations to access magnetic field information in cold dense cores and filaments on $\sim$1000 au scales in nearby regions of star formation. Among the notable work performed with SCUBA-2/POL-2 includes the BISTRO survey, which targeted several clouds in the Gould Belt (Ward-Thompson et al., 2017). Analysis of BISTRO data through comparison of inferred magnetic field orientation with molecular outflows found that, on average for the sources considered, the magnetic field direction tended to be offset from the outflows by about $15 - 35^\circ$ (Yen et al., 2021). Overall, these results are consistent with a picture with comparable magnetic and turbulent energy components in the cores. They also suggest this misalignment can only be a partial, not complete, solution to overcome the problem of magnetic braking.

1.4.5 ALMA

The Atacama Large Millimeter/submillimeter Array (ALMA) is a 66-dish interferometer in the Atacama Desert in Chile operated by an international partnership of many members around the world. ALMA, which came online for science observations in 2011, is capable of sub-arcsecond resolution and very high spectral resolution in velocity space, allowing us detailed access to the dust/gas structure and kinematics in disks. It has also since its inception functioned as a linear polarimeter, and much work has been done in attempt to diagnose the magnetic field morphology in these small-scale environments. This goal has, however, proven challenging due to the many other sources of linear polarization that are evidently important in disks.

Prior to any observations with ALMA, the first definitive hints of resolved linear polarization in disks came from the Combined Array for Research in Millimeter-wave Astronomy (CARMA). In 2014, Stephens et al. (2014) used CARMA to collect 1.25 mm polarized continuum data of HL Tau and found that the vectors implied the magnetic field to be oriented along the long-axis of the disk. This was a somewhat puzzling result, as it was expected that the magnetic field would be dominated by toroidal and vertical components. Meanwhile, CARMA observations by Segura-Cox et al. (2015) of the edge-on disk L1527 did not produce any hints of a vertical magnetic field component. Though they were able to plausibly explain this as evidence of a toroidally-dominated magnetic field, around this time there was a growing thought in the community that alternative sources of polarization were strongly affecting these results.

Work by both Kataoka et al. (2015) and Yang et al. (2016) suggested that self-scattering could be a dominant driver of linear polarization in disks. This idea was not only consistent with the observational data, including new higher-resolution ALMA observations of HD 142527 (Kataoka et al., 2016), but it also provided a powerful new tool for studying dust, since the scattering depends on maximum dust grain size. Multiband observations of HL Tau with ALMA (Stephens et al., 2017) further corroborated this picture. Their shortest wavelength data (ALMA Band 7, 870 μm) showed a polarization pattern with electric field vectors oriented along the minor axis of the disk, which was consistent with the earlier modeling for self-scattering (Yang et al., 2016). The highest wavelength data (ALMA Band 3, 3.1 mm), on the other hand, had a toroidal polarization pattern, which was perhaps indicative of some form of mechanical alignment (Yang et al., 2019). In any case, this change in the polarization morphology as a function of frequency would not be expected if grain alignment with the magnetic field were the dominant mechanism. Therefore, at this point it was clear that linear polarization could not be used as a reliable probe of magnetic field information in disks.

In 2018, ALMA's circular polarization mode became available after many years of development, offering a new view into disk magnetic fields via Zeeman effect measurements. This mode is still its initial stages of use, and early programs to observe TW Hydra (Vlemmings et al., 2019) and AS 209 (Harrison et al., 2021) have so far only provided conservative constraints on magnetic field strength upper limits. As circular polarization science with ALMA promises to ramp up in the coming years, the introduction of this mode has brought with it a need for modeling work to guide the interpretation of Zeeman results. Much of the work in this thesis is aimed at addressing this need, for both protoplanetary disks (Chapter 2) and disk-envelope systems (Chapter 4).

1.4.6 Historical Zeeman Measurements

Though Zeeman measurements are novel in the disk context, they have a long history of use in attempts to constrain magnetic field strengths in clouds and cores. The first detection of Zeeman emission in the interstellar medium was of H I (21-cm line), made by Verschuur (1968). In the 1980s and 1990s, a flurry of additional detections were made with single-dish telescopes. This included work using the Hat Creek 85 ft telescope to observe regions near Orion (Troland & Heiles, 1982), an expanding H I shell in Eridanus (Heiles & Troland, 1982), the Ophiuchus dark cloud complex (Goodman & Heiles, 1994), and dense H I cores (Myers et al., 1995). Among other work, Crutcher et al. (1993) used the NRAO 140 ft at Green Bank Observatory to carry out a survey of OH Zeeman toward dark clouds, and Troland & Crutcher (2008) performed an OH survey of dark clouds with Arecibo. In terms of CN observations, the IRAM 30 m telescope was used to obtain detections in several molecular cloud cores (Crutcher et al., 1996, 1999).

Perhaps the most famous result from this line of work is the plot shown in Figure 1.6, which aggregates many Zeeman detections and upper limits and compares them with the inferred column density for the associated lines-of-sight. Also overplotted is

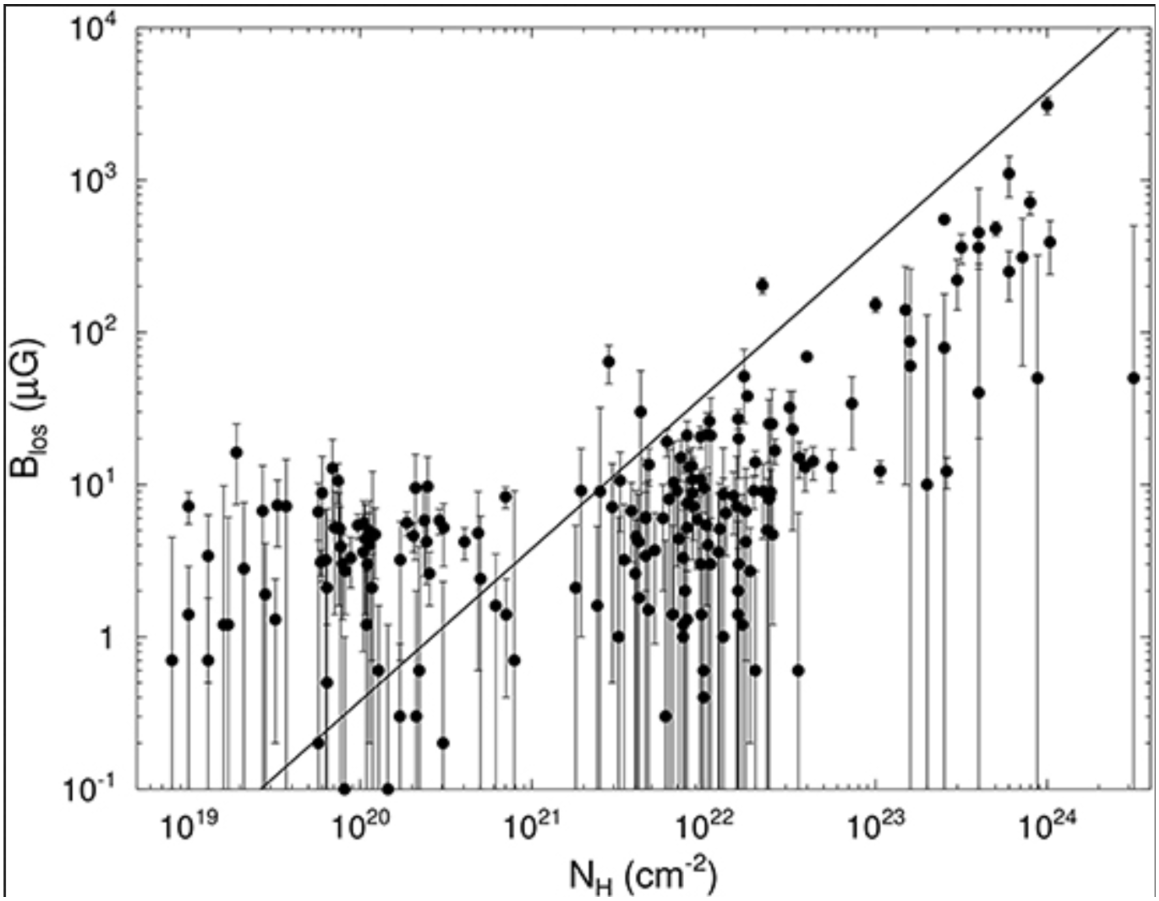

Figure 1.6: Aggregate plot of many Zeeman measurements in dense cores and molecular clouds, plotted against column densities (N_H). The diagonal straight line corresponds to a critical $M/\Phi = 3.8 \times 10^{-21}\ N_H/B$. This particular version of the figure is adapted from Crutcher & Kemball (2019).

a diagonal line corresponding to “critical" magnetic field strengths (i.e., where gravity is balanced by magnetic pressure and tension forces). The majority of low column density data points ($N_H \lesssim 10^{21}$ cm^{-2}) lie above the critical line (“subcritical”), and most high column density data points are below the critical line (“supercritical”). These results seem to suggest that magnetically supported (subcritical) dense cores are rare or do not exist.

1.5 MODELING TOOLS

The work performed in this thesis relies on the use of tools to simulate astrophysical processes. This includes modeling the 3-dimensional star forming environments themselves, as well as the emission they produce that can be detected and studied by observers like us on Earth.

1.5.1 Numerical Simulations

The molecular cloud and disk-envelope system simulations used for Chapter 3 and Chapter 4 were conducted using the grid-based `Athena` family of codes (Stone et al., 2008, 2020), which were built for the purpose of studying fluid flows and MHD. To use these codes, the user must supply a set of initial conditions for each computational cell, including initial gas density, magnetic field vector, and local velocity vector. The code then solves the partial differential equations associated with the problem to compute future time steps. Our cloud-scale simulations were run using the original `Athena` code with a static mesh refinement setup, and our envelope-scale simulations were performed using the updated `Athena++` code with adaptive mesh refinement. Additional details on the simulation setups can be found in the respective chapters for the work associated with each simulation.

1.5.2 Radiative Transfer Simulations

In our study of star formation it is not only important to be able to model the intrinsic physics of clouds and disks, but it is also important to have the tools to model the information we can obtain from observations. This information arrives to us on Earth in the form of radiation. Therefore, robust modeling of the observable emission requires us to model the production and transport of photons through the medium before they ultimately arriving at the observer.

For this task, we use 3-dimensional codes to solve the equations of radiative transfer within our modeled environments of interest. To model circularly polarized Zeeman emission, we enlist the use of the POLARIS radiative transfer code (Brauer et al., 2017a; Reissl et al., 2016). For our radiative transfer simulations of molecular line emission in a molecular cloud (Chapter 3), we use RADMC-3D (Dullemond et al., 2012). The majority of our work in this thesis assumes local thermodynamic equilibrium (LTE) conditions, though in Chapter 3 we perform a few non-LTE experiments using the large velocity gradient (LVG) approach.

1.6 Thesis Overview

The next three chapters of this thesis contain detailed accounts of three projects that model polarized emission (and by proxy, information about the magnetic field) at three different scales relevant to the process of star formation. This includes modeling of Zeeman effect emission in a protoplanetary disk (Chapter 2), modeling of linear dust polarization in a molecular cloud (Chapter 3), and modeling of Zeeman effect emission in the envelopes of disk-envelope systems (Chapter 4). These chapters are adapted, with minimal modification, from manuscripts that were published in professional astronomy journals.

Finally, in Chapter 5 the dissertation is capped off with a short summary of all of these projects, as well as a brief elaboration on some potential future work that this thesis may motivate.

CHAPTER 2

THE ZEEMAN EFFECT IN A PROTOPLANETARY DISK

This chapter is adapted from Mazzei et al. 2020, The Astrophysical Journal, 903, 20, with minimal modification.

2.1 INTRODUCTION

Protoplanetary disks (PPDs) are produced by the gravitational collapse and angular momentum mediated flattening of dense rotating cores in molecular clouds. Their initial formation and subsequent evolution will be strongly impacted by the presence or absence of a magnetic field (e.g., Li et al., 2014, and references therein). Observations of (sub)millimeter continuum dust polarization in cloud complexes reveal suggestive (e.g., “hour-glass") linear polarization patterns on $\lesssim$1000 AU scales in both low- and high- mass regimes (Girart et al., 2006; Beltrán et al., 2019). This structure is commonly interpreted as evidence of magnetic field structure in these environments, with the polarization thought to arise from alignment, through “radiative torques," of dust grains orthogonal to the local magnetic field (Lazarian & Hoang, 2007). Indeed, a magnetic field with this morphology (pinched toward the center of the collapsing core) is consistent with standard theoretical models for magnetized star formation (Galli & Shu, 1993; Fiedler & Mouschovias, 1993).

The magnetism of interstellar clouds has also been probed by Zeeman splitting measurements (e.g., of CN, OH and HI), and studies to this end (Falgarone et al., 2008; Troland & Crutcher, 2008; Heiles & Troland, 2004) reveal that cores are moderately magnetized, with mean line-of-sight $\boldsymbol{B}$-field strengths up to $\approx 30\ \mu$G. Crutcher et al. (2010) concluded through Bayesian analysis of a large sample of dense cores that the most strongly magnetized cores have approximately critical mass-to-flux ratios, suggesting a dynamically important magnetic field regulating the star formation infall process.

Since PPDs form in molecular cloud core environments, it would not be surprising if they inherit some seed magnetization as well, which could be amplified by sheering effects within the disk. It is difficult to determine the magnetic field morphology of a protoplanetary disk based on core-scale constraints, however, because a large amount of physical evolution and dynamical processing occurs as the disk forms (Li et al., 2014). For example, as gas flows onto the proto-stellar disk and local densities increase, the ionization level drops sufficiently low that non-ideal MHD effects, such as ambipolar diffusion, the Hall effect, and Ohmic dissipation, become important (for review, see e.g., Armitage, 2019). Simulation work that incorporates these physics has been successful in informing how PPDs evolve dynamically under these conditions (Turner et al., 2014), but there remains significant ambiguity in determining what constitutes a reasonable initial set-up. We do not have firm answers to some basic questions. How strong should the magnetic field be? How should it be configured?

These questions are of critical importance, as $\boldsymbol{B}-$fields remain central to the study of PPDs and are thought to play a key role in gas dynamics, which in turn controls the concentration and growth of dust grains that are crucial to the formation of planetesimals and eventually planets (Armitage, 2019). In particular, magnetic fields can cause magneto-rotational instability (MRI; Balbus & Hawley, 1991), which is widely believed to be a dominant driver of gas accretion in disk systems. This interpretation remains uncertain in light of observations that suggest ionization rates that are too low for the MRI to operate efficiently (Cleeves et al., 2015), which is consistent with the low levels of turbulence inferred in some disks (e.g., Flaherty et al., 2015). Poloidal field components may also launch jets and winds perpendicular to the disk plane (e.g., Blandford & Payne, 1982; Simon et al., 2013) that mediate gas accretion. These flows have been proposed to trigger the formation of rings and gaps (Suriano et al., 2017), and field-dependent mechanisms (e.g., “zonal flows," Johansen et al., 2009; Bai, 2013) can lead to planetesimal formation as well.

Since there is a wealth of disk physics that depends on the magnetic field strength and orientation, observational constraints are important. To date there has never been an independently confirmed direct measurement of a magnetic field in a protoplanetary disk. This is largely because linear polarization, the historically available technique for inferring magnetic information, has yielded results on the disk-scale that are difficult to reconcile with any clear $\boldsymbol{B}-$field interpretation. Though magnetic alignment is expected (Cho & Lazarian, 2007; Bertrang et al., 2017), recent work has demonstrated that a variety of other mechanisms may also produce millimeter linear polarization in disks, including self-scattering of thermal dust emission (Kataoka et al., 2015; Yang et al., 2016), radiation field (e..g “k-RAT") alignment (Kataoka et al., 2017; Tazaki et al., 2017), and gas flow alignment (Kataoka et al., 2019), none of which depend explicitly on the magnetic field geometry.

Fortunately, circular polarization is now possible with the Atacama Large Millimeter/submillimeter Array (ALMA), providing us with the opportunity to carry out “Zeeman effect" observations as a more definitive technique for accessing line-of-sight magnetic information in PPDs (e.g., Vlemmings et al., 2019). With more observations on the horizon, this paper aims to elucidate physical interpretation of disk-scale circular polarization and address the main difficulties associated with inferences of magnetic structure in PPDs. We perform full radiative transfer simulations of Zeeman observations of the CN $J = 1 - 0$ transition for several different disk set-ups (in terms of CN distribution and magnetic field configuration), then interpret the emission and assess its detectability under a variety of conditions. Finally, we address the importance of beam size, which presents challenges that are unique to circular polarization observations.

2.2 ZEEMAN EFFECT PRIMER

For a parcel of gas threaded by a magnetic field, Zeeman-sensitive species' line emission is split into two circularly polarized components:

$\sigma_+(\nu)$: line center at $\nu = \nu_0 - \Delta\nu_z$, and

$\sigma_-(\nu)$: line center at $\nu = \nu_0 + \Delta\nu_z$

where $2\Delta\nu_z = z_B B$. The value of z_B (the so-called “Zeeman-factor") is calculated as

$$z_B = 2\frac{\mu_B}{h}\bar{g}\,, \tag{2.1}$$

where μ_B is the Bohr magneton and $\bar{g}$ is the effective g-factor for the transition (Vlemmings et al., 2019). The σ_+ and σ_- line profiles have the same intrinsic width, $\Delta\nu_{\rm line}$, as determined by the typical environmental processes (e.g., thermal, pressure, natural broadening), and the Stokes I and Stokes V[1] of the emission are as follows:

$$I(\nu) = \sigma_+(\nu) + \sigma_-(\nu) \tag{2.2}$$

$$V(\nu) = \sigma_+(\nu) - \sigma_-(\nu)\,. \tag{2.3}$$

If the magnetic field is uniform along the line-of-sight and sufficiently weak such that $\Delta\nu_z \lesssim \Delta\nu_{\rm line}$ (i.e., unresolved splitting, which is expected for both molecular cloud-like and PPD environments), the Stokes V can be related approximately to the Stokes I as

$$V = \frac{dI}{d\nu}\Delta\nu_z \cos\theta_B\,. \tag{2.4}$$

Here, θ_B is the inclination of the magnetic field relative to the line-of-sight (Crutcher et al., 1993). In Figure 2.1, we demonstrate the I and V profiles obtained from Doppler broadened lines for a variety of choices of $\Delta\nu_z/\Delta\nu_{\rm line}$, showing that Equation 2.4 is an increasingly good approximation in the $\Delta\nu_z \to 0$ limit. It is worth stressing that $dI/d\nu$ mimicks the shape of the V profile only for *uniform* magnetic fields. Magnetic field configurations with significant sub-structure (e.g., toroidal or radial components) can cause the relationship to break down.

2.3 PARAMETRIC MODELING

We explore a fully parametric disk model for use in our radiative transfer simulations, to allow us to probe a variety of disk chemical and physical set-ups. We first produce "simple" models with purely vertical and purely toroidal field configurations as morphological case studies. We then invoke a more complex magnetic field geome-

---

[1] The choice $V = \sigma_+ - \sigma_-$ (instead of $V = \sigma_- - \sigma_+$) is purely a matter of convention.

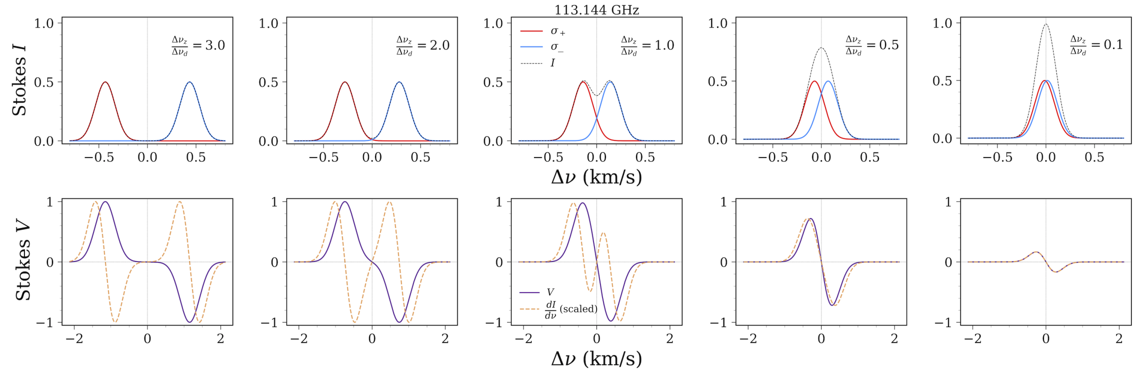

Figure 2.1: Stokes I (top) and Stokes V (bottom) profiles for a variety of choices of $\Delta\nu_z/\Delta\nu_{\rm line}$ in the case of Doppler (i.e., Gaussian) broadened lines. In this demonstration we set $T = 20$ K, $\nu_0 = 113.144$ GHz (the frequency of the CN $J = 1-0$ transiton), and calculate $\Delta\nu_d = \frac{\nu_0}{c}\sqrt{\frac{2kT}{m_p}}$. We then vary B to calculate each $\Delta\nu_z$. In the unresolved limit, the magnitude of V scales linearly with the magnetic field strength. Protoplanetary disks fall in this regime, since their field strengths are expected to be relatively weak. Note that in each plot on the bottom row, the $\frac{dI}{d\nu}$ curve has been scaled down to match the magnitude of the V curve for figure clarity.

try and vary parameters related to the distribution of our emitting molecule (CN) and the magnetic field strength. A description and list of chosen values for our parameter exploration is given in Table 2.1. Our fiducial disk structure is inspired by AS 209, a nearby ($d \approx 126$ pc), approximately solar-mass star with a minimally extincted ($A_{\rm v} = 0.8$; Avenhaus et al., 2018), moderately inclined ($i = 38°$) disk that has been observed to have CN $J = 2-1$ emission to a radial extent of ~ 200 AU (Öberg et al., 2011). These favorable observational characteristics have made AS 209 a common choice for pilot circular polarization studies with ALMA (e.g., 2018.1.01030.S, PI: R. Harrision; 2018.1.00298.S, PI: L. Cleeves). It should be noted that though we use gas and dust distributions specifically fitted to AS 209 (see Section 2.3.1), the bulk structure is not dissimilar from a variety of other disks (Andrews et al., 2009). In addition, recent sub-millimeter observations (e.g., DSHARP; Andrews et al., 2018) also show that dust sub-structure is common in PPDs. Therefore, the model presented in this work is intended to serve as an example of a “typical" disk, and we expect the general trends found here to be broadly applicable.

2.3.1 Density Structure

Our gas density distribution is based on the best-fit self-similar accretion disk solution obtained through multi-wavelength fitting of AS 209 by Tazzari et al. (2016). Their reported gas surface density profile has a power-law falloff and exponential taper

$$\Sigma_{\rm g}(R) = \Sigma_{\rm g}^0 \big(\frac{R}{R_0}\big)^{\gamma_0} e^{-\left(\frac{R}{R_{\rm c}}\right)^{2+\gamma_0}} \tag{2.5}$$

with parameter choices $R_0 = 40$ AU, critical radius $R_{\rm c} = 78$ AU, and $\gamma_0 = -0.91$.

Dust plays an important role in radiative transfer and should be modeled as accurately as possible to produce a reasonable calculation of the disk's temperature. We include two dust density distributions to simultanously account for a puffed-up, hydrostatically supported layer of small grains and a midplane-settled population of large grains. Both are set to have MRN (Mathis et al., 1977) power-law size distributions, with the small population ranging from 0.005-1 μm and the large population ranging from 0.005-2000 μm. We take the small dust to be spatially co-located with the gas, and set the large dust distribution based on the best-fit surface density profile from ALMA 1.3 mm observations (Fedele et al., 2018),

$$\Sigma_{\rm d,lg}(R) = \Sigma_{\rm d,lg}^0 \delta(R) \big(\frac{R}{R_{\rm c}}\big)^{\gamma_1} e^{-\left(\frac{R}{R_{\rm c}}\right)^{\gamma_2}} , \tag{2.6}$$

with $\gamma_1 = 0.3$ and $\gamma_2 = 2.0$. The scaling parameter $\delta(R)$ models the observed ring/gap

Table 2.1: Selected values for our parameter exploration. For each parameter we run a batch of line emission simulations of the 113.144 GHz CN $J = 1 - 0$ transition over the specified range, with all other parameters set to their fiducial values.

Parameter	Fiducial Value	Range	Description
$\mathrm{X_{CN}}$	**10^{-8}**	5×10^{-10} - 5×10^{-7}	CN abundance in slab (relative to H_2)
$R_{\mathrm{in,CN}}$ (AU)	**30**	1 - 60	Inner radius of CN slab
$R_{\mathrm{out,CN}}$ (AU)	**150**	90 - 200	Outer radius of CN slab
$N_{\mathrm{min,CN}}$ ($\times 10^{21}$ cm^{-2})	**0.5**	0.05 - 3	Minimum column density of CN slab
$N_{\mathrm{max,CN}}$ ($\times 10^{21}$ cm^{-2})	**10**	5 - 200	Maximum column density of CN slab
$B_{\mathrm{sum,0}}$ (mG)	**40**	5 - 100	Sum[a] of magnetic field components at $R = 1$ AU
$\beta_{B_{\mathrm{r}}}$	**-0.75**	-0.3 to -1.3	Power law index for radial falloff in B-field strength
f_1	**0.3**	-	$B_{\mathrm{vert,0}}/B_{\mathrm{sum,0}}$
f_2	**0.36**	-	$B_{\mathrm{rad,0}}/(B_{\mathrm{sum,0}}(1 - f_1))$
i (°)	-	0, 40, 90	Disk inclination (0° = face-on, 90° = edge-on)
f_{lg}	**0.85**	-	Fraction of M_{dust} put into the large dust population

[a] $B_{\mathrm{sum,0}} = B_{\mathrm{rad,0}} + B_{\mathrm{tor,0}} + B_{\mathrm{vert,0}}$, the sum of the radial, toroidal, and vertical magnetic field components, respectively.

sub-structure in AS 209 and is written as

$$\delta(R) = \begin{cases} \delta_{\rm G1} = 0.1 & R \in [R_{\rm G1} - hw_{\rm G1}, R_{\rm G1} + hw_{\rm G1}] \\ \delta_{\rm R1} = 0.75 & R \in [R_{\rm G1} + hw_{\rm G1}, R_{\rm G2} - hw_{\rm G2}] \\ \delta_{\rm G2} = 0.01 & R \in [R_{\rm G2} - hw_{\rm G2}, R_{\rm G2} + hw_{\rm G2}] \\ \delta_{\rm R2} = 4.5 & R \in [R_{\rm G2} + hw_{\rm G2}, R_{\rm R2,out}] \\ \delta_{\rm out} = 1.5 & R \geq R_{\rm R2,out} \\ 1 & \text{otherwise}\,, \end{cases} \tag{2.7}$$

with the gaps parameterized by best-fit radii ($R_{\rm G1} = 62$ AU, $R_{\rm G2} = 103$ AU) and half-widths ($hw_{\rm G1} = 8$ AU, $hw_{\rm G2} = 16$ AU). The outer ring has an outer radius of $R_{\rm R2,out} = 140$ AU. Outside of disk radius $R_{\rm out} = 200$ AU, we set both the gas and dust surface densities to zero. Our fiducual disk model does not include gas deficits. However, there is observational evidence from near-infrared scattered light (Avenhaus et al., 2018) and CO line transition data (Favre et al., 2019) that gas gaps may be present in AS 209 and similar disks, perhaps co-located with the dust gaps. We explore their impact on Zeeman observations in Section 2.6.3.

The 2.5-dimensional distributions used in our simulations are constructed from the above detailed 1-dimensional surface density profiles using the general conversion

$$\rho_i(R, z) = \Sigma_i(R) \frac{e^{-\frac{1}{2}(\frac{\theta_z}{h_i})^2}}{\sqrt{2\pi} R h_i}\,, \tag{2.8}$$

where $\theta_z = \arctan(|z|/R)$. The scale height h_i for each distribution allows for flaring and is parameterized as

$$h_i = \chi_i h_{\mathrm{c}} \big(\frac{R}{R_{\mathrm{c}}}\big)^{\psi}\,, \tag{2.9}$$

where h_{c} is a dimensionless critical scale height (normalized to radius), R_{c} is the critical radius of the disk, and ψ is the disk flaring parameter. For consistency with the Fedele et al. (2018) results, we choose $\psi = 0.1$, $h_{\mathrm{c}} = 0.133$, $\chi_{\mathrm{g}} = \chi_{\mathrm{d,sm}} = 1$, and $\chi_{\mathrm{d,lg}} = 0.2$, where subscripts correspond to gas, small dust, and large dust, respectively. We also set the total disk dust mass as $M_{dust} = 3.5 \times 10^{-4}\ M_{\odot}$. To determine the normalizations for our density distributions, we assume a gas-to-dust mass ratio of 100 and set the fraction of dust mass in the large grain distribution by parameter f_{lg}. Numerical integration then easily yields appropriate values for Σ^0_{g}, $\Sigma^0_{\mathrm{d,sm}}$, and $\Sigma^0_{\mathrm{d,lg}}$. In Figure 2.2 we show edge-on midplane cuts of ρ_{g}, $\rho_{\mathrm{d,sm}}$, and $\rho_{\mathrm{d,lg}}$ for our “AS 209"-like density structure.

2.3.2 Velocity Field

The bulk gas motions are assumed to be Keplerian, i.e.,

$$\boldsymbol{v}(R, z) = \sqrt{\frac{GM_*}{R}}\,\hat{\boldsymbol{\phi}}\,, \tag{2.10}$$

where $\hat{\boldsymbol{\phi}}$ is the azimuthal unit vector in cylindrical coordinates and $M_* = 0.9\ M_{\odot}$ (Andrews et al., 2009). In addition, the line emission simulations include thermal broadening and an additional turbulent component specified by the user, where we choose $v_{\mathrm{turb}} = 0.1$ km/s (Piétu et al., 2007; Chapillon et al., 2012).

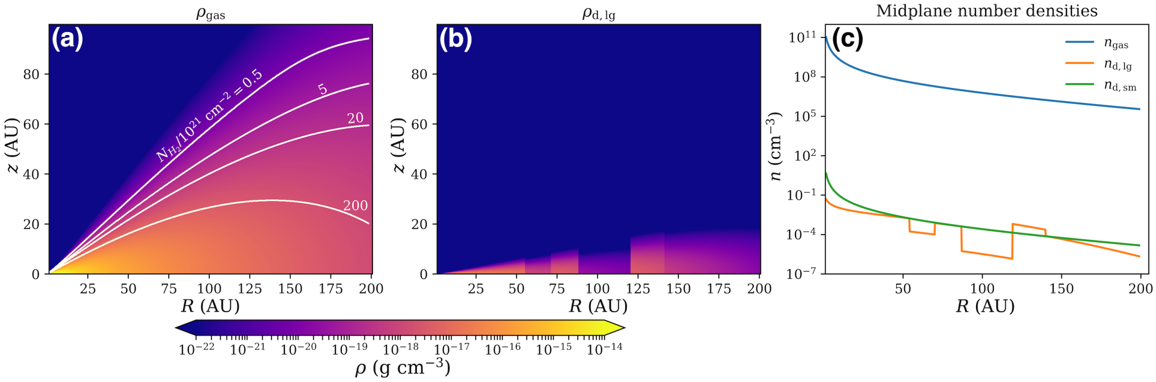

Figure 2.2: Density structure of our AS 209 based model. **Panel (a)**: Gas density, overlaid with vertically computed H_2 column density contours relative to $(N_{H_2}/10^{21}\ \mathrm{cm}^{-2})$. N_{H_2} bounds the allowed limits for CN to reside in our simulations. The small dust is co-located with the gas. **Panel (b)**: A large dust density slice. The gaps at 62 AU and 103 AU are based on previous modeling of AS 209's sub-mm dust continuum observations and aim to make our model more realistic due to the observed prevalence of substructure in disks (Andrews et al., 2018). **Panel (c)**: Midplane number densities as a function of radius for our gas, large dust, and small dust distributions.

2.3.3 Magnetic Field

We adopt a parametric description of the disk magnetic field. The magnetic field strength is set to obey a radial power-law

$$B_{\mathrm{sum}}(R) = B_{\mathrm{sum},0}\Big(\frac{R}{1\,\mathrm{AU}}\Big)^{\beta_{B_{\mathrm{r}}}}\,, \tag{2.11}$$

with B_{sum} assumed to be constant as a function of z, approximately consistent with the results of magnetized simulations from Suriano et al. (2017) that include a disk-wind. A routinely used method for deriving reasonable values for $\beta_{B_{\mathrm{r}}}$ is to invoke self-similarity between the radial gas density and magnetic field strength profiles. Taking $P \propto \rho^{\Gamma}$, it is straightforward to show (Zanni et al., 2007) that $\beta_{B_{\mathrm{r}}}$ is a function of the radial gas density power law, β_ρ:

$$\beta_{B_\mathrm{r}} = \frac{\Gamma\beta_\rho}{2}\,. \tag{2.12}$$

Adopting $\Gamma = 5/3$ and setting $\beta_\rho = \gamma_0 = -0.91$ from the AS 209 gas density distribution modeled in Section 2.3.1, we obtain $\beta_{B_\mathrm{r}} = -0.758$. We use this calculation as a guide for our fiducial value.

At each radial location in the disk, we divide the magnetic field strength into independent toroidal, radial, and vertical components as

$$\boldsymbol{B}(R,z) = (1-f_1)f_2B_\mathrm{sum}\hat{\boldsymbol{r}}' + (1-f_1)(1-f_2)B_\mathrm{sum}\hat{\boldsymbol{\phi}}' + f_1B_\mathrm{sum}\hat{\boldsymbol{z}}\,, \tag{2.13}$$

where $f_1 \leq 1$ and $f_2 \leq 1$. Also, we prescribe

$$\hat{\boldsymbol{r}}' = \begin{cases} \hat{\boldsymbol{r}} & \text{if } z > 0 \\ -\hat{\boldsymbol{r}} & \text{otherwise}\,, \end{cases} \tag{2.14}$$

and

$$\hat{\boldsymbol{\phi}}' = \begin{cases} \hat{\boldsymbol{\phi}} & \text{if } z > 0 \\ -\hat{\boldsymbol{\phi}} & \text{otherwise}\,. \end{cases} \tag{2.15}$$

Equation 2.14 is included to model the “wind-up" that occurs in the toroidal $\boldsymbol{B}$-field component due to disk rotation (per simulations, e.g. Romanova et al., 2012), and Equation 2.15 accounts for the reversal of the radial component that occurs due to inward dragging in accretion disks.

Our fiducial choices (see Table 2.1) for f_1, f_2, and $B_{\mathrm{sum},0}$ are guided by the results of disk wind simulations (Suriano et al., 2017) after 1000 orbits. A few other values are also explored to examine a diverse variety of potential magnetic field configurations.

2.3.4 CN Distribution

Chemical modeling of PPDs with many different physical structures by Cazzoletti et al. (2018) suggests that it is ubiquitous for CN to reside in a relatively thin layer in the upper and outer regions of the disk. This structure arises because CN abundance is mainly governed by the balance between ionizing far ultraviolet photons (which produce overwhelming photodissociation and photoionization at $N_{\mathrm{H}_2} \lesssim 10^{20}$ cm^{-2}) and freeze-out onto grains deep in the disk at low temperatures, $\lesssim 32$ K. Chemical models also find CN abundances are approximately constant (to within a factor of $\approx$2) within this intermediate layer irrespective of radius, modulo an inner deficit of CN. Given these constraints, we set the distribution of CN in our simulations to be a constant abundance slab. The slab is defined to have inner and outer radii, $R_{\mathrm{in,CN}}$ and $R_{\mathrm{out,CN}}$, and the vertical extent is set by upper and lower H_2 column densities, $N_{\mathrm{min,CN}}$ and $N_{\mathrm{max,CN}}$. Expected values for $N_{\mathrm{in,CN}}$, $N_{\mathrm{out,CN}}$, $R_{\mathrm{in,CN}}$, and $R_{\mathrm{out,CN}}$ are not precisely constrained, so we vary each over a few different reasonable possibilities in Section 2.5.2.

2.4 SIMULATION METHODS

We perform our simulations using the POLARIS 3D radiative transfer code (Reissl et al., 2016; Brauer et al., 2017b). Radiative transfer in POLARIS is solved using Mol3D (Ober et al., 2015), and spectral line Zeeman splitting and polarization is based on the Stokes formalism implementation by Larsson et al. (2014). We specify physical quantities in an octree format, with grid sub-division set using a variable refinement scheme based on local gas density. The densest regions have $\sim$0.2 AU resolution, with reduced resolution approximately linearly down to ~8 AU in the most diffuse parts of the disk, such as the upper atmosphere above the CN emitting region. Each simulation involves two computations: first a temperature calculation based on the dust density structure, then the CN line emission. Each step is detailed further in the following sections.

2.4.1 Temperature Calculation

The disk is heated by irradiation from a central point source, set to have luminosity consistent with a blackbody that has AS 209 stellar parameters ($R = 2.3$ R$_\odot$, $T = 4250$ K; Tazzari et al., 2016). We use 10^7 photons in this calculation to ensure good coverage in all regions of the disk. After each photon is generated (with characteristic wavelength, energy per unit time, and randomly chosen direction), it is allowed to scatter on dust grains according to an isotropic phase function. Dust heating is handled with continuous absorption (Lucy, 1999) and immediate re-emission (Bjorkman & Wood, 2001) methods. After all photons from the central star have been propagated, $T_{\rm dust}$ at each location in the disk is determined based on the temperature of local grains. We then set $T_{\rm gas} = T_{\rm dust}$ for simplicity in our parametric model; however, we note that the disk gas in the atmosphere is likely warmer than the dust temperature, due to additional UV heating from the star. This could result in generally brighter CN emission than what is predicted here.

2.4.2 Emission from CN Spectral Lines

The $J = 1 - 0$ transition of CN presents nine hyperfine Zeeman components, seven of which are strong enough to be of potential astronomical relevance. In Table 2.2 we give the rest frequency (ν_0), relative intensity (RI), and Zeeman factor (z_B) for each of these lines, as originally tabulated by Falgarone et al. (2008). For our main set of models we only consider the 113.144 GHz transition, since it is a good representative case with high relative sensitivity to B_{LOS} and a large z_B. In Section 2.6.2, we simulate (and stack) the emission from all seven lines for our fiducial disk.

Zeeman-splitting line emission in POLARIS is computed using the ZRAD extension (Brauer et al., 2017b). ZRAD makes use of energy level and transition data from the Leiden Atomic and Molecular DAtabase (LAMDA; Schöier et al., 2005) and the JPL spectral line catalog (Pickett et al., 1998). This work uses the CN hyperfine data set, with rates from Kalugina & Lique (2015). Natural, collisional, and Doppler broadening, as well as the magneto-optic effect (Larsson et al., 2014), are all considered in determining the line shape, and the final profile is calculated with a Faddeeva function solver[2]. For the turbulent component we choose $v_{\mathrm{turb}} = 0.1$ km/s (Piétu et al., 2007; Chapillon et al., 2012), or about 30% of the sound speed.

We initialize our line radiative transfer simulations with 10^5 unpolarized background photons and assume local thermodynamic equilibrium (LTE) for all level population calculations. Photons are ray traced to a 256×256 pixel detector, where the Stokes I and V of the emission are recorded. We set the detector to observe in 181 velocity channels in range $[v_0 - 6 \text{ km/s}, v_0 + 6 \text{ km/s}]$, producing 0.067 km s^{-1} resolution data. The source velocity is set to $v_0 = 0$ km s^{-1}.

2.5 RESULTS

Our POLARIS simulations yield 3D data cubes with spatially resolved I, V, and optical depth (τ) information for each pixel in each of the 181 channels. We then bin the data to 0.4 km/s wide frequency bins and convolve the data with a Gaussian kernel to simulate a $1''$ beam. From these processed data, we produce channel maps and spatially integrated line profiles.

---

[2] http://ab-initio.mit.edu/wiki/index.php/Faddeeva_Package, Copyright ©2012 Massachusetts Institute of Technology

Table 2.2: The seven strong hyperfine lines for the CN $J = 1 - 0$ transition. RI$\times z_b$ quantifies relative sensitivity to B_{LOS}.

ν_0 (GHz)	RI	z_B (Hz/μG)	RI$\times z_B$
113.144	8	2.18	17.4
113.171	8	-0.31	2.5
113.191	10	0.62	6.2
113.488	10	2.18	21.8
113.491	27	0.56	15.1
113.500	8	0.62	5.0
113.509	8	1.62	13.0

2.5.1 Vertical and Toroidal Magnetic Field Case Studies

Presented here are the results of simulations with either vertical or toroidal magnetic field configurations. All the parameters from Table 2.1 (except f_1 and f_2) are set to their fiducial values for these models, except for the maximum column density of the CN slab which we set to $N_{\mathrm{max,CN}} = 20 \times 10^{21}$ cm^{-2} here. While this choice is arbitrary, it ensures that the CN is not too optically thick such that the Stokes V is dominated by magnetic effects rather than opacity. Opacity varies due to the geometry of the CN emitting gas and sight line effects, but aside from some regions in the vertical magnetic field case when viewed face-on, $\tau < 1$ at all locations in observer space across all frequencies for these runs. Therefore, these models are reasonable approximations of the "optically-thin" limit.

Vertical Magnetic Field

The top two panels of Figure 2.3 show our results for face-on and intermediate inclination views of our purely vertical, $f_1 = 1$ and $f_2 = 0$, simulation. In the face-on case, the Keplerian rotation of the disk is in the plane-of-the-sky, so its contribution to the line-of-sight velocity field is zero everywhere. The emission is therefore spread in frequency space only due to line broadening, distributed primarily among the central three channels. Since $v_{\rm LOS,Kep} = 0$ km s^{-1} and the line-of-sight magnetic field is pointed entirely toward the observer at all locations, the $\boldsymbol{B}$-field configuration and viewing angle combination produces Stokes I and V profiles that are morphologically similar to the $\Delta\nu_z < \Delta\nu_{\rm line}$ case for the simple model (uniform magnetic field threading a uniform, non-moving parcel of gas) illustrated in Figure 2.1. Notably, in the central (zero velocity) channel the Stokes V is zero due to σ_+ and σ_- cancellation.

Unlike the face-on case, the intermediate ($i = 40^\circ$) inclination case produces line-of-sight velocity contributions. For $\Delta x_{\rm obs} < 0$, $v_{\rm LOS,Kep} > 0$, and for $\Delta x_{\rm obs} > 0$, $v_{\rm LOS,Kep} < 0$, resulting in a double-peaked Stokes I line profile. Since the magnetic field here is again pointed in the same direction across all space (the inclination simply results in a $\cos\theta_B$ reduction of its line-of-sight strength), the shape of the Stokes V profile is well mimicked by $dI/d\nu$. Each channel in the Stokes V map has positive and negative regions. This pattern arises due to the varying amounts of red and blue shifted emission, and can be understood most clearly by considering the central ($v_{\rm LOS} = 0$) channel. In this channel, all the positive V is located at $\Delta x_{\rm obs} < 0$ (where $v_{\rm LOS,Kep} > 0$) and all the negative V is located at $\Delta x_{\rm obs} > 0$ (where $v_{\rm LOS,Kep} < 0$). This flip occurs because, as demonstrated in Figure 2.1, for a parcel of gas with line-of-sight velocity v_0, the peaks of the Stokes V profile occur at $v_0 \pm \sim 0.4$ km/s (the precise value depends on the temperature and turbulence of the gas, which sets the slope of the Stokes I over frequency). As a result, the positive Stokes V emission we observe in the zero velocity channel is dominated by red-shifted regions in the disk, and the negative Stokes V arises in the blue-shifted regions. In general, for a channel centered at $v = v_{\rm channel}$ the crossover "line" from positive V to negative V occurs where $v_{\text{LOS}} = v_{\text{channel}}$.

Toroidal Magnetic Field

In the bottom two panels of Figure 2.3, we plot the results for our toroidal-only model ($f_1 = 0, f_2 = 0$). Viewed edge-on ($i = 90°$), we see the Stokes V image is clearly split into four distinct regions in most channels. The divide across the midplane (at $\Delta y = 0$) reflects the crossover from the magnetic field being oriented parallel to the Keplerian rotation to it being anti-parallel. Recall this feature aims to simulate $\boldsymbol{B}$-field “wind-up" due to disk rotation. Meanwhile, the vertical divide occurs because of the Keplerian rotation itself and is similar to the effect observed in the vertical magnetic field viewed at $i = 40°$ case. This divide is absent in the center-most channels, due to the co-locality of the velocity field and the magnetic field sign flips. Together, these effects make it such that gas with slightly negative or slightly positive line-of-sight velocity components will both produce the same handedness of circular polarization at $v_{\text{LOS}} = 0$. Note also that the shape of the spatially integrated Stokes V is no longer mimicked by $\frac{dI}{d\nu}$ due to the non-uniform magnetic field geometry. We discuss this break down in more detail in Section 2.5.2.

Viewed at intermediate inclination, the emission from the toroidal $\boldsymbol{B}$-field is still split into four distinct sub-regions in most velocity channels. This morphology arises because the CN slab traces out the disk surface, with each line of sight piercing the upper and lower surface at different radial positions, mirrored over the major axis of our axisymmetric disk. When rotated to $i = 40°$, this arrangement gives four regions of coherent emission in the central velocity channel, because the magnetic field sign flips and velocity field sign flips are co-local (similar to the scenario for the *two* regions for the edge-on case described above). A few channels, e.g ±0.7 km/s, express additional substructure. This is due to the combined effects of the emitting

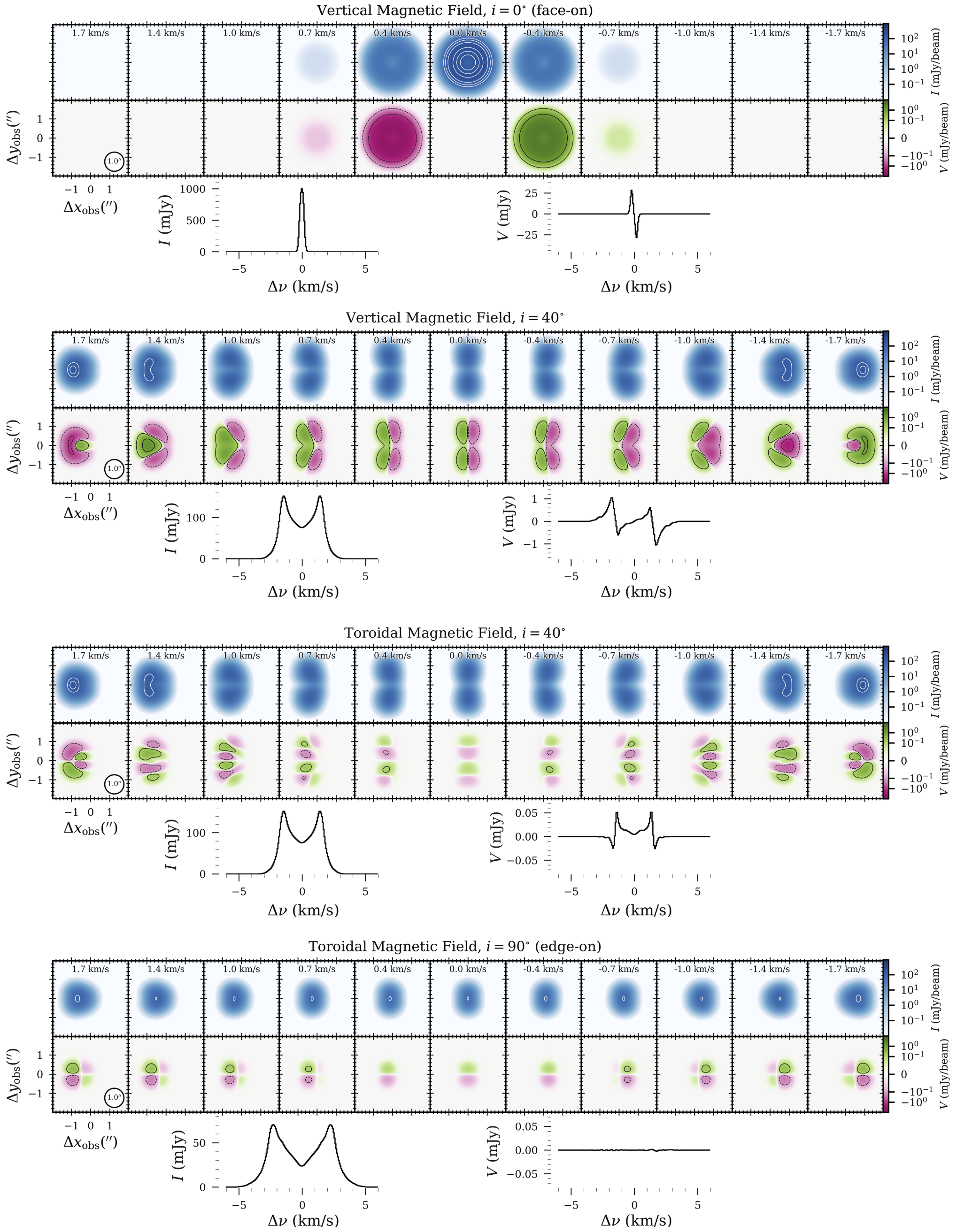

Figure 2.3: Model Stokes I and V channel maps of the 113.144 GHz CN $J = 1 - 0$ transition. The top two panels show vertical magnetic field simulations at the labelled inclinations. The bottom two panels show toroidal magnetic field simulations at edge on and 40° inclinations. Stokes V contours are drawn at ± 0.1 and ± 1 mJy beam^{-1}, and optical depth contours (over-plotted on the Stokes I maps) are drawn at τ of 0.5, 0.75, and 1. In the bottom three panels, the major axis of the disk lies along the $\Delta x_{\rm obs}$-axis. Below each set of channel maps we include disk-integrated spectra. Of note, the edge-on toroidal case shows bright Stokes V emission in the channel maps (with some regions producing > 10 mJy/beam), but roughly zero signal in the integrated profile (due to spatial cancellation). This demonstrates the importance of leveraging spatial information when observing sources with sub-structured magnetic field configurations.

layer height, the viewing geometry, and the Keplerian rotation.

2.5.2 Parameter Space Exploration

We now assess the observational impact of varying the parametric set-up of our model disk. This analysis is performed in two parts. First, we explore factors related to CN configuration and magnetic field strength (the first seven parameters listed in Table 2.1). Starting from our fiducial model (plotted in the top panel of Figure 2.8), which has a magnetic field component ratio of $B_{\mathrm{vert}} : B_{\mathrm{tor}} : B_{\mathrm{rad}} = 30\% : 45\% : 25\%$, we independently vary each parameter with the other parameters held fixed to examine *par*ameter *sli*ces (hereafter referred to as our *parsli* analysis) through the model space. This produces an easily digestible set of data to consider (as opposed to a full n-dimensional parameter space, it is instead n 1-dimensional cuts). In the subsequent section, we revert back to our fiducial model for those parameters and examine some different magnetic field geometries by varying f_1 and f_2.

parsli

We vary the following parameters within the ranges specified in Table 2.1: X_{CN}, $R_{\mathrm{in,CN}}$, $R_{\mathrm{out,CN}}$, $N_{\mathrm{min,CN}}$, $N_{\mathrm{max,CN}}$, $B_{\mathrm{sum,0}}$, and β_{B_r}. After binning the simulation data to 0.4 km/s resolution and producing channel maps, we calculate the maximum flux (Stokes I and V) and optical depth obtained for each model. The results of these computations are provided in Figure 2.5. Among the parameters related to the distribution of CN in the disk, X_{CN}, $R_{\mathrm{out,CN}}$, and $N_{\mathrm{max,CN}}$ are the most important. Sensibly, flux scales linearly with CN abundance until there are enough molecules to produce $\tau \sim 1$, at which point optical depth effects become important and some of the emission is suppressed. Extending the outer radius of the slab has a large effect due to the increase in emitting area. Extending the CN slab deeper into the disk to higher H_2 column densities (i.e., increasing $N_{\mathrm{max,CN}}$) incorporates more high density

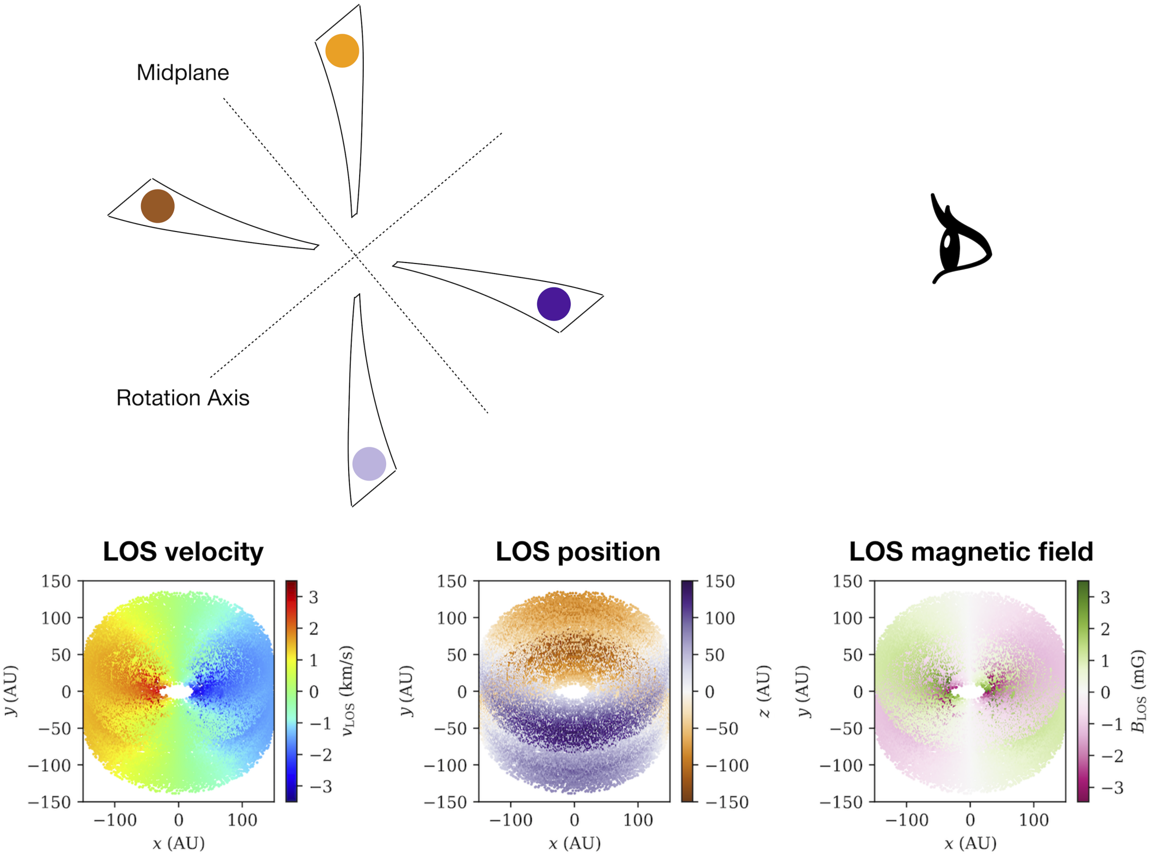

Figure 2.4: Illustration of the geometry of a disk with a toroidal magnetic field viewed at $i = 40°$. *Top:* Side view of the disk geometry. The four closed regions denote the locations where CN is placed in our model, with each one schematically color-coded to assist with interpretation of the “LOS position" plot below. *Bottom:* 3D Line-of-sight (LOS) velocity, LOS position, and LOS magnetic field maps. These visualizations are scatter plots, created by selecting 10,000 random locations in the disk, then color-coding the points accordingly and projecting them into the observer plane (notated as the xy-plane here). In the “LOS position" plot, z denotes LOS deviation from the center of the disk model space. The four CN slabs are clearly discernible, and this is why emission for the $i = 40°$, toroidal case in Figure 2.3 is distributed into four distinct clumps (especially evident in the centermost channels). The clumps alternate between positive and negative V because the magnetic field sign flips across the midplane, as illustrated in the “LOS magnetic field" panel here.

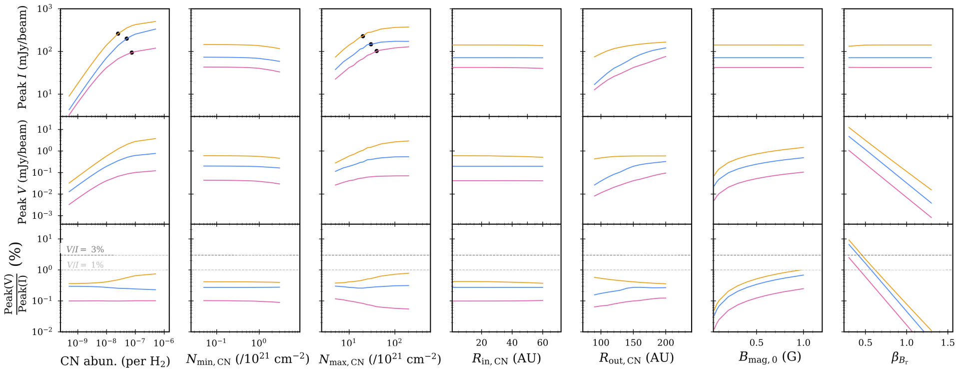

Figure 2.5: Parameter space cuts for several variables, plotting the peak Stokes I, V, and V/I for a 1" beam as a function of parameter values. Peak flux is defined as the maximum value obtained for a given Zeeman simulation spatially and spectrally. The orange, blue, and pink curves correspond to 0°, 40°, and 90° inclinations, respectively. In the top panel the black points indicate a transition to optically thick Stokes I. This only occurs for large X_{CN} or $N_{\mathrm{max,CN}}$.

gas and thus also significantly boosts CN $J = 1 - 0$ emission.

Meanwhile, there is very little dependence on the inner radius or the minimum hydrogen column density limits of the CN slab (i.e., the upper CN slab surface). This is because there is a relatively small volume of gas at small R (between the prescribed column density limits) and relatively low emissive material in the disk upper atmosphere. Ultimately, for all these scaling relationships the operative quantity being modified is the total number of emitting CN molecules added or subtracted, so expansion of the CN slab into high density regions (or by a large volume) is what produces the largest increases in I and, for a fixed magnetic field strength, V. Furthermore, we find that the magnetic quantities ($B_{\mathrm{sum,0}}$ and β_{B_r}) scale with Stokes V proportionally as expected from Eq. 2.4.

Extracting Magnetic Field Strengths

Given the complications of the disk magnetic structure, in this section we explore how the "true" value of the magnetic field put into the simulation compares to what one would extract using conventional line fitting techniques like Eq. 2.4. Included in this analysis are a subset[3] of the *parsli* simulations, including our purely toroidal (`tor`), purely vertical (`vert`), and fiducial (`fid`) models, as well as a “fiducial-like" model with a boosted toroidal component (`fidtc`).

All four configurations (summarized in Table 2.3) have the same scaling for the magnetic field strength $B_{\text{sum},0} = 0.4$ Gauss and power law dependence $\beta_{B_r} = -0.75$, and therefore have the same mean (mass weighted) magnetic field strength of $B_{\text{avg}} = 1.4$ mG within the CN emitting region. Nevertheless, these models give different amounts of Stokes V emission since the magnitude of the line-of-sight component of the magnetic field naturally changes. In Table 2.4 we list the mean line-of-sight magnetic field strength for each case, where

$$B_{\text{LOS,avg}} = \frac{\int \frac{B_z + B_y \tan i}{\sqrt{1+\tan^2 i}} \rho(\boldsymbol{r}) d\boldsymbol{r}}{\int \rho(\boldsymbol{r}) d\boldsymbol{r}}\,, \tag{2.16}$$

integrated over the CN emitting region. Due to symmetry, toroidal field components always produce $B_{\text{LOS,avg}} = 0$. Though this usefully expresses the importance of cancellation, most cancellation is due to spatial confusion rather than line-of-sight effects. To get a sense of the magnitude of all the Zeeman-relevant emission, irrespective of whether $\boldsymbol{B}$ is directed toward or away from the observer, we also report the absolute value of the line-of-sight magnetic field strength as well, again integrated over the whole CN slab. We also give the maximum Stokes V found anywhere in the observation, with corresponding profiles (Peak V vs. frequency) plotted in Figure 2.7.

We find that the strongest Stokes V emission in a given simulation is a strong function of the geometry of the underlying magnetic field. Due to the lack of spatial

---

[3] Some might say a sprig.

cancellation within a given beam, vertical $\boldsymbol{B}$-field components produce by far the largest $B_{\mathrm{LOS,avg}}$ and peak V. A face-on disk with a purely vertical magnetic yields a peak signal that is about a factor of seven larger than an edge-on disk with a purely toroidal magnetic field, even though $|B_{\mathrm{LOS}}|_{,\mathrm{avg}}$ is only ≈1.5 times larger. In terms of producing a detection, intermediate inclination and edge-on viewing geometries are only preferable for field configurations that are almost entirely toroidal. For our `fid` and `fidtc` cases, face-on observations result in emission that peaks 2.2 and 1.8 times higher than $i = 40^\circ$ observations, respectively.

Of course, due to Keplerian rotation, high inclination sources will have their emission distributed across a larger chunk of frequency space. This geometry can be advantageous for some analysis goals, like localizing the emission along a given column of gas based on an assumed velocity profile (e.g., Teague, 2019). However it can also have some disadvantages, like decreasing the line peak, thereby making detection more challenging.

As described previously, fitting the derivative of the Stokes I to the Stokes V profile is a conventional technique for inferring line-of-sight magnetic field strengths from Zeeman observations (Eq 2.4). This methodology may be applied to disk-scale observations, but we must be aware that the obtained B_{LOS} value may be significantly reduced due to field sub-structure in these environments. In Figure 2.6 we plot the spatially integrated Stokes V profiles for each of the magnetic field configurations, viewed at both face-on and intermediate inclinations. Note, the edge-on case produces $V \approx 0$ mJy for all four magnetic field geometries. This includes the toroidal field case due to the sign flip cancellation across the midplane.

In the same figure, we overplot the $dI/d\nu$ curve scaled to represent the V inferred by setting $B = 1.4$ mG (the density-weighted average field strength for these runs). In the face-on case, the shape of $dI/d\nu$ mimics the V curves well because this view

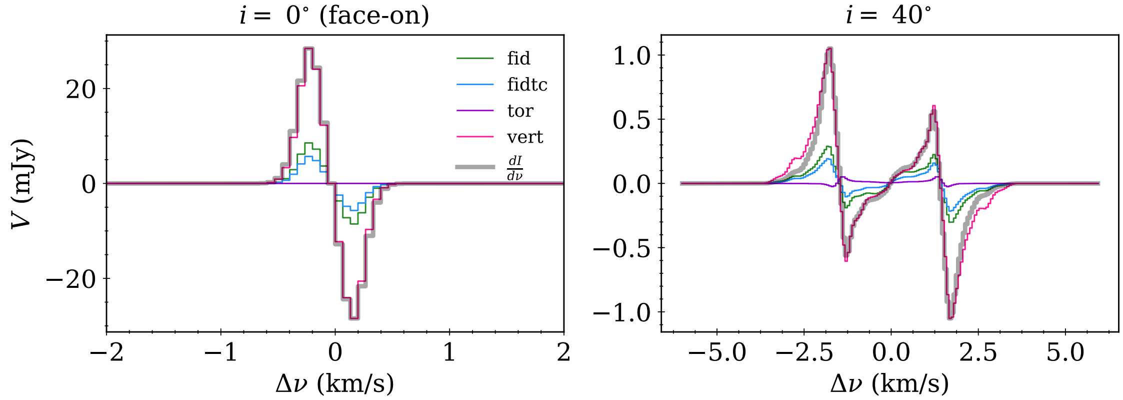

Figure 2.6: Spatially integrated Stokes V profiles for the different magnetic field geometries we considered, as viewed at $i = 0°$ and $i = 40°$. Also plotted is the derivative of the Stokes I, scaled to fit the V curve for a uniform magnetic field with a strength consistent with that put into our simulations. Magnetic field geometries with substructure produce significantly reduced Stokes V magnitudes. If the toroidal field component is large enough, it can yield a profile that is different in shape from $dI/d\nu$.

picks out the vertical field component, which is not subject to any cancellation. The `fid` and `fidtc` curves are reduced in magnitude because they have a small fraction of their $\boldsymbol{B}$-field strength put into the vertical component. At $i = 40°$, the shape of $dI/d\nu$ still reasonably matches the `vert`, `fid`, `fidtc` Stokes V profiles. This highlights the dominance of the vertical field component, even when it is down to a factor 3.5 weaker than the toroidal component (as in the `fidtc` model). However, in the fully toroidal model the profile is both substantially reduced and has a different morphology, owing to the sign flips in the magnetic field geometry. If this magnetic sub-structure is not taken into account, fitting these curves using the conventional method results in considerable underestimates of the magnetic field strength.

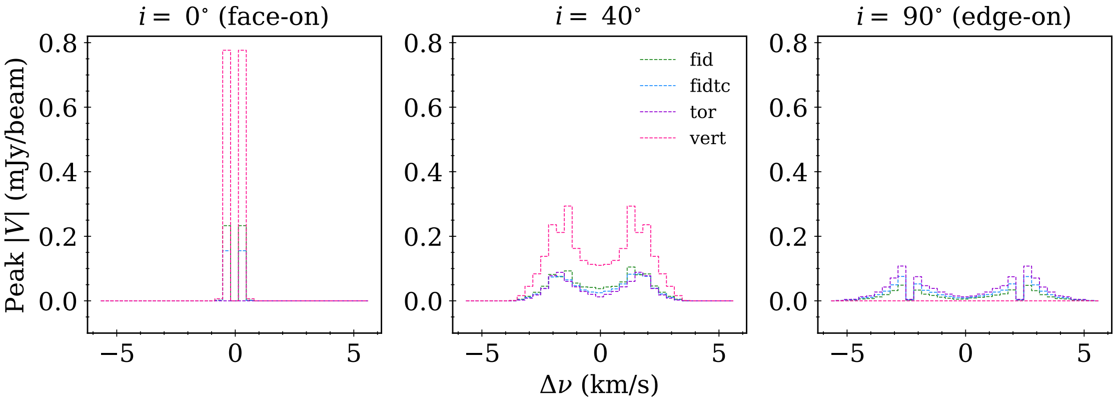

Figure 2.7: Peak $|V|$ as a function of frequency for each of the magnetic field configurations from Table 2.3. The maximum value for each of these curves (i.e., the peak $|V|$ across all frequencies) is listed in Table 2.4. These data are binned to the same resolution (0.4 km/s) as the channel maps.

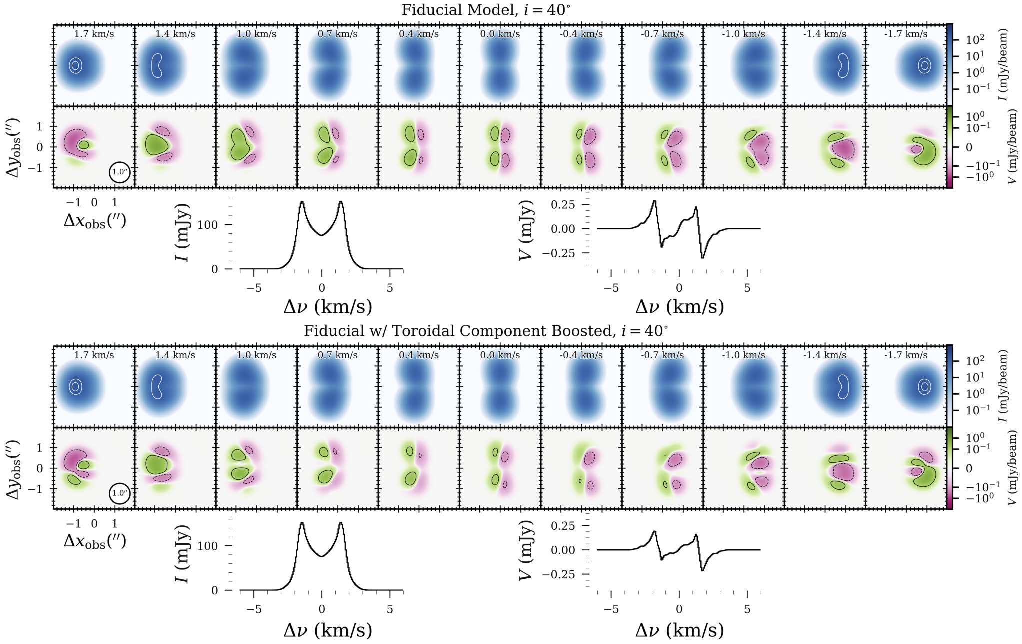

Figure 2.8: *Top panel:* Same as Figure 2.3, now for our "fiducial" case, viewed at $i = 40°$. This model has its magnetic field strength divided such that $B_{\rm vert} : B_{\rm tor} : B_{\rm rad} = 30\% : 45\% : 25\%$. *Bottom panel:* "Toroidally boosted" version of the fiducial model, with $B_{\rm vert} : B_{\rm tor} : B_{\rm rad} = 20\% : 70\% : 10\%$.

Table 2.3: The magnetic field configurations we consider in Section 2.5.2 and Section 2.6.2. Percentages represent the fraction of the total magnetic field strength allocated to each of the components.

Name	Vertical (%)	Toroidal (%)	Radial (%)
`vert`	100	0	0
`tor`	0	100	0
`fid`	30	45	25
`fidtc`	20	70	10

2.6 Discussion

2.6.1 Evidence of Magnetic Complexity in Stokes V Channel Maps

One of the principle results of this work is that channel map information from spatially resolved observations can be used to distinguish vertical and toroidal magnetic field geometries in intermediate inclination disks. The features of the emission produced in these respective case studies are individually discussed in detail in Sections 2.5.1 and 2.5.1, but we can also use them to make a broader point about identifying magnetic sub-structure in general. For the purely vertical $\boldsymbol{B}$-field geometry, each channel has exactly one region of positive V and one region of negative V. The spatial span of these regions changes for different channels (due to the Keplerian rotation of the disk), but at all velocities they are both continuous and symmetric about the major axis of the disk. We can think of this as the "unsubstructured" baseline — that is, a rotating, axisymmetric disk with a uniform magnetic field threading through it will always produce Stokes V channel map emission that looks like this. Therefore,

Table 2.4: Mean line-of-sight magnetic field strength ($B_{\rm LOS,avg}$), mean absolute value of the line-of-sight magnetic field strength ($|B_{\rm LOS}|_{\rm ,avg}$), and peak $|V|$ obtained from the channel maps for each of the magnetic field configurations we simulated. Values are reported for emission from the 113.144 GHz component only. A vertical field viewed face-on yields a peak V flux that is a factor of $\sim$7 larger than a toroidal field viewed edge-on, even though $|B_{\rm LOS}|_{\rm ,avg}$ is only a factor of $\sim$1.6 larger. This highlights the importance of cancellation for sub-structured (e.g., toroidal) magnetic field configurations.

		$i = 0°$	$i = 40°$	$i = 90°$
`vert`	$B_{\rm LOS,avg}$ (mG)	1.40	1.07	0
	$\lvert B_{\rm LOS}\rvert_{\rm ,avg}$ (mG)	1.40	1.07	0
	Peak V (mJy/beam)	0.78	0.29	0
`tor`	$B_{\rm LOS,avg}$ (mG)	0	0	0
	$\lvert B_{\rm LOS}\rvert_{\rm ,avg}$ (mG)	0	0.57	0.89
	Peak V (mJy/beam)	0	0.09	0.11
`fid`	$B_{\rm LOS,avg}$ (mG)	0.42	0.32	0
	$\lvert B_{\rm LOS}\rvert_{\rm ,avg}$ (mG)	0.42	0.37	0.46
	Peak V (mJy/beam)	0.23	0.10	0.05
`fidtc`	$B_{\rm LOS,avg}$ (mG)	0.28	0.21	0
	$\lvert B_{\rm LOS}\rvert_{\rm ,avg}$ (mG)	0.28	0.43	0.63
	Peak V (mJy/beam)	0.15	0.08	0.07

any deviation from this picture is suggestive of magnetic sub-structure.

The purely toroidal channel map is an extreme example of such deviation. We see well-defined, interlaced regions of positive and negative V emission, and the placement of these regions are not symmetric about the disk's major axis (due to the combined effects of CN positioning and viewing geometry, as illustrated in Figure 2.4). A key point here is that the morphology of the emission in the vertical $\boldsymbol{B}$-field case essentially only reflects the impact of Keplerian rotation (since the magnetic field is uniform), whereas the toroidal $\boldsymbol{B}$-field case is sensitive to the inherent nearside/farside asymmetries that arise in an inclined disk (since, unlike a uniform field, a sub-structured magnetic field is itself affected by the asymmetry). Interestingly, this is also the reason why the toroidal $\boldsymbol{B}$-field case (at $i = 40°$) does not have zero spatially-integrated V emission. Even though the disk's mean line-of-sight magnetic field strength is zero (see Table 2.4), the asymmetry results in non-zero emission for many velocity channels.

Our fiducial disk has a complicated magnetic field geometry ($B_{\rm vert} : B_{\rm tor} : B_{\rm rad} = 30\% : 45\% : 25\%$) and is intended to model a "realistic" situation. In the context of the discussion above, we can use it to make an important qualitative point about general interpretation of Zeeman observations in disk environments. Looking at the channel map for the fiducial model (given in the top panel of Figure 2.8, as viewed at intermediate inclination), it is obvious that its morphology much more closely resembles the purely vertical case than the purely toroidal case. This tells us that the observed Stokes V will be dominated by any vertical field component, if present. As a result, the shape of the integrated V profile is almost identical to that of the purely vertical model. However, as we know from the model set-up, the disk's intrinsic $\boldsymbol{B}$-field is *not* primarily vertical — only 30% of the field strength is in the vertical component. The only clear evidence of the other (sub-structured) components is the slight asymmetry in the Stokes V emission across the disk's major axis. This asymmetry is of course more pronounced if the toroidal component is boosted (as in the bottom panel of Figure 2.8), but even in that case the integrated V profile shows virtually no evidence of the non-vertical magnetic field. The channel map information therefore provides crucial context for interpreting $\boldsymbol{B}$-field orientation and strength. It is important to be aware that even small asymmetries in the emission can represent a relatively high degree of complexity (and therefore cancellation) in the disk's intrinsic magnetic field.

2.6.2 Detectability Analysis

Apart from the characteristics of the source itself, there are a few observational effects that can play a role in governing the level of detectability for our emission of interest. We first evaluate the importance of beam size, then discuss the potential efficacy of velocity-based stacking of the hyperfine transitions (listed in Table 2.2) to boost the total Stokes V flux.

Beam Size

In the case of observations for which the total emission is the quantity of interest, there is a direct proportionality between the size of the beam, θ_{beam}, and the maximum flux observed per beam. This relationship is not necessarily true for observations of the Stokes V, because the positive and negative components of the emission become more prone to cancellation when integrated over more area. Therefore, larger beams are liable to wash out signals of opposite polarity.

In Figure 2.9, we choose a representative velocity channel (0.4 km/s wide, centered at 1 km/s) and for each of the magnetic field configurations discussed in Section 2.5.2 show V emission maps using $\theta_{\text{beam}} = 0.5, 1, 1.5$ and $2''$, viewed at $i = 40°$. We also plot peak V (mJy/beam) vs. θ_{beam}. In the 100% vertical magnetic field simulation, the emission scales approximately linearly with the size of the beam. This scaling occurs because the magnetic field has uniform direction in this case, and as such there is no sub-structure to produce cancellation. In the other models we introduce toroidal (and radial) $\boldsymbol{B}$-field components, and the impact this has in suppressing signal is clear. The most striking example is the 100% toroidal case, for which we observe a turnover in peak V at $\theta_{\rm beam} \approx 0.8''$. The signal becomes almost completely washed out for very large beams. For the more complicated magnetic field geometries, the V vs. $\theta_{\rm beam}$ plots for those cases exhibit a knee at $\approx 0.8''$, the scale at which toroidal field cancellation becomes important. For larger $\theta_{\rm beam}$, the rate of increase of the V emission tapers considerably. Since simulations generally predict substantial toroidal $\boldsymbol{B}$-field components, these results suggest that $\theta_{\rm beam} \approx 0.8''$ is the most reasonable choice for observations to maximize signal and preserve good spatial resolution when little is known about the true magnetic field geometry.

Hyperfine Component Stacking

For the CN $J = 1 - 0$ transition, there are 7 observable hyperfine components. So far we have only considered the 113.144 GHz line (as a representative case), but it is in principle possible to leverage the flux from multiple lines to produce a stronger detection. In Figure 2.10 we plot the (spatially integrated) line flux results of simulations for all the transitions, performed for our fiducial model at $i = 40^\circ$. Since the lines are entirely non-blended, stacking is possible. The stacked line profile has a peak flux that is a factor of $\sim$5 larger than that produced solely by the 113.144 GHz component.

2.6.3 Sub-structured Gas Distribution

Our fiducial disk includes rings in the large dust population. As part of our modeling work we also tested disk scenarios with smooth (re-normalized to the same

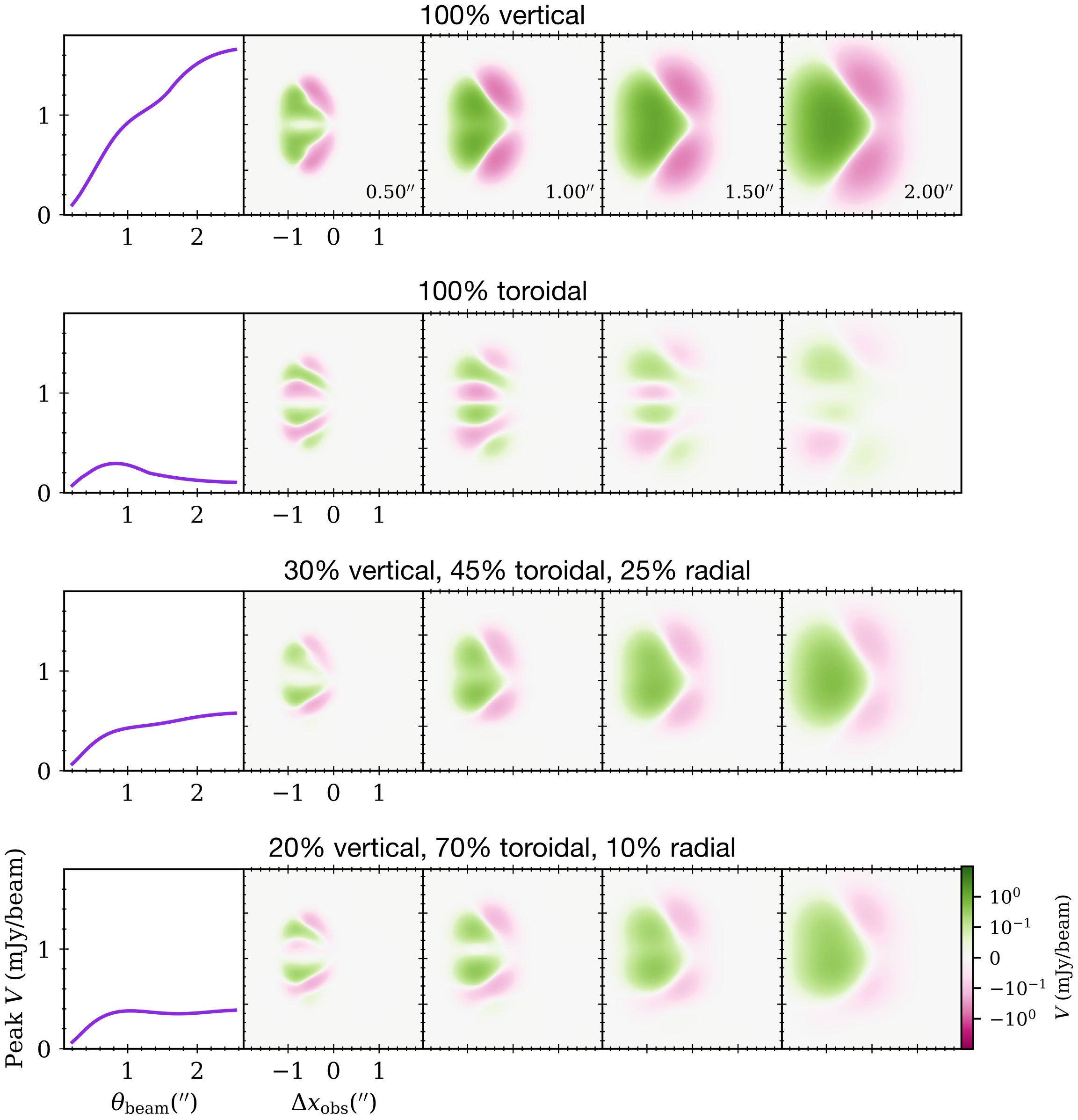

Figure 2.9: Comparison plots of a 0.4 km/s wide channel (centered at 1 km/s) for several choices beam size, viewed at intermediate (40°) inclination. Each row reflects a different magnetic field geometry. The left panel shows how the maximum observable intensity (e.g., flux coming from the brightest pixel) changes as a function of beam size. Note that in the fully toroidal case, there is a turnover in Peak V at $\theta_{\text{beam}} = 0.8$ arcsec. This demonstrates the importance of spatial cancellation in poorly resolved observations of sources with toroidally dominated magnetic fields.

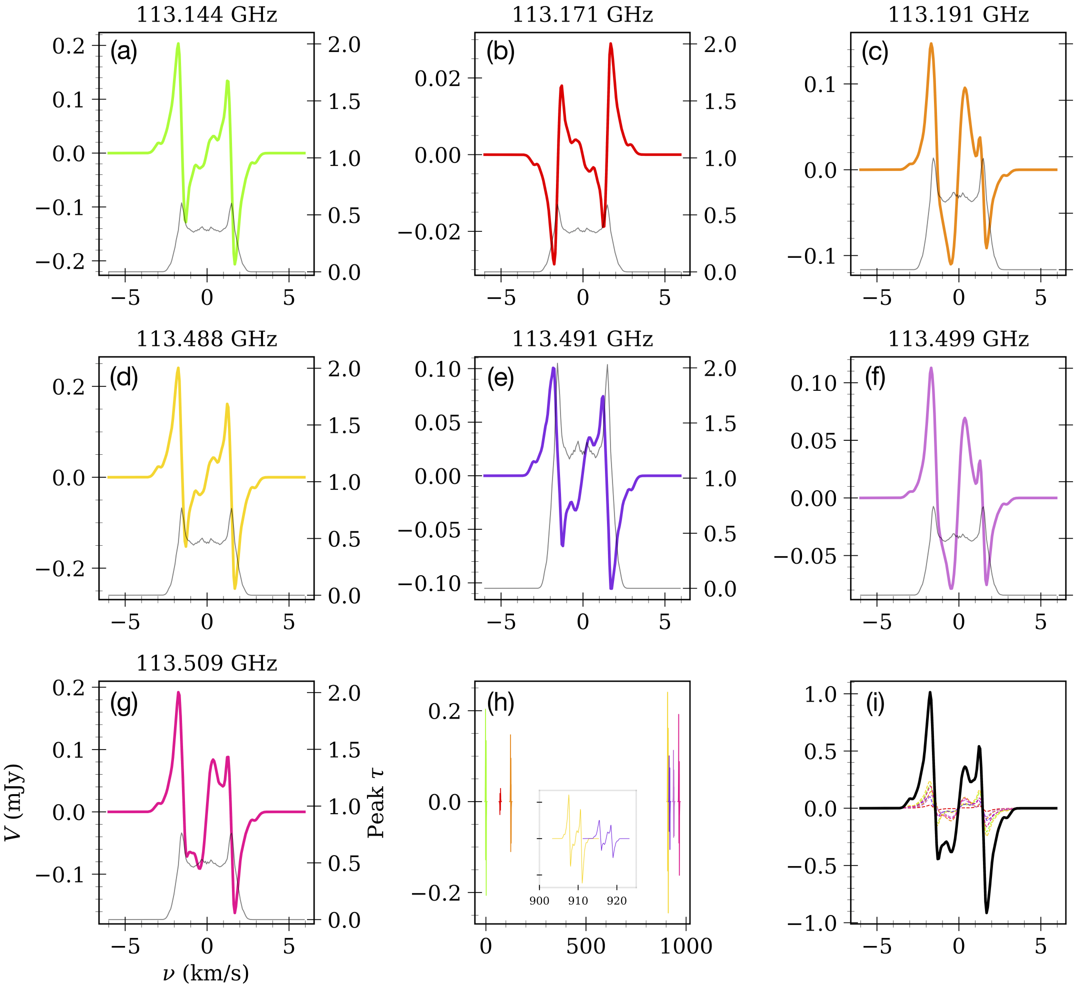

Figure 2.10: **Panels (a) - (g):** Stokes V profiles for each of the CN $J = 1 - 0$ hyperfine transitions. Also included in each panel are optical depth profiles, plotting the peak τ (across all space) found at each frequency. **Panel (h):** A plot of where the lines lie in frequency space with respect to each other. They are mostly well separated. In the sub-panel we show that the 113.488 GHz and 113.491 GHz, which are relatively nearby, are still completely non-blended. **Panel (i):** Stacked profile of all 7 lines. Note that because the 113.171 GHz transition has negative z_B, its profile should be negated before stacking.

mass) large dust distributions, and found that the presence or absence of dust sub-structure has a negligible effect on the line emission results. However, it is possible that this sub-structure may exist in the gas as well. Observations of $C^{18}O$ ($J = 1-0$) emission in AS 209 by Favre et al. (2019) show evidence of gas deficits that are spatially coincident with the dust gaps. To model this scenario, we ran additional versions of our fiducial simulations with gas density gaps carved out according to the $\delta(R)$ prescription given in Equation 2.7. The density distribution is renormalized such that the total gas mass is kept the same as it was in the original runs. In Figure 2.11 we compare the emission profiles from these sub-structured runs with the original smooth ones.

For intermediate inclination and edge-on models, the Stokes I is redistributed in velocity space when sub-structure is introduced, yielding more "peaky" profiles since more of the CN gas is constrained to specific radii. The opacity in these regions is slightly higher, exceeding $\tau = 1$ only near the peaks (this results in a $\sim$ 20% lower maximum in I than the original). For most frequencies the emission remains optically thin, but there are still differences in the profile morphology as a result of the added gas sub-structure. This is an important point to consider — in the case of sub-structured disks, it is possible that some of the features in the V profile are *not* the result of magnetic complexity. Observers should be cautious of this when searching for signatures of $\boldsymbol{B}$-field morphology in their data.

For the face-on model, the opacity increases dramatically with the addition of gaps. This is because the emission, already distributed over a relatively narrow range in frequency space (since $v_{\mathrm{LOS}} = 0$ everywhere), is now pushed to smaller regions in observer space. As a result of these optical depth effects, the I and V emission are both reduced significantly (by a factor of $\sim$2).

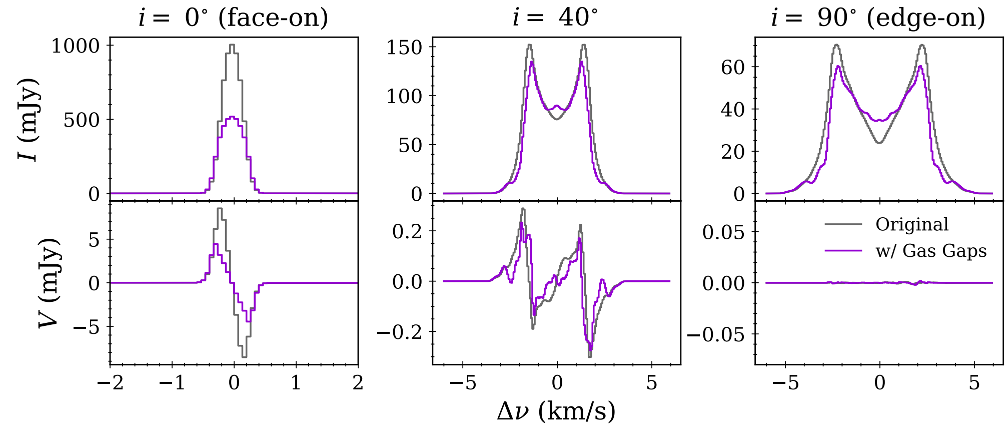

Figure 2.11: Comparison plots of the spatially integrated Stokes I and V profiles for a model with smooth gas distributions (e.g., `fid`) and one with gas gaps added. Due to increased opacity in the ring regions, the face-on view yields significantly reduced emission when gas sub-structure is introduced. This effect is present in the intermediate and edge-on cases as well, but to a smaller extent since the emission is spread over a larger range of velocity space. At $i = 40°$, the gas gaps affect the morphology of the V profile as well.

2.6.4 Comparison to ALMA Percentage Polarization Limits

ALMA's current circular polarization instrumentation is nominally stated to have a 1.8% percentage polarization limit. In the bottom row of Figure 2.5, we give percentage polarization for the models in our main *parsli* grid. Since values for I and V vary across the observer plane, we report peak values for each run. Our fiducial model yields percentages of 0.1%, 0.3%, and 0.4% for 90° (edge-on), 40°, and 0° (face-on) viewing angles, respectively.

Increasing the CN abundance or the depth of the CN slab (to larger $N_{\mathrm{max,CN}}$) increases V/I in the face-on case, and extending the maximum radius of the slab leads to larger V/I in the intermediate inclination and edge-on cases. Peak percentage polarization also scales with $B_{\mathrm{sum},0}$, of course. Increasing the values of these parameters in various combinations produces a parameter space of optimistic disk scenarios that reach the nominal ALMA limit of 1.8%. For instance, if we set $B_{\mathrm{sum},0}$ to 1.0 G (corresponding to $B_{\mathrm{avg}} = 3.5$ mG), we could produce 1.8% polarization by also increasing the CN abundance to $\approx 3 \times 10^{-7}$ (per H_2) or increasing $N_{\mathrm{max,CN}}$ to about 10^{23} cm^{-2}. It should be noted that at these high values of CN abundance and $N_{\mathrm{max,CN}}$, opacity effects will start to come into play as some regions of the disk reach $\tau > 1$.

Based on their circular polarization (non-detection) observations of TW Hydra, Vlemmings et al. (2019) suggest ALMA may be capable of substantially better polarization performance, inferring a <0.8% detection level. For our face-on fiducial model, 0.8% polarization can be reached if we set $B_{\mathrm{sum},0} = 0.8$ G, which corresponds to a mean magnetic field in the CN emitting region of $B_{\mathrm{avg}} = 2.8$ mG. This agrees reasonably well with the 2.6 mG limit Vlemmings et al. (2019) report. We note however that, as discussed above, there are also factors related to the disk set-up that can affect percentage polarization — namely the abundance of the emitting molecule and the depth of the molecular layer.

2.7 CONCLUSIONS

We simulated the Stokes I and V CN $J = 1-0$ emission arising from a ringed disk (modelled after the AS 209 disk system) with the POLARIS radiative transfer code. We produced synthetic observations viewed at face-on, intermediate ($i = 40°$), and edge-on inclinations. We varied several parameters in our model to probe how the emission changes as a function of the magnetic field configuration and the properties of the CN emitting region. Our main conclusions are as follows:

1. Vertical and toroidal magnetic field configurations produce substantially different Stokes V emission, and it is possible to distinguish them based on channel map morphology. At intermediate inclination, vertical $\boldsymbol{B}$-field components produce blotches of positive and negative V emission that are symmetric about the

major axis of the disk. Asymmetries to this end are a telltale sign of magnetic complexity, and even small ones can signify a relatively strong toroidal magnetic field component. For sources with both vertical and toroidal components, the toroidal component must be much stronger than the vertical component for it to contribute significantly to the spatially integrated Stokes V emission, unless the disk is viewed close to edge-on.

2. For our fiducial disk model, which has “realistic" distributions of magnetic field strength and CN, the maximum Stokes V signal obtained from our synthetic observations (at 0.4 km/s velocity resolution, with a $1''$ beam) is 0.6, 0.2, and 0.04 mJy/beam for face-on, $i = 40°$, and edge-on observations, respectively. Note that these values are for the 113.144 GHz transition only — considering the other hyperfine components can fruitfully improve the signal (see item 6 below).

3. The Stokes V scales with the strength of the magnetic field, and both the Stokes I and Stokes V scale with the total number of CN molecules. For our fiducial model the line emission is optically thin, but if CN exists deep enough into the disk (at column densities $\gtrsim 3 \times 10^{22}$ cm^{-2}) or if it is abundant enough ($\gtrsim 4 \times 10^{-8}$ CN molecules per H_2), the emission can transition to optically thick in some regions.

4. The traditional method for inferring magnetic field strength from Zeeman observations (i.e., fitting with Equation 2.4) must be approached with caution in disk environments, because PPDs are expected to have significant magnetic substructure. If the magnetic field has a strong vertical component, this component will be picked out effectively for face-on or intermediate inclination observations.

However, its magnitude will imply a magnetic field strength that may be significantly reduced from the true value, depending on how much of the field is distributed into the other components. For close to edge-on sources or disks with dominant toroidal fields, the spatially integrated Stokes V profile will be greatly diminished due to cancellation, and its shape will not be matched by $dI/d\nu$ due to the non-uniformity of the magnetic field. In this case, leveraging spatial information becomes crucial.

5. Choice of beam size can play an important role in the detectability of the Stokes V emission in sources with magnetic sub-structure. If the magnetic field is toroidally dominated, there is a turnover in flux per beam at $\theta_{\rm beam} \approx 0.8''$ in our model. This beam size corresponds to a physical size of ~ 100 au. Larger beams wash out the signal due to cancellation.

6. The 7 observable hyperfine components in the CN $J = 1 - 0$ suite are well-resolved in frequency space. Due to optical depth effects and differing critical densities, the profiles of these components are not all identical. Nonetheless, they are similar enough that stacking is feasible. We demonstrate that stacking can increase the total signal by a factor of $\sim$5 over just using the strongest 113.144 GHz line.

7. The presence of gas sub-structure in the disk can have important effects on the Stokes V emission, both in terms of magnitude and morphology. Face-on disks with gaps have substantially elevated optical depth (in the rings) compared to equal mass gap-less counterparts. If some regions (i.e., the rings) reach $\tau > 1$, this is liable to produce reduced emission in the spatially integrated profile. Intermediate inclination disks are also susceptible to this effect, but to a lesser

> extent since the emission is spread over a wider breadth of frequency space. As our $i = 40^\circ$ simulation shows, gas gaps in intermediate inclination sources also produce perturbations in the Stokes V profile, which could in principle be interpreted (incorrectly) as evidence of magnetic sub-structure. Observers should be cautioned of this when inferring magnetic field information from Zeeman observations.

In this work we considered one disk structure and only performed line emission simulations. Natural future extensions could include testing different density distributions (in both gas and dust) and simulating the continuum emission. Namely, one potentially important factor we have not accounted for here is that some sources may have thick dust midplanes that could block up to half of the disk, depending on the viewing geometry. This could of course reduce total emission, but also may eliminate some of the cancellation that occurs in the Stokes V emission of sub-structured magnetic field configurations, which could have interesting effects on both the morphology and detectability of the signal. In the simulations we performed for this work the midplane was optically thin at 113 GHz, so dust did not play a role in the radiative transfer beyond factoring into the calculation of the dust and gas temperature. However, future simulations of Zeeman at higher J rotational transitions should take the possibility of optically thick continuum emission into account when simulating line observations.

CHAPTER 3

LINEAR DUST POLARIZATION AND MOLECULAR LINES IN A MOLECULAR CLOUD

This chapter is adapted from Mazzei et al. 2023, Monthly Notices of the Royal Astronomical Society, 521, 3830, with minimal modification.

3.1 INTRODUCTION

All known low-mass star formation occurs in self-gravitating cores and filaments within molecular clouds. These relatively dense features are formed from diffuse interstellar medium (ISM) gas, producing local conditions that can facilitate the formation of molecular gas and eventually (in the densest regions, $n \gtrsim 10^{5-6}$ cm^{-3}) runaway gravitational collapse that leads to the birth of stars (Shu et al., 1987; McKee & Ostriker, 2007). The morphology of a molecular cloud (and the geometry of its sub-features, e.g. cores and filaments) is also influenced by the turbulent motions in the gas and the strength and relative orientation of the magnetic field (Crutcher, 2012).

The magnetic field not only restricts the flow of gas through tension and pressure forces leveraged across many scales of the cloud, but also can provide direct opposition to gravitational collapse (Mestel & Spitzer, 1956; Mouschovias & Spitzer, 1976). One of the main aims in the field of star formation theory, particularly beyond the core scale ($\gtrsim 0.1$ pc), is to develop a general theoretical understanding of the interplay between gas structure, turbulence, and magnetic fields so we may ascertain the dynamical importance of the magnetic field in regulating gas flow through the early and intermediate stages of the star formation process during the molecular cloud's evolution. A detailed understanding of the 3D magnetic field is required for this task.

Over the last several decades, theoretical studies have used magnetohydrodymaic (MHD) simulations to develop a more comprehensive understanding of the role magnetic fields play in generating the variety of star formation outcomes observed in nature. Simulations have shown that turbulence at all scales can affect the gas dynamics by forming shearing and converging flows (Ostriker et al., 2001; Nakamura & Li, 2008), with turbulence especially having the capability to produce compression that can lead to localized collapse within a cloud (Mac Low & Klessen, 2004). This in turn leads to fragmentation that yields overdense gas regions with conditions directly conducive to the formation of stars (Scalo, 1985; Ballesteros-Paredes et al., 2007). Additionally, in the ISM the magnetic energy density is expected to be approximately in equipartition with the turbulent and gravitational energy densities (Heiles & Crutcher, 2005). The magnetic field vector $\boldsymbol{B}$ has some direction, so a large-scale magnetic field introduces an asymmetrical effect on turbulence-driven gas collapse within the cloud. Particularly, magnetic pressure forces suppress the condensation of gas flows that propagate perpendicular to $\boldsymbol{B}$ (Field, 1956), allowing shock waves to only flow parallel to the local magnetic field. As a result, elongated dense gas filaments tend to preferentially form with their crests oriented orthogonal to the mean magnetic field (Hennebelle & Pérault, 2000; Hartmann et al., 2001; Inoue et al., 2007; Körtgen & Banerjee, 2015). Soler & Hennebelle (2017) calculated the gradient of the volume density, $\nabla\rho$, and compared it to direction of the magnetic field, $\boldsymbol{B}$, in a turbulent, self-gravitating MHD simulation. They found that $\nabla\rho$ and $\boldsymbol{B}$ tended to be perpendicular at low density and parallel at high density, with the value of the transition column density dependent on the strength of the magnetic field. Chen et al. (2016) observed a similar result for their analysis of cloud-scale colliding gas flows; overall, the magnetically dominated (sub-Alfvénic) post-shock region showed a preference for parallel alignment between gas structures and the magnetic field, but in the densest sub-regions (where there is a transition to super-Alfvénic conditions) there was a flip to perpendicular alignment. Notably, in the more diffuse regions of these simulations gas flows along magnetic field lines were also present, contributing to the parallel alignment in lower density regions. These "striation" features have also been seen in observations (André et al., 2014).

Given the important interplay between magnetic fields and gas structure, magnetic fields are of key observational interest. In principle, $\boldsymbol{B}$-field information may be accessed via Stokes V observations, since in the presence of a magnetic field the Zeeman Effect splits the energy levels of some molecules (e.g., CN, OH) into higher- and lower-energy circularly polarized components. The degree of the splitting is proportional to the strength of the line-of-sight magnetic field, so this effect offers a direct probe of the magnetic field. This technique has been successfully used to study the magnetization of dense cores (Falgarone et al., 2008; Troland & Crutcher, 2008; Heiles & Troland, 2004). On the cloud-scale, however, where B_{LOS} is expected to be relatively small ($\approx$10 μG or less), the circular polarization from the Zeeman effect is difficult to detect (Goodman et al., 1989; Crutcher et al., 1999, see, however Ching et al. (2022)). In this context, the most effective tool for accessing magnetic field structure is far-infrared and sub-mm linear polarization observations; the dominant source of linear polarization in the large-scale diffuse regions of molecular clouds is "radiative torque" alignment, through which rapidly spinning, effectively oblate dust grains become preferentially oriented with their short axis along the local magnetic field (Lazarian & Hoang, 2007; Hoang & Lazarian, 2009). This yields dust emission that is polarized perpendicular to the magnetic field (Davis & Greenstein, 1951).

High-resolution dust polarization data provide a means to compute a 2D map of the line-of-sight integrated plane-of-the-sky component of the magnetic field for a given observation. This technique has been used perhaps most notably by *Planck* to produce 353 GHz all-sky polarization maps at ∼10' resolution (Planck Collaboration Int. XIX, 2015). Additionally, the Balloon-born Large Aperture Submillimeter Telescope for Polarimetry (BLASTPol) has performed high-resolution observations of the Vela C giant molecular cloud ($d \approx 950$ pc). Vela C is a massive (∼5×10^4 $M_\odot$), relatively cold (≈10-20 K) cloud thought to be in an early phase of its evolution. Thus relatively unaffected by feedback from massive star formation, it is a pristine laboratory for studying the role of magnetic fields across the many scales of star formation within a cloud. During its 2012 December run, BLASTPol simultaneously observed Vela C in 250 μm, 350 μm, and 500 μm for a total of 54 hours (Galitzki et al., 2014). In the 500 μm band, these observations (with correction for ISM dust along the line-of-sight) yielded a 2.5 arcminute (∼0.5 pc, at Vela C distance) resolution map of inferred plane-of-the-sky magnetic field vectors. Future observing runs by the next generation BLAST Observatory project promise to provide even higher resolution dust polarization observations of several molecular clouds in the Southern Sky.

Soler et al. (2013) introduced the histogram of relative orientations (HRO) method for synthetic observations of 3D MHD simulations. By computing the angle between the local direction of polarization vectors with the gradient of the column density, the HRO provides a way to compare the orientation of the magnetic field with the orientation of gas structures in a 2-dimensional observer space. Using this tool, analysis of a subset of *Planck* data taken from ten nearby ($d < 450$ pc) molecular clouds revealed a transition from mostly parallel alignment between the magnetic field field and dense gas structures to mostly perpendicular alignment at $\log\left(N_{\mathrm{H}}/\mathrm{cm}^{-2}\right) \gtrsim 21.7$ (Planck Collaboration Int. XXXV, 2016). The HRO technique has also been applied to Vela C, wherein Soler et al. (2017) compared BLASTPol polarization data with *Herschel*-inferred column densities. Their results showed a preference for iso-N_{H} contours to be aligned parallel with the plane-of-the-sky magnetic field along low N_{H} sightlines, and perpendicularly aligned along high N_{H} sightlines. Fissel et al. (2019) performed a similar analysis, however rather than using column density data, the BLASTPol-inferred magnetic field was instead compared to integrated (Moment 0) line-intensity maps of nine molecular transitions observed with the Mopra telescope. The advantage of this methodology is that different molecules have different radiative transfer and opacity properties, so their emission may probe different layers of the cloud. Indeed, it was found that gas structures traced by some molecules (e.g., ^{12}CO, ^{13}CO) were preferentially aligned parallel to the magnetic field, whereas higher density tracers (such as C^{18}O, CS, and NH$_3$) showed perpendicular alignment. From these results, combined with simple radiative transfer modeling, they concluded that in Vela C the transition from parallel to perpendicular alignment occurs at $\sim 10^3$ cm^{-3}, between the densities traced by the $J \rightarrow 1-0$ transitions of ^{13}CO and C^{18}O.

These observational results suggest a need for more detailed modeling to drive physical interpretation of the gas structures probed by each molecular tracer. In this work, we perform synthetic molecular line radiative transfer and dust polarization observations of MHD simulations of a turbulent, collapsing molecular cloud threaded by a magnetic field. We then apply the HRO technique to compare the inferred molecular gas structure from a variety of molecular tracers to the magnetic field information. Over the course of our analysis, we test a variety of simulation setups to explore how changing the magnetic field strength, viewing geometry, and stage of cloud evolution affect the HRO outcomes.

This paper is organized as follows. In Sections 4.2, 3.3, and 3.4, respectively, we introduce our MHD simulation setup, synthetic polarimetry methods, and synthetic line radiative transfer methods. The details of our HRO calculations are discussed in Section 3.5. We present our main set of results in Section 4.4. This is followed by a discussion in Section 3.7, that in part focuses on an exploration of optical depth effects for a selection of molecular line observations. By calculating the location of the $\tau = 1$ surface, we develop intuition for which parts of the cloud are being traced by each molecule, thereby linking our observational results back to the underlying 3D physical environment. In Section 3.7.4 we compare a sub-set of our results with the Vela C results derived from the BLASTPol and Mopra observations. We perform a beam convolution on these selected synthetic data to facilitate a more direct comparison. The main conclusions are summarized in Section 3.8.

3.2 NUMERICAL SIMULATIONS

The simulations in this work were performed using `ATHENA`, a 3-dimensional grid-based MHD code (Stone et al., 2008). Our simulations are in full 3D with ideal MHD assumptions. Our simulation models a turbulent, initially spherical ball of dense gas, embedded in a low-density ambient environment threaded by a uniform magnetic field. This is intended to mimic a typical isolated molecular cloud, collapsing under the influence of gravity against turbulent and magnetic support. We prescribe an isothermal equation-of-state, with temperature $T = 10$ K.

Our cloud is initialized as a pseudo-Bonner Ebert sphere with number density

$$n(r) = \frac{n_0}{1 + (r/r_c)^2} \, . \tag{3.1}$$

We set the central density $n_0 = 2000\ H_2/\mathrm{cm}^3$ and choose $r_c = 0.5R$, where $R = 2$ pc is the radius of the cloud. Outside this radius the density has a sharp cutoff, linearly decreasing from $n(R)$ to the ambient density $n(R)/100$ over a shell of width $dr = 0.01R$. The cloud is placed in a box with side length $L = 5$ pc on a $256 \times 256 \times 256$ fixed grid. Therefore, each simulation cell has a width of $\sim$0.02 pc. We adopt outflow boundary conditions.

Initial gas velocities are set by prescribing a perturbation for each cell, sampling from a Gaussian random distribution with power-law turbulence $v_k \propto k^{-2}$ and the amplitude of the velocity perturbation set to $\sigma_v = 10c_s$. The turbulence is not driven.

Finally, the initial magnetic field is set as $\boldsymbol{B_0} = (0, 0, B_z)$ where B_z is parameterized by the Alfven Mach number M_A:

$$M_A = \frac{\sigma_v \sqrt{4\pi\rho_0}}{B_z} \, . \tag{3.2}$$

Here we adopt the conventional assumption that $n_{\mathrm{He}} = 0.1 n_{\mathrm{H}}$, such that $\rho_0 = 2.8 m_{\mathrm{p}} n_0$. We produce two simulation versions, one with a weaker (super-Alfvénic) initial magnetic field ($B_{z,0} = 16\ \mu$G; hereafter called Model W), and one with a stronger (trans-Alfvénic) initial magnetic field ($B_{z,0} = 58\ \mu$G; hereafter called Model S). These values correspond to $M_A = 4$ and $M_A = 1$ for Model W and Model S, respectively.

To investigate how our results change through different stages of the cloud's evolution, in this work we examine synthetic data collected from uniformly sampled snapshots of these two models, taken between 0.25 Myr and 1.25 Myr after the simulation start time. To probe different viewing geometries, we also select a variety of angles at which to observe the cloud. The orientation of an observer's line-of-sight s relative to simulation coordinate system can be parameterized with two parameters: its inclination i away from the z-axis, and its position angle PA away from the x-axis in the xy-plane. Since our simulations do not have any preference in azimuthal direction around the z-axis (i.e, the direction of $\boldsymbol{B_0}$), we can effectively sample the unique geometries of the observer space by adjusting only i and setting PA = 0. Hereafter, we will sometimes refer to the view with $i = 0°$ as the $B_{0,\mathrm{LOS}}$ view (since from this view, the direction of the initial magnetic field is along the line-of-sight), and the view with $i = 90°$ as the $B_{0,\mathrm{POS}}$ (since from this view, the direction of the initial magnetic field is in the plane-of-the-sky).

Presented in Figure 3.1 are column density maps for our simulations, as observed from the $B_{0,\mathrm{POS}}$ view and the $B_{0,\mathrm{LOS}}$ view at the five time steps we will consider in this work. These plots demonstrate the important effect that a strong magnetic field strength can have on gas dynamics within a cloud, and moreover how the orientation of the $\boldsymbol{B}$-field relative to the observer can impact the apparent gas structure even for an identical physical environment. Furthermore, the two magnetic field strengths produce different temporal evolution, which is especially evident at later times. For example, at the $t = 1.25$ Myr time step the two viewing geometries for the stronger field $M_A = 1$ simulation are clearly distinct, with the $B_{0,\mathrm{POS}}$ view showing filamentary structure orthogonal to the magnetic field. Meanwhile, the two views of the $M_A = 4$ simulation are similar. This isotropic structure formation suggests a gravitationally dominated collapse scenario in which the magnetic field has less dynamical importance.

Also of interest is the relationship between the 3D orientation of the magnetic field and density structures. Figure 3.2 quantifies this relative orientation for the $t = 0.75$

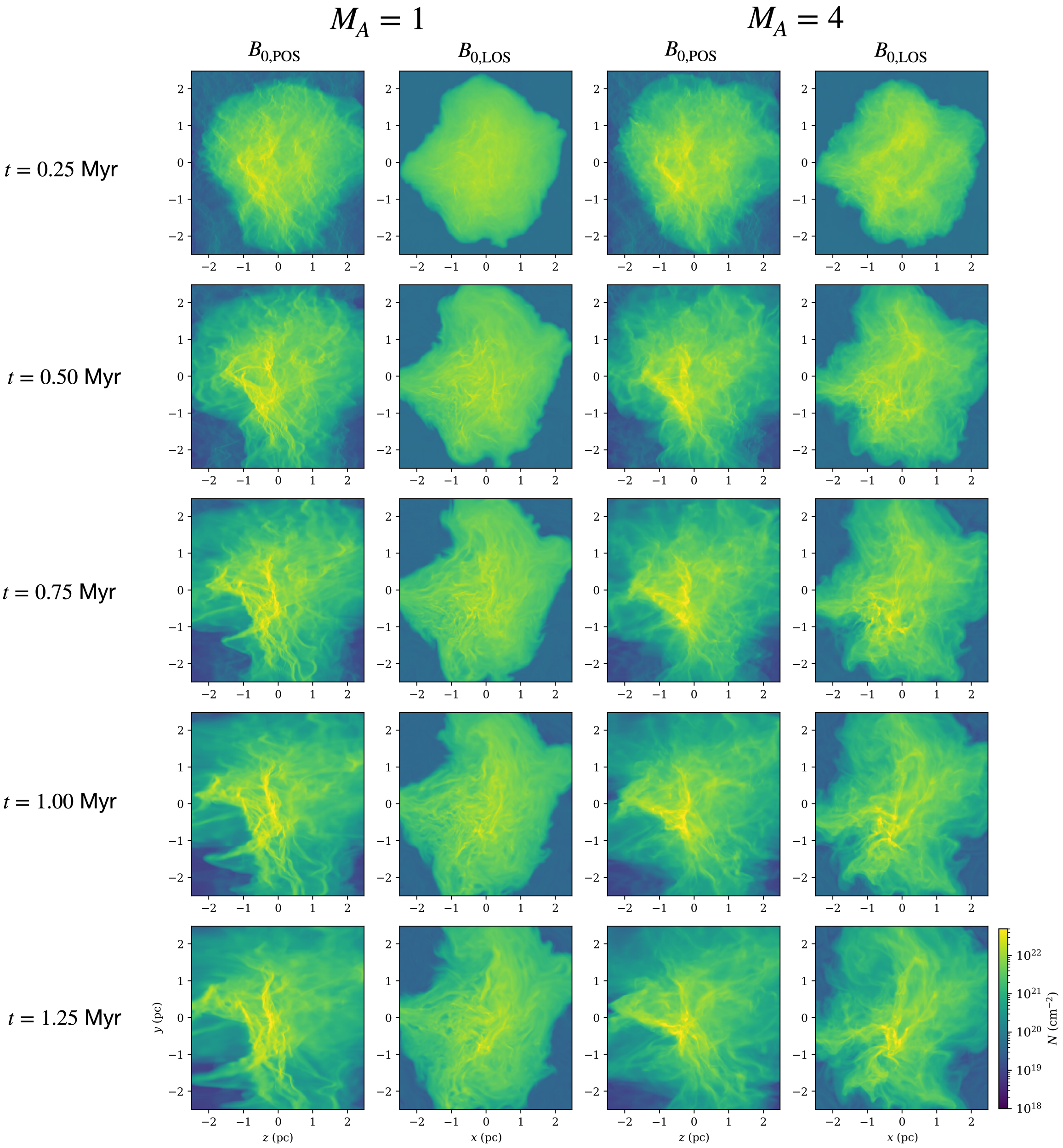

Figure 3.1: Column density maps for our strong and weak magnetic field simulations ($M_A = 1$ and $M_A = 4$), viewed with the initial magnetic field in the plane-of-the-sky ($B_{0,\mathrm{POS}}$, first and third column) and along the line of sight ($B_{0,\mathrm{LOS}}$, second and fourth column), as a function of time elapsed after simulation initialization.

Myr time step in Model S and Model W. In this 3D view, the magnetic field tends to be parallel to the orientation of local gas structures when the density is low, but the orientation begins to flip at higher densities. This effect is especially clear in Model S, wherein (due to the stronger magnetic guiding gas structure formation) there is a clear preference for perpendicular alignment at the highest densities. The transition threshold occurs at $n \gtrsim 4 \times 10^3$ cm^{-3}. Meanwhile, in Model W there is significantly less alignment preference at the highest densities. We quantify this using the HRO shape parameter ζ. Positive ζ corresponds to a preference for parallel alignment, and negative ζ corresponds to a preference for perpendicular alignment (see Planck Collaboration Int. XXXV, 2016; Chen et al., 2016).

3.3 Synthetic Polarimetry

To perform mock polarimetry on these data, we follow the literature-standard practice for the computation of synthetic Stokes parameters (e.g., Planck Collaboration et al., 2015b; Chen et al., 2016), writing the following expressions for I, Q, and U:

$$I = N - p_0 N_2 \,, \tag{3.3}$$

$$Q = p_0 \tilde{Q} \,, \tag{3.4}$$

$$U = p_0 \tilde{U} \,, \tag{3.5}$$

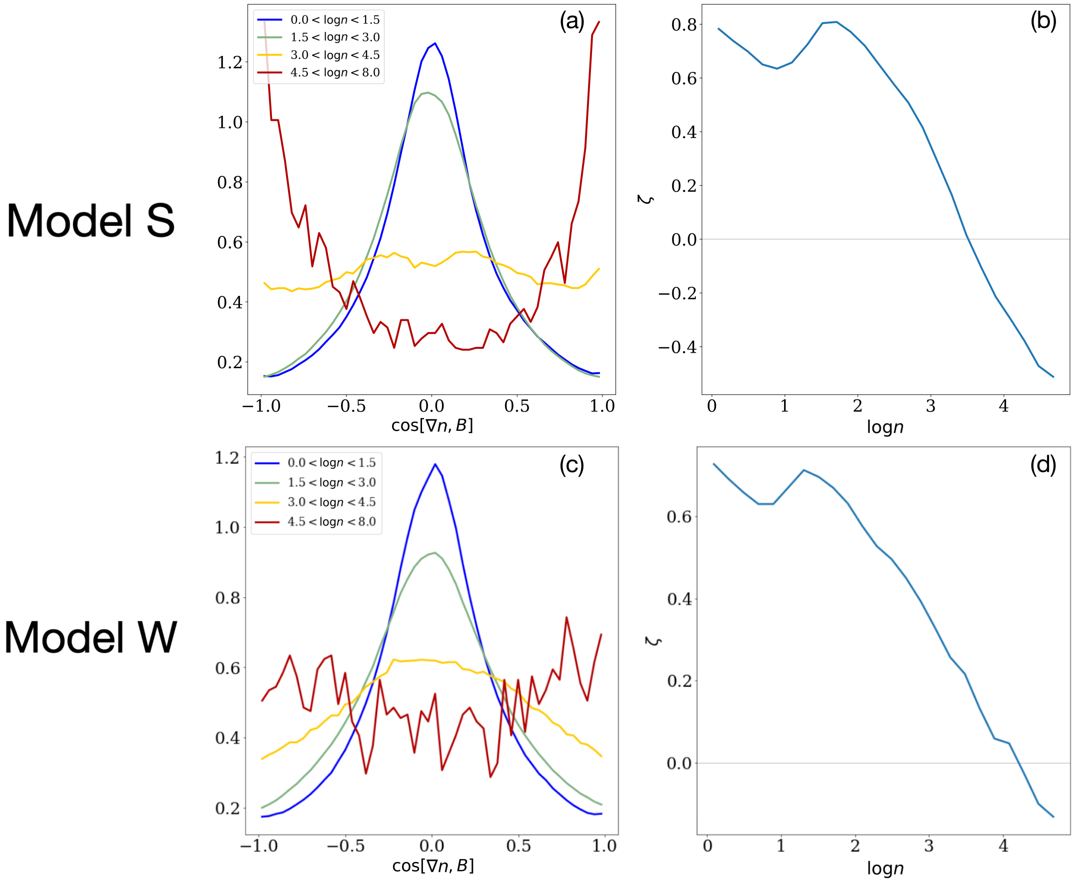

Figure 3.2: Plots depicting the 3D orientation of the magnetic field relative to density structures in our Model S (Panels (a) and (b)) and Model W (Panels (c) and (d)) simulations at the $t = 0.75$ Myr time step. **Panel (a)**: The average angle between ∇n and $\boldsymbol{B}$ for a few density bins. At low density there is a local 3D preference for parallel alignment between the magnetic field and gas structures (indicated by a value of $\cos\left[\nabla n, B\right] = 0$) . This flips to a perpendicular preference as the density is increased. **Panel (b)**: ζ as a function of ρ. In this particular frame, the crossover to perpendicular alignment occurs when $n \gtrsim 4 \times 10^3$ cm^{-3}. **Panels (c) and (d)**: Same plots for Model W, the weaker magnetic field case. There is still a preference for parallel alignment in the low density regions, but the highest density regions no longer show much preference for perpendicular alignment.

where

$$N = \int n ds \,, \tag{3.6}$$

$$N_2 = \int n\Big(\frac{B_x^2 + B_y^2}{B^2} - \frac{2}{3}\Big) ds \,, \tag{3.7}$$

$$\tilde{Q} = \int n\Big(\frac{B_y^2 - B_x^2}{B^2}\Big) ds \,, \tag{3.8}$$

$$\tilde{U} = \int n\Big(\frac{2B_x B_y}{B^2}\Big) ds \,. \tag{3.9}$$

Note that since it is usually the case that $N_2 << N$, the Stokes I generally gives a good approximate probe of column density (King et al., 2018). For this work, we adopt the literature standard value of $p_0 = 0.15$.

In performing these integrations for each pixel column along the chosen line-of-sight, we produce 2-dimensional maps of N, I, Q, and U in synthetic observer space. Polarization fraction p and polarization angle χ (measured in the plane-of-the-sky) for each pixel are then calculated as

$$p = \frac{\sqrt{Q^2 + U^2}}{I} \tag{3.10}$$

and

$$\chi = \frac{1}{2} \arctan{(U, Q)} \,. \tag{3.11}$$

Plotted in Figure 3.3 are polarization vectors for both the weak and strong magnetic field cases at the $t = 0.75$ Myr time step, as viewed with the line-of-sight along the x-axis (the $B_{\rm POS}$ view). We also provide a comparison with $\boldsymbol{B}$-field "streamlines" taken from the midplane ($x = 0$) of our simulations. Just as the magnetic field affects the gas structure, its impact is also evident in the polarization. In the stronger magnetic field case ($M_A = 1$) the $\boldsymbol{B}$-field has largely maintained its initialized orientation (i.e., $\boldsymbol{B} \approx (0, 0, B_z)$), and the polarization vectors reflect this. By contrast, there is significantly more change of direction of the $\boldsymbol{B}$-field in the $M_A = 4$ simulation. In kind, the polarization vectors are more disordered. There are also some regions with significant de-polarization. Absent any dust grain physics effects (which are not considered here), this is caused by the magnetic field being bent away from the plane-of-the-sky or being "tangled" in such a way that in projection it has less apparent local preferred direction.

Notably, these vector maps are qualitatively consistent with the 3D alignment preference data depicted in Figure 3.2. This demonstrates that the 2D observables have some power in diagnosing the physical conditions underpinning our simulations. Furthermore, the data are consistent with visual inspection of the volume density slices. This is made especially clear by panel (a) of Figure 3.3 for the strong field case. The low- and intermediate-density parts of the cloud have structures that appear to flow along the $\boldsymbol{B}$-field lines, whereas the densest filament is orthogonal to the magnetic field. In contrast, the orthogonal alignment in the densest regions is less clear in the weak field case (see panel (b) of Figure 3.3). This contrast provides a way to distinguish the strong and weak field cases through polarimetric observations (see Section 3.6.2).

3.4 Synthetic Molecular Line Observations

To perform our HRO analysis, we require a probe of gas structure. Molecular line data are a useful tool for this purpose in the cloud environment. By observing a variety of molecular tracers (each with distinct excitation conditions and optical depths), we may leverage the information available in these maps in combination with polarization

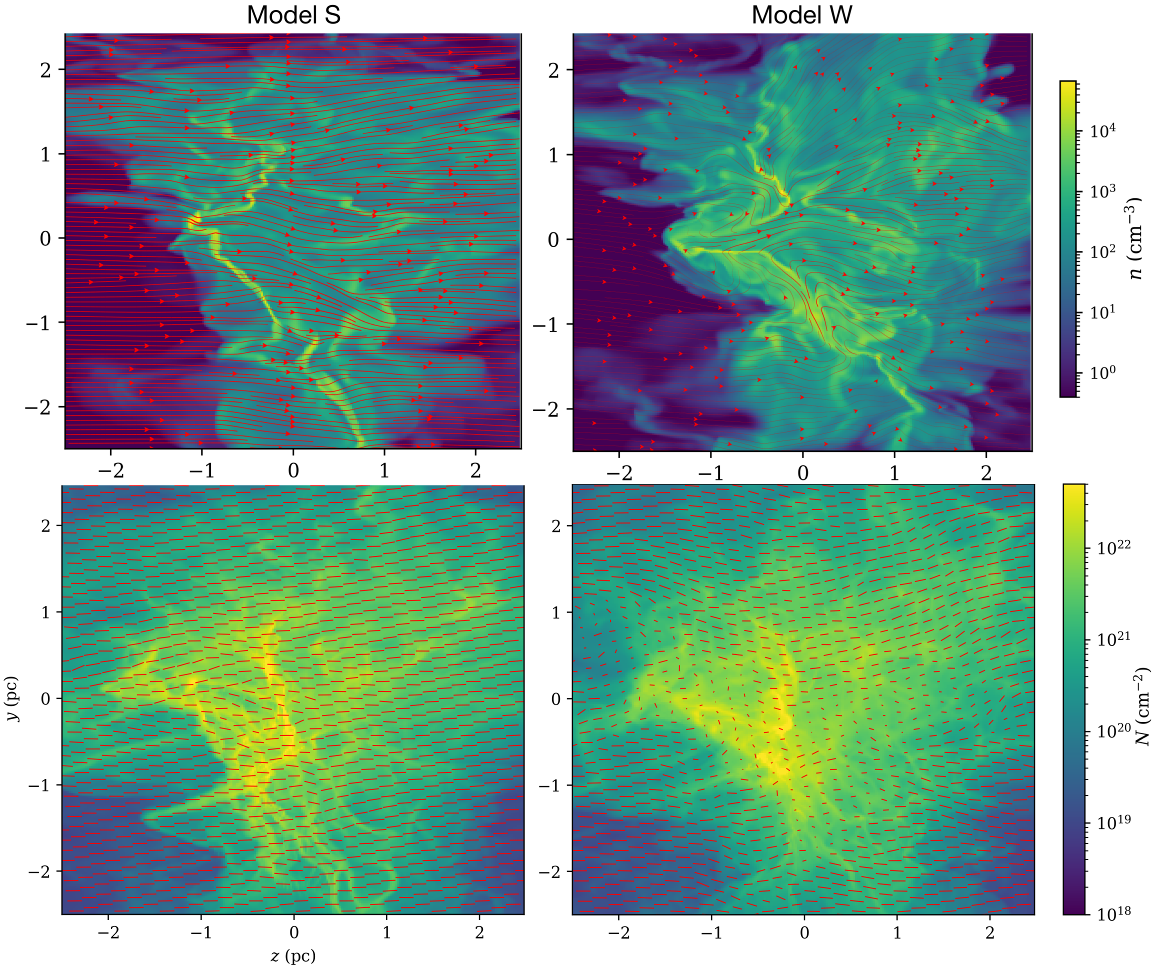

Figure 3.3: ***Panels (a) and (b):*** Volume density midplane cuts through our simulation space, for Model S and Model W, respectively, from the $t = 0.75$ Myr frame. Overplotted on each are streamlines of the magnetic field vectors in the plane. ***Panels (c) and (d):*** Corresponding polarization vector maps, plotted overtop the column density maps. There is significantly more de-polarization in the high column density regions of the weak field simulation, due to increased field line tangling in those regions.

data to learn about the relationship between the (line-of-sight integrated) magnetic field and gas structure at a variety of cloud depths.

3.4.1 Line Simulation Methods

Line radiative transfer (LRT) simulations were performed using the RADMC-3D radiative transfer code (Dullemond et al., 2012). A synthetic LRT observation requires the following physical input data for each cell in the observed 3D space:

- Gas number density n
- Gas temperature T
- Gas velocity $\boldsymbol{v} = (v_x, v_y, v_z)$
- Abundance X of the molecular species being observed
- Molecular transition data for the species being observed

In addition to n, T, and $\boldsymbol{v}$, which can be read directly from the simulation, molecular transition data were imported from the Leiden Atomic and Molecular DAtabase (LAMDA; Schöier et al., 2005). Abundance is a parameter that may be set freely. In Table 3.1, we list the fiducial values chosen for each molecular species used in this work. Our choices are based on data from a few different molecular cloud observation programs (Fuente et al., 2019; Maret et al., 2006; Morgan et al., 2013). The abundance ultimately prescribes the number density of the observed species placed in each cell of the simulation:

$$n_{\text{species}}(x, y, z) = X_{\text{species}} n(x, y, z)\,.$$

After setting up these physical parameters, we then must choose the position of the detector. We place it at a simulated distance $d = 950$ pc away from our molecular cloud (i.e., the approximate *Gaia*-constrained distance to Vela C), and adjust its orientation relative to the initial magnetic field by setting i. We set the source velocity to $v_0 = 0$ km s^{-1} relative to the observer.

To carry out each LRT calculation 10^5 unpolarized background photons are initialized behind (relative to the detector) the 3D simulated cloud, and the radiative transfer is iteratively calculated until all photons have been propagated. We find this to be a sufficient number of photons for convergence in our case. In our main set of models, we assume local thermodynamic equilibrium (LTE) for level population calculations. To assess the effect of this assumption on our results, we also perform (for a sub-set of our parameter space grid) synthetic observations that use the non-LTE large velocity gradient (LVG) approximation. For these LVG runs, a collisional partner (with corresponding number density) must be input into the simulation. We adopt the standard choices here, using H_2 as the collisional partner with $n_{H_2} = n$.

To generate images, photons are ray traced to the 256 × 256 pixel detector, and the emission is recorded. We set the detector to observe the specific intensity I_ν at $n_{\rm freq} = 111$ frequencies in range $[v_0 - 3\text{ km/s}, v_0 + 3\text{ km/s}]$ about the rest frequency of each of our lines, producing data with a velocity resolution of $\Delta\nu = 0.05$ km s^{-1}.

3.4.2 Computation of the Moment 0 Maps

For the purposes of the analysis in this work, we are interested in the integrated intensity map I of the line emission. Our simulations provide us with I_ν for each simulated frequency. Since our molecular lines are in the Rayleigh-Jeans limit, we may convert each of these values to brightness temperatures,

$$T_B(\nu) = \frac{I_\nu c^2}{2k\nu^2}\,, \tag{3.12}$$

Table 3.1: Molecular line transition information and abundance data for each species simulated in this work. Choices of lines to synthetically observe were motivated by Mopra observations from Fissel et al. (2019).

Species	Transition	Rest Frequency (GHz)	Fiducial Abundance	Abundance Reference
^{12}CO	$J = 1 \rightarrow 0$	115.2712	1.4×10^{-4}	Fuente et al. (2019)
^{13}CO	$J = 1 \rightarrow 0$	110.2013	2.3×10^{-6}	$X(^{12}\mathrm{CO})/60$
C^{18}O	$J = 1 \rightarrow 0$	109.7822	2.3×10^{-7}	$X(^{12}\mathrm{CO})/600$
N_2H^+	$J = 1 \rightarrow 0$	93.1730	5.0×10^{-10}	Maret et al. (2006)
HNC	$J = 1 \rightarrow 0$	90.6636	5.0×10^{-10}	Fuente et al. (2019)
HCO$^+$	$J = 1 \rightarrow 0$	89.1885	1.3×10^{-8}	Fuente et al. (2019)
HCN	$J = 1 \rightarrow 0$ (hfs)	88.6319	1.0×10^{-9}	Fuente et al. (2019)
CS	$J = 1 \rightarrow 0$	48.9910	2.0×10^{-8}	Fuente et al. (2019)
NH_3	(1,1)(hfs)	23.6945	1.0×10^{-8}	Morgan et al. (2013)

where c is the speed of light and k is the Boltzmann constant. To compute I (in K km s^{-1} units), we then sum over the observed frequencies :

$$I = \sum_{i}^{n_{\rm freq}} T_B(v)\Delta v\,. \tag{3.13}$$

Note that implicit in this summation is a conversion from frequency space to velocity space, where in this regime radial velocities (relative to line rest frequency ν_0) may be computed as

$$v = \frac{c(\nu_0 - \nu)}{\nu_0}\,. \tag{3.14}$$

3.5 ANALYSIS METHODS

Dust polarization observations provide us with a proxy for the plane-of-the-sky orientation of the magnetic field, and Moment 0 intensity maps from our molecular tracers give information on the plane-of-the-sky orientation of the distribution molecular gas. In this work, we use the analysis tools described below to perform pixel-by-pixel comparisons of these two sets of data.

3.5.1 The Histogram of Relative Orientations

As described in Soler et al. (2017), alignment of the magnetic field vector with the direction of an iso-I filament is equivalent to alignment of the electric field vector $\boldsymbol{E}$ with the gradient of the local intensity, ∇I. The relative orientation angle ϕ is calculated as

$$\phi = \arctan(|\nabla I \times \hat{E}|, \nabla I \cdot \hat{E})\,, \tag{3.15}$$

with $\phi = 0°$ corresponding to (local) parallel plane-of-the-sky alignment between the magnetic field and gas structure, and $\phi = 90°$ corresponding to orthogonal alignment.

To obtain a statistical understanding of the relative alignment across the observer-space, we may plot the Histogram of Relative Orientations (HRO) for all ϕ in the map.

3.5.2 The Projected Rayleigh Statistic

In addition to the HRO technique, we can use the Projected Rayleigh Statistic (PRS) to distill the information provided by the relative orientation calculation into a single parameter that characterizes the global alignment across the observer space. As described in Jow et al. (2018), the PRS Z_x is a metric that indicates whether there is a preference for parallel or perpendicular alignment within a set of independent angle measurements. Taking $\theta = 2\phi$, such that $\theta = 0$ corresponds to parallel alignment and $\theta = \pi$ corresponds to perpendicular alignment, the PRS Z_x is given as

$$Z_x = \frac{\sum_i^{n_{\text{ind}}} \cos\theta_i}{\sqrt{n_{\text{ind}}/2}} \,. \tag{3.16}$$

In our case, the independent samples are the values of θ in each pixel across the map, so $n_{\text{ind}} = 256^2$. Positive values of Z_x suggest a tendency toward parallel alignment between the magnetic field and gas filaments, and negative values of Z_x suggest a tendency toward perpendicular alignment. The larger the value of $|Z_x|$, the greater the alignment preference.

We correct for PRS oversampling using the white noise map protocol described in Fissel et al. (2019). All of our PRS measurements have a 3-sigma uncertainty of ±1.

3.6 RESULTS

To assess HRO results for a variety of scenarios, we performed LRT synthetic calculations for several different simulation set-ups by independently adjusting a few key parameters, which we split into "main parameters" (M_A, i, t, and molecular species) and "auxiliary parameters" (listed in Table 3.2). Presented in this section are the results obtained from adjusting the main parameters. This "main grid" of models establishes a baseline for understanding how the outcome of our HRO analysis is affected by the intrinsic physics of the cloud and viewing geometry effects. These computations were performed using the LTE radiative transfer assumption, with abundances set by the values from Table 3.1 and no beam convolution applied. Adjustments to the auxiliary parameters are addressed in Discussion sections 3.7.2, 3.7.3, and 3.7.4, respectively.

To establish a reference point to cross-compare the results gathered from these many parameter adjustments, we define a fiducial frame: the $t = 0.75$ Myr snapshot of Model S ($M_A = 1$), as observed in the $B_{0,\mathrm{POS}}$ view ($i = 90°$). This frame was chosen because it is a good representative frame for capturing the many elements of our simulation. It is about halfway through the runtime, at which point clear filaments have started to form and gravitational collapse is beginning to take hold, despite the initial turbulence. Furthermore, since dust polarimetry captures the plane-of-the-sky component of the magnetic field, this view gives us the best direct representation of the global $\boldsymbol{B}$-field.

Our parameter space exploration is organized as follows. First, in Section 3.6.1 we investigate how the HRO and PRS results change for different molecules, as observed in the fiducial frame and as a function of time. In Section 3.6.2 we present the results for adjustments to the magnetic field strength (i.e, Model S vs. Model W), and in Section 3.6.3 the effect of inclining $\boldsymbol{B_0}$ between 0° and 90° relative to the observer.

3.6.1 Molecular Tracers

To synergize with the existing observational data, we chose to perform synthetic observations for the nine (ground-state) molecular line transitions studied in Fissel

Table 3.2: A summary of the parameter space we explore in our synthetic observations. For most parameters, fiducial values are bolded. In addition to testing two different magnetic field strength simulations at different stages of evolution, we adjust several parameters related to the observed molecular species and viewing geometry.

	Parameter	Range Explored	Notes
Main	M_A	**1**, 4	$B_{z,0} = 58$ μG and $B_{z,0} = 14$ μG
	t (Myr)	0.25, 0.5, **0.75**, 1.0, 1.25	Simulation time
	i (°)	0, 30, 60, **90**	Inclination of $\boldsymbol{B_0}$
	Molecular Tracer	^{12}CO, ^{13}CO, C^{18}O, CS, HCO$^+$ N$_2$H$^+$, HNC, HCN, NH$_3$	
Auxiliary	Molecular Abundance	10^{-10} to 10^{-4}	Fiducual values given in Table 3.1
	Radiative Transfer Mode	LTE, LVG	Using RADMC3d
	Beam Size (pc)	**0.02,** 0.2, 2.0	Computed with Gaussian convolution

et al. (2019) for the Vela C molecular cloud (see Table 3.1 for species and rest frequencies). Moment 0 maps (at fiducial abundance) are presented in Figure 3.4, plotted at t = 0.25, 0.5, 0.75, 1.0, and 1.25 Myr. The implied gas structure varies across many of the molecules. The tracer with the highest abundance in the set, ^{12}CO, yields a map that is significantly more uniform in intensity than the others. It is optically thick, with $\tau > 1$ across much of the cloud. Meanwhile, tracers like CS and the isotopologue C^{18}O reveal much more varied structure. These maps almost exactly match the column density calculated simply by summing up the volume density along the line-of-sight. They represent the optically thin case, and are more effective at tracking the evolution of high density sub-regions as time progresses (see e.g. 3.4). Whereas the ^{12}CO map remains relatively uniform in intensity at later times, the CS map (for example) traces the condensation of mass into filaments. There are also some molecules that sit between these extremes with more intermediate τ, like HCO$^+$ and ^{13}CO.

HROs for Molecular Tracers

Shown in Figure 3.5 are the HROs computed using the intensity gradients of the maps in Figure 3.4. Histograms with negative slopes (i.e., more counts in low ϕ bins) indicate a preference for parallel alignment between molecular structure and the magnetic field, and histograms with positive slopes (i.e., more counts in high ϕ bins) indicate a preference for perpendicular alignment. In addition to HROs that incorporate all the pixels in the synthetic observation (plotted in black), we also include versions that only use the 10% lowest intensity cells and the 10% highest intensity cells.

Starting with the black ("all cells") curves, we can observe two notable trends. First, there is in general a clear distinction between ^{12}CO and all the other tracers. At

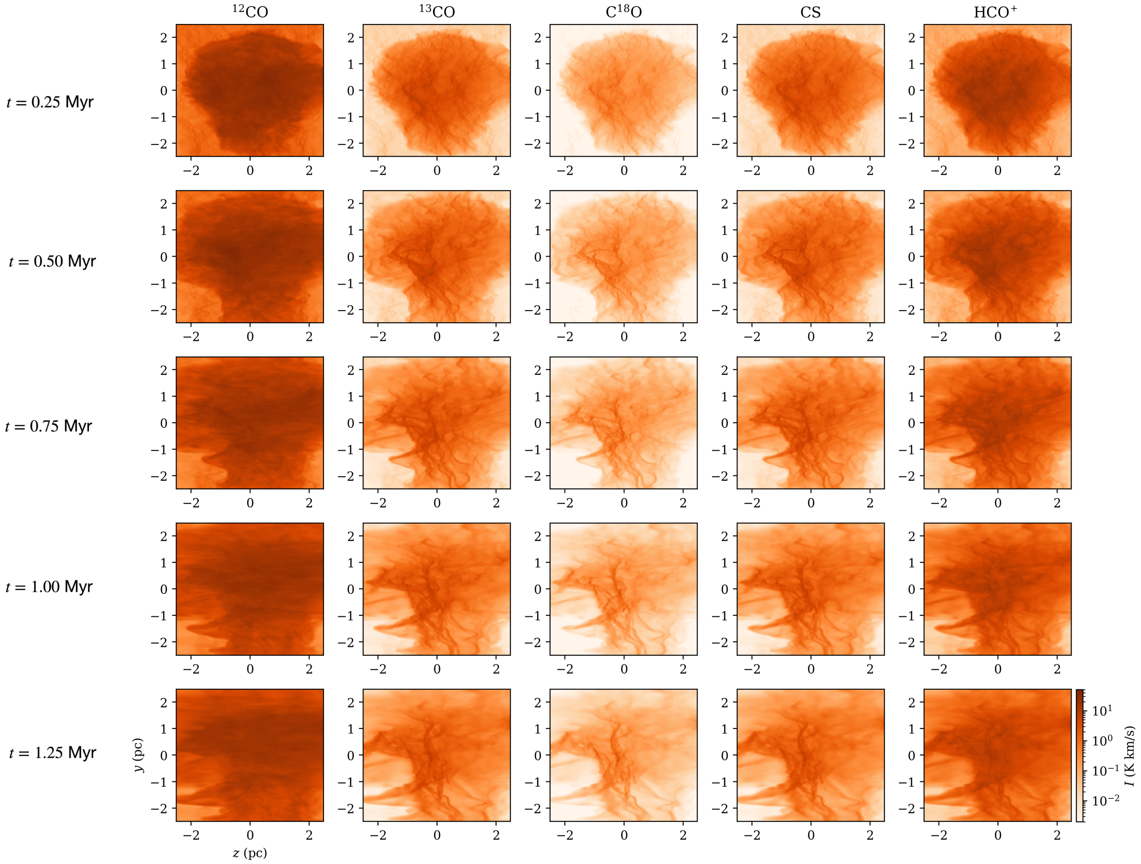

Figure 3.4: Moment 0 Maps for a selection of our modeled tracers, viewed with the magnetic field in the plane-of-the-sky and plotted at the same timesteps shown in Figure 3.1. The difference in distribution of intensity across the tracers is clear. In ^{12}CO, for example, it is not possible to see any of the signature of high density filamentary structure that is present in the other CO isotopologues.

early times ($t = 0.25$ Myr), ^{12}CO has a slightly negative slope (i.e., a slight preference for parallel alignment), while the others have a slight positive slope. At this point in the simulation, the cloud still has relatively little density contrast compared to later in its evolution (excluding the ambient low-density gas outside the main cloud), because it takes time for density structures to fully develop out of the turbulence imposed at the start of the simulation. However, some moderately high-density filaments have started to form with their ridges mainly orthogonal to the magnetic field. As reflected in the intensity maps, the higher density tracers like C^{18}O and CS pick up these filaments, producing a modest preference for perpendicular alignment. Meanwhile, these filaments are not present in the ^{12}CO emission, and as a result it does not take on the same HRO shape. Its slight preference for parallel alignment is due to a somewhat subtle effect. As demonstrated in Xu et al. (2019), the field-aligned filaments in the low-density regions are a natural consequence of the magnetically induced anisotropy in the cloud turbulence. Similar filaments are also found in other simulations, such as Chen et al. (2017). These "striations" are visible in the ^{12}CO maps, running parallel to the global $\boldsymbol{B}$-field direction along the z-axis.

The second clear trend we see in the "all cells" HROs is that as time advances the tendency toward parallel alignment is enhanced. This is present for all molecules observed, and the cause is two-fold. The main effect is that as time progresses, the mass becomes more concentrated as it is transported into the filaments near cloud center. As a result the majority of the volume becomes low-density, and alignment preference is dominated by the magnetically-aligned striations. The secondary effect, which leads to the same result, is that the cloud expands over time. This, again, results in more of the volume of the simulation box being occupied by low density gas flowing toward the filaments.

The global HRO shape is largely determined by what fraction of the synthetic observation is occupied by low-density striations vs. higher-density filaments. As the pink histograms in Figure 3.5 show, however, a different trend is revealed when we only consider the top 10% of cells by intensity. In this case, the high density tracers show HROs with more perpendicular alignment as time progresses. Effectively, with this emission cutoff it is possible to capture the perpendicular alignment in the filaments without having the lower-density regions dilute the overall HRO result. Meanwhile, the HRO slope for ^{12}CO remains about the same as for the "all cells" case. This is because the ^{12}CO is too optically thick to probe the higher density filaments (see further discussion in Section 3.7.1).

PRS Results for Molecular Tracers

HROs are useful for visualizing alignment preference across the observer space. The PRS distills this down to a single number, giving us a sense of global alignment between the magnetic field and molecular structure in a particular snapshot. To understand how this quantity changes as the cloud evolves, in panels (a) and (b) Figure 3.6 we plot Z_x as a function of time for each of our tracers (using the fiducial model), for the cases where we use all cells and just the top 10% of cells in the computations, respectively. This plot clearly illustrates some of the general trends discussed in the previous section. In the "all cells" plot, the PRS systemically increases for all molecules, and at later times (when gravitational infall begins to dominate) Z_x is large (>10) for all tracers. Meanwhile, in the high-intensity version the high density tracers remain with a negative PRS throughout the cloud evolution. This, again, is a reflection of the perpendicular alignment preference that persists in the cloud's high-density filaments. Note that, compared to all the other tracers besides ^{12}CO, HCO$^+$ has a relatively high PRS. This is because of the selected abundance, a point we discuss in more detail in Section 3.7.2.

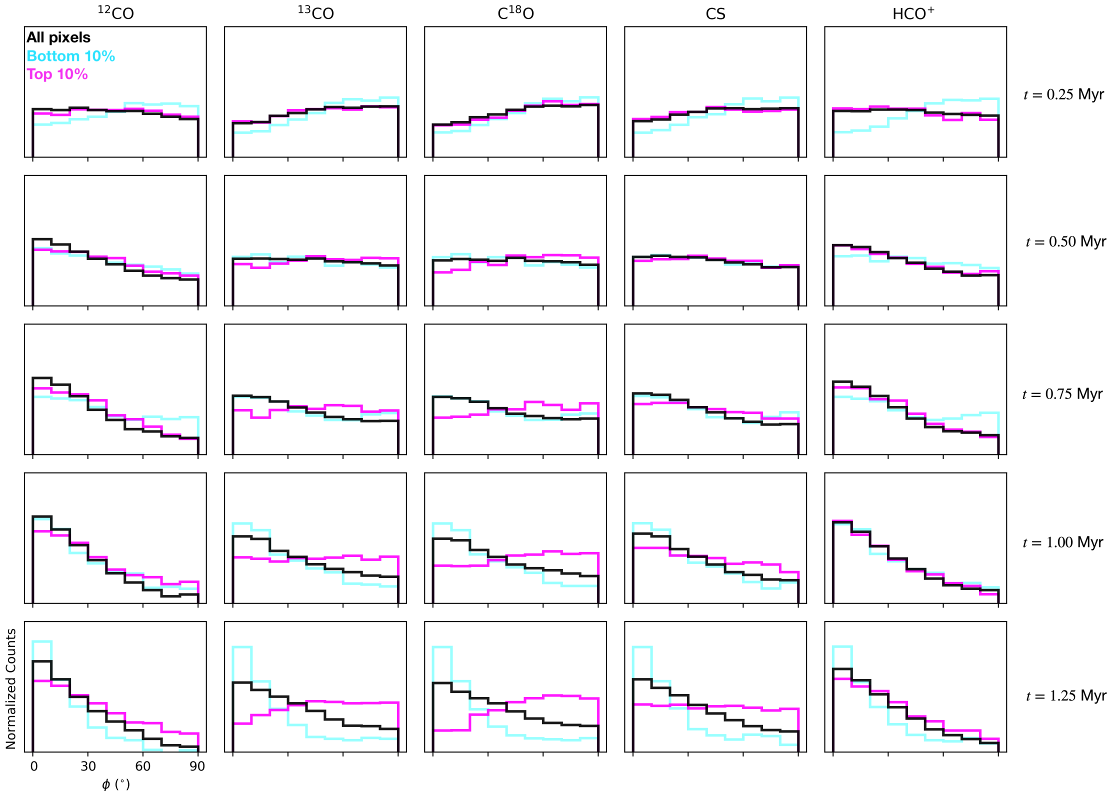

Figure 3.5: Histograms of relative orientation for the same subset of tracers shown in Figure 3.4. Included are HRO results that include all observer-space cells in the computation (black), the top 10% of cells in molecular intensity Moment 0 map value (pink), and the bottom 10% of cells in molecular intensity Moment 0 map value (blue). As discussed in the text (Section 3.6.1), several of the tracers generally show a preference for perpendicular alignment (indicated by a positive HRO slope) in the highest intensity cells, as expected for dense filaments threaded by a strong magnetic field (as in panels (a) and (c) of Figure 3.3). The major exception to this is ^{12}CO, which universally shows a strong preference for parallel alignment.

3.6.2 Magnetic Field Strength

Here we compare the results obtained for Model S (the fiducial model) and Model W, which has a factor of four weaker magnetic field strength. Panels (c) and (d) of Figure 3.6 show the PRS vs. time for each of these simulations. There is a substantial difference in alignment preference between the two models, especially when only the highest intensity cells are considered. Considering all pixels of the synthetic maps (left panels in Figure 3.6), both models show a tendency toward higher Z_x at later times, as the simulation becomes more gravitationally dominated. This effect is mainly leveraged on the lower intensity regions, however, as discussed in the previous section. In the top 10% of cells case, the difference between ^{12}CO and the high density tracers is absent in Model W, except at the very earliest times when the magnetic field is still roughly uniform (as prescribed by the initial conditions). As the simulation progresses, the weaker magnetic field of Model W is tangled by turbulent gas flows and its orientation becomes essentially random. As a result, none of the HROs have any correlative preference. This result shows the utility of this method in diagnosing magnetic field strength, as alignment preference between polarization vectors and molecular structure (and moreover, parallel vs. perpendicular preference in low- vs. high-density tracers) only appears when the magnetic field is sufficiently strong to have dynamical importance.

It is also notable that the parallel alignment observed in the "all cells" cut (which contains mostly low-intensity cells) persists for both the strong and weak field simulations. In both cases, the polarization vectors in the low-intensity regions are dominated by contributions from low-density gas, where density structures tend to lie parallel to the plane-of-the-sky magnetic field orientation. For ^{12}CO, this is the case even in pixels that include high-density gas (see the pink curves in Figure 3.5).

These results suggest that, generally, the bulk orientation of the magnetic field in diffuse regions of the cloud may be inferred just from the intensity gradients. Therefore, methods that rely solely on this information, such as the intensity gradient technique (Hu et al., 2019a), should have significant power in mapping out the magnetic field in the outer layers of a cloud, even when the magnetic field is not particularly strong. Of the tracers we tested, ^{12}CO is the best option for this task since it explicitly probes the low-density gas due to optical depth effects (see Section 3.7.1).

3.6.3 Inclination Effects

Since dust polarimetry only probes the plane-of-the-sky component of the magnetic field, viewing orientation has an impact on observed HRO outcomes. Furthermore, if the magnetic field is strong enough to regulate gas flows then the observed gas structure will also be affected.

First, we can compare the two inclination extremes - the $B_{0,\mathrm{POS}}$ case (i.e., the fiducial model, with $i = 90°$) versus the $B_{0,\mathrm{LOS}}$ case ($i = 0°$). The PRS as a function of simulation time for these cases are plotted in panels (a)-(b) and (e)-(f) of Figure 3.6, respectively. Whereas the magnetic field in the plane-of-the-sky orientation showed significant secular evolution of the PRS and different alignment preference for the low- and high-density tracers (in the the "all cells" version and the top 10% cut), these effects are entirely suppressed when the bulk field is along the observer's line-of-sight.

For the fiducial timestep, we also computed Z_x for each of our tracers at a few intermediate inclinations (60° and 30°) using Model S. The results of this exploration are presented in Figure 3.7. The outcome is largely consistent with expectation for a mostly rigid magnetic field. For the calculation that considers all cells of the simulation (i.e, is dominated by the low-density regions, where we expect more parallel alignment), the PRS decreases roughly linearly as the plane-of-the-sky component of

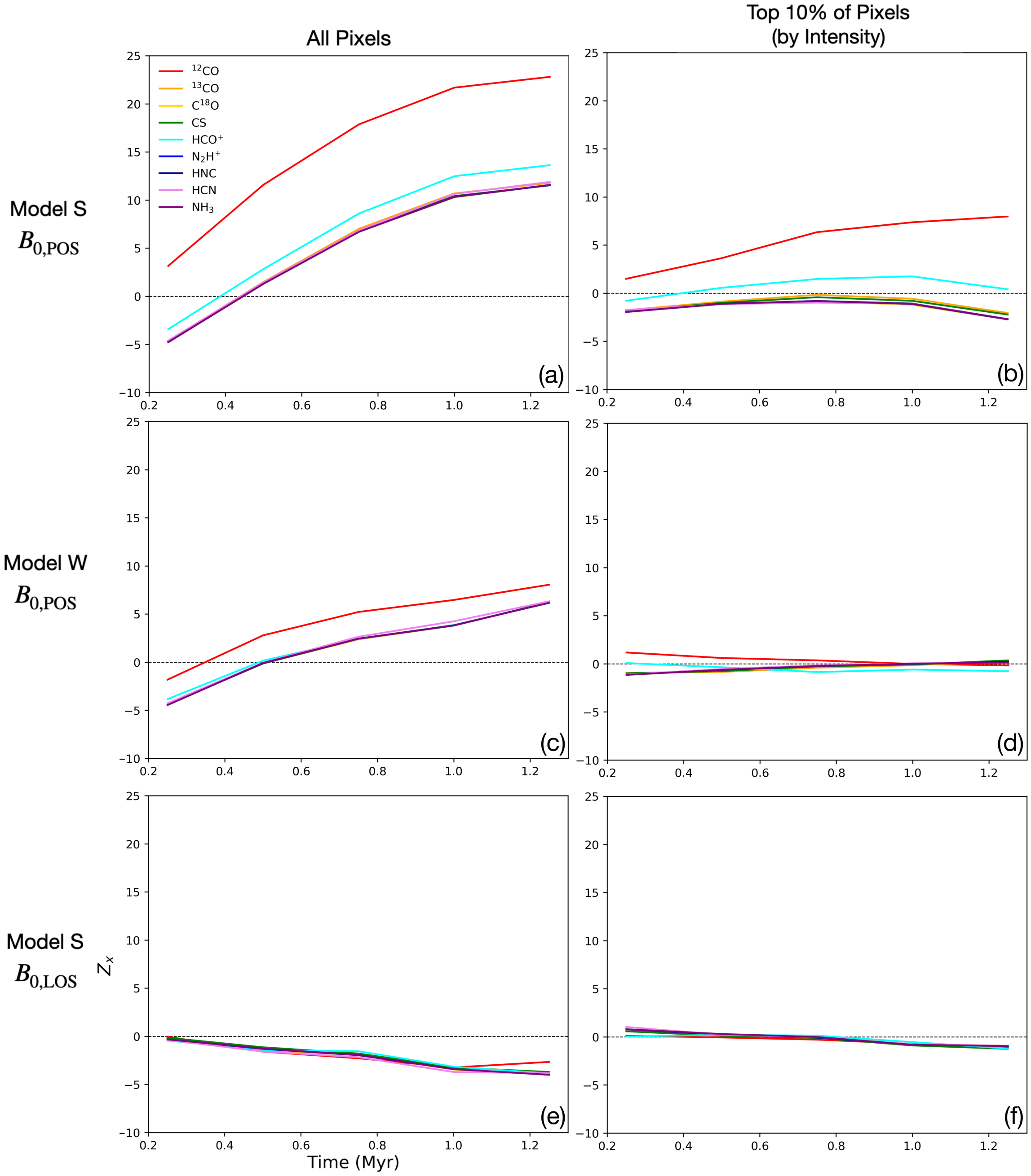

Figure 3.6: The Projected Rayleigh Statistic (Z_X) as a function of time for each of our tracers, for a variety of scenarios within our main grid of models. The left column shows the results using the whole observer space, and the right column incorporates a cut that includes only the top 10% highest intensity pixels in the computation. ***Panels (a) and (b):*** Fiducial model results (stronger magnetic field simulation, viewed with B_0 in the plane-of-the-sky). ***Panels (c) and (d):*** Same as fiducial model, but with the weaker field simulation (Model W). ***Panels (e) and (f):*** Same as fiducial model, but viewed with B_0 along the line-of-sight.

$\boldsymbol{B}$ decreases. The PRS stays above zero for all tracers even down to $i = 30°$, and the value for ^{12}CO remains notably larger than the values for the high density tracers. There is a different outcome when we only consider the top 10% of cells. ^{12}CO follows roughly the same trend, but the other tracers (with the exception of HCO^+) show moderately negative Z_x for $i = 90°$ and $i = 60°$. This is because with this 10% cut we only include the highest column density cells, which have a preference for perpendicular alignment. However, as the view becomes more inclined (and the plane-of-the-sky component of the magnetic field is thereby reduced), this preference is eliminated and Z_x moves toward zero. Interestingly, even at $i = 30°$ there is essentially no perpendicular alignment in any of the tracers, other than ^{12}CO.

3.7 Discussion

Our discussion is split into four parts. In Section 3.7.1 we use optical depth information to connect our results to the 3D picture of our simulations. We then comment on the possible physical implications of a given observation as implied by our simulations. In Sections 3.7.2 and 3.7.3, we examine the impact of varying the abundance (for a given molecular tracer) and radiative transfer assumption (LTE vs. LVG), respectively. Finally, in Section 3.7.4 we apply beam convolution to selected synthetic observations and investigate the corresponding HRO results, to provide a more direct comparison with Vela C data (Fissel et al., 2019).

3.7.1 Optical Depth Connection

To facilitate this analysis, we used RADMC3D to calculate the physical depth of the $\tau = 1$ surface for each of our observed molecular tracers (at line center). Results taken from the fiducal observing frame from Model S are shown in Figure 3.8. For many of the high density tracers (NH_3, HCN, HNC, N_2H^+, $C^{18}O$), almost the entire

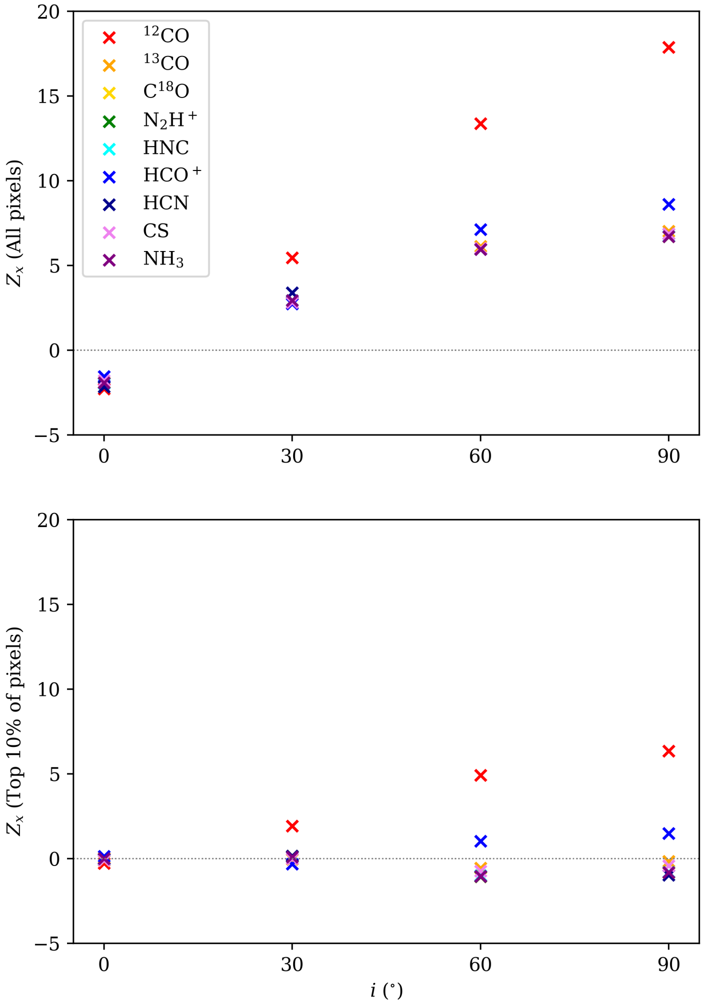

Figure 3.7: The Projected Rayleigh Statistic results for each of our tracers for a variety of magnetic field inclinations, using the fiducial $t = 0.75$ Myr time step of Model S. An inclination of $i = 90°$ corresponds to the $B_{0,\mathrm{POS}}$ view, and $i = 0°$ corresponds to the $B_{0,\mathrm{LOS}}$ view. The top and bottom panels show the results for all pixels in the observer space and only the top 10% of pixels, respectively.

cloud along the line-of-sight is optically thin; the $\tau = 1$ surface is not encountered between the observer and the far side of the cloud for 90% of sightlines, and for all the remaining 10% of sightlines the $\tau = 1$ is reached only beyond the midplane. For CS, ^{13}CO, and HCO^{+}, about 5% of sightlines (10% for HCO^{+}) encounter $\tau = 1$ just in front of the midplane. These regions are well correlated with the highest column density sight-lines.

^{12}CO is the most optically thick tracer by a wide margin. For about 40% of the observer space the $\tau = 1$ surface is encountered in ^{12}CO before the midplane. These high opacity sightlines overlap with some of the highest column density regions in the simulation (see Figure 3.9), thus obstructing the observer's view of high volume density regions. This provides physical evidence for why ^{12}CO produces a distinct alignment trend from the others. That is, the data from ^{12}CO are clearly probing a different section of the cloud, only receiving emission from the lower density foreground along the optically thick sight lines. The "high density" tracers also probe this low-density material, but since they are optically thin up to (and in some cases, through) the midplane of the cloud, the final intensity ultimately becomes dominated by the high density gas.

To demonstrate this effect, plotted in Figure 3.9 are histograms of the location along the line-of-sight of the $\tau = 1$ surface for tracers that are representative of these two regimes, ^{12}CO and CS. On a dual axis, we compare this to the maximum number density reached in a slice of the cloud (parallel to the plane-of-the-sky) at a given depth into the cloud along the line of sight. From this visualization, we can see that the peak of the distribution for CS is nearly aligned with the maximum volume density in the simulation box. The observed CS emission therefore serves as a good probe of the high density gas in the simulation, and it is able to trace the high density filaments visible in the column density maps (see e.g., Fig 3.4). As a

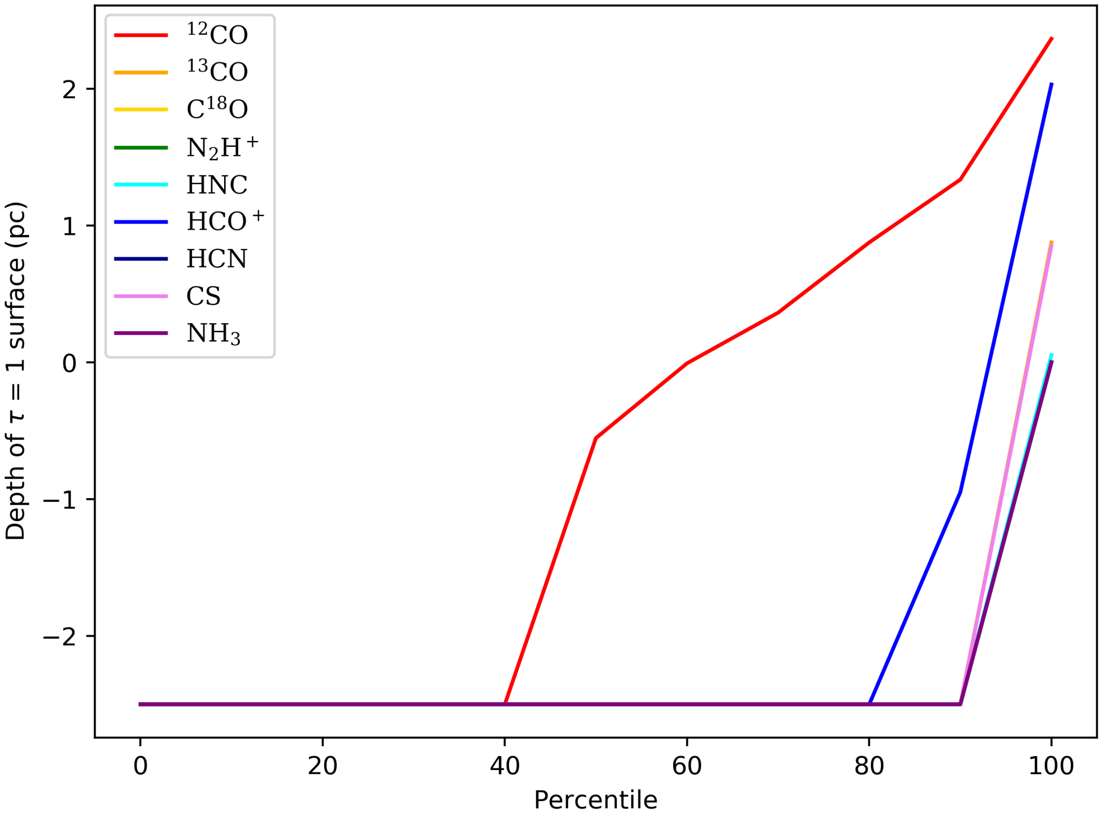

Figure 3.8: The depth of the $\tau = 1$ surface for each of our tracers, as calculated from the fiducial frame in Model S. Whereas for ^{12}CO $\sim$40% of pixels are fully optically thin (corresponding to the very lowest intensity pixels, in the outskirts of the cloud), all the other tracers are optically thin in $\gtrsim$90% of pixels (with the exception of HCO$^+$, at $\sim$80%). For ^{12}CO the $\tau = 1$ surface is encountered in front of the midplane in about 40% of pixels. Note: in this figure the line for C^{13}O is overlapped by the CS line, and the lines for N$_2$H$^+$, HNC, C^{18}O, and HCN are overlapped by the NH$_3$ line.

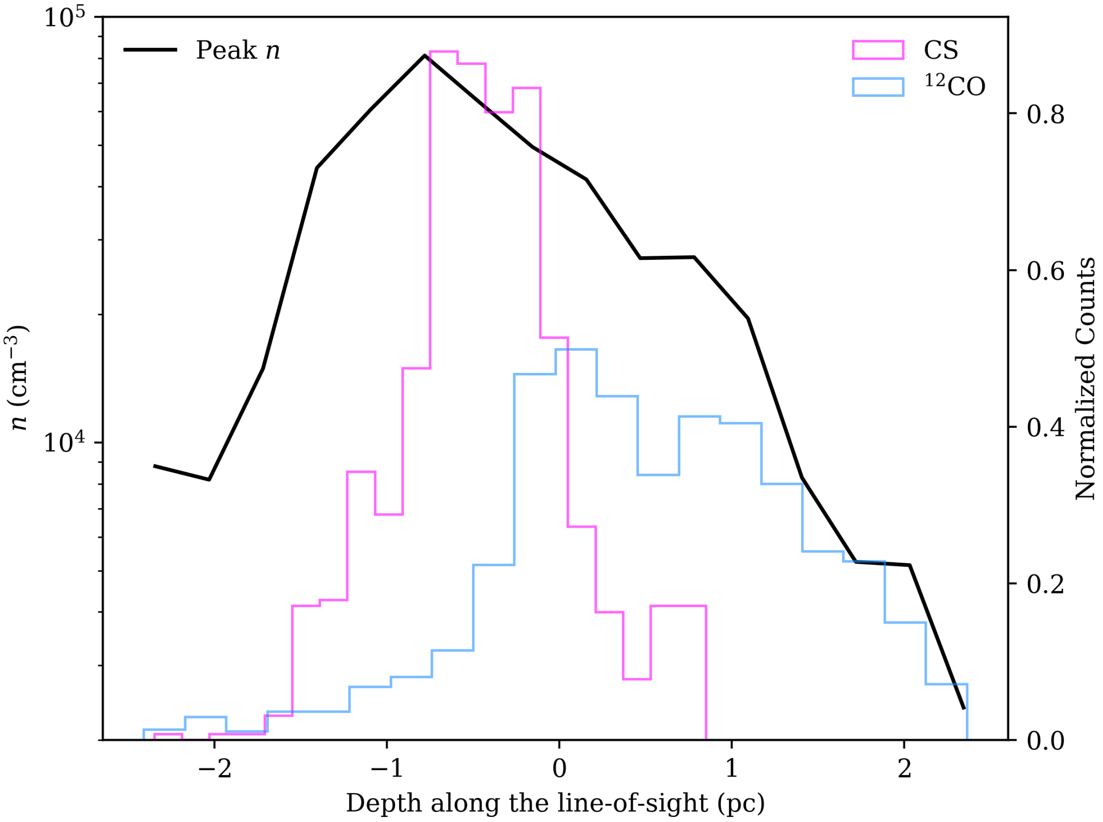

Figure 3.9: Comparison between the maximum volume density reached along the observer's line-of-sight and the histograms of the $\tau = 1$ surface depths for ^{12}CO and CS. The observer is placed at positive infinity on the axis. The CS distribution is well-aligned with the location of the highest volume density gas, consistent with the expectation that CS operates as a high-density tracer. Meanwhile, the ^{12}CO is offset toward the front of the cloud where n is lower, confirming that it largely probes the low density gas.

result, the perpendicular alignment between 3D gas structure and magnetic fields at the highest volume densities (see e.g., Figure 3.2 panel (a)) is preserved in the high intensity cut for CS (negative Z_x). Meanwhile, the ^{12}CO $\tau = 1$ surface distribution is offset from the peak volume density along the line-of-sight toward the closer side of the cloud to the observer. Therefore, the observed ^{12}CO emission only probes (on average) lower density gas. This material shows a preference for parallel alignment, which is reflected in the ^{12}CO HRO results.

Notably, the results found here are consistent with those obtained in a similar experiment by Hu et al. (2019b). They studied the effectiveness of velocity channel gradients (VChGs; see, e.g., Lazarian & Yuen, 2018) in probing the magnetic field orientation using molecular tracers ^{12}CO, ^{13}CO, C^{18}O, CS, HNC, HCO^{+}, and HCN. They found that ^{12}CO, and to lesser extent ^{13}CO, is much more effective at reconstructing the magnetic field in low-density regions than in high-density regions. In contrast, lower optical depth tracers (such as C^{18}O, CS, and HNC) were effective over a larger range of densities. This result lead to the suggestion that ^{12}CO can serve to study the field structure in the outer layers of the cloud, and the lower optical depth tracers to trace high-density structure. Our work here supports this idea, with Figure 3.12 especially showing that it is indeed the case that line radiative transfer observations of ^{12}CO trace different (outer layer) gas as compared to the tracers that probe more deeply into the high-density material in the cloud midplane.

3.7.2 CS and ^{12}CO Abundance Case Studies

The previous section discussed different gas-magnetic field alignment preferences in synthetic molecular line observations, and we attributed such difference to the different density ranges traced by these molecules. The synthetic observations, however, also depend on species abundances, which in our main grid of models we prescribed using observational constraints (see Table 3.1). We therefore performed a case study of varying species abundance to explore how it may affect synthetic line emissions.

Shown in Figure 3.10 are the PRS results for synthetic observations of ^{12}CO and CS with abundances ranging from 10^{-10} to 10^{-4}. Interestingly, the PRS values from a single molecular line with various abundances highly resemble those from various gas tracers (see panel (b) of Figure 3.6). Note that the ^{12}CO and CS show nearly identical results at very low abundance. This represents the optically thin observing scenario, and as such the particular radiative transfer properties of the tracer are irrelevant - the observer sees all of the emission, essentially reproducing the column density map simply calculated by summing up the volume density along the line-of-sight (Equation 3.6). However, when the abundance value is turned up, optical depth begins to come into play and high column density material becomes obscured. The transition abundance is different ($\sim 10^{-5}$ for ^{12}CO, and $\sim 10^{-7}$ for CS), but in both cases the Z_x value systemically increases after that threshold is reached.

This case study demonstrates that optical depth is the critical factor controlling the observed gas-magnetic field alignment preference. In other words, operative quantity that Z_x depends on is the density of cloud material being probed, which ultimately is principally a function of the depth into the cloud probed by the observation.

3.7.3 LTE vs. LVG

Our main results were computed using the LTE assumption, with $T = 10$ K set to match the isothermal conditions prescribed in our MHD simulations. In the top two panels of Figure 3.11, we compare these results to those obtained using another commonly-adopted radiative transfer mode, the Large Velocity Gradient (LVG) approximation, for a sub-selection of our tracers. The ^{12}CO emission becomes somewhat more patchy, compared to the fairly uniform LTE case. This is expected, since at

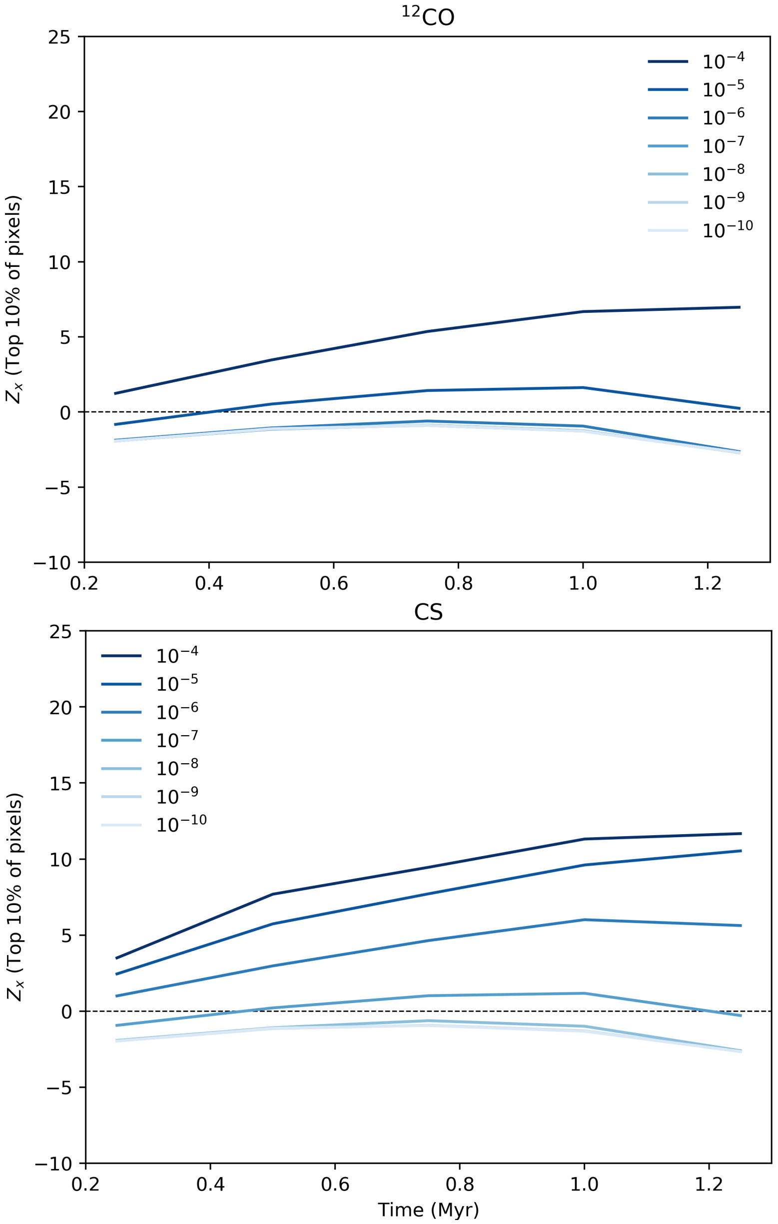

Figure 3.10: The Projected Rayleigh Statistic calculated using the top 10% highest intensity cells for ^{12}CO (top) and CS (bottom) at abundances ranging from 10^{-10} to 10^{-4}. At very low abundance both tracers exhibit perpendicular alignment. As the value is increased, they both move to positive Z_x, due to the corresponding increase in optical depth. In cloud environments CS and ^{12}CO are observed to have abundances of $\sim 10^{-8}$ and $\sim 10^{-4}$, respectively, so they are typically associated as high- and low-density tracers, respectively.

each point in the simulation space the LVG method uses a calculation of gas velocities near a given location to determine photon escape probabilities, which produces different results at different locations. Interestingly the patchiness in the ^{12}CO introduces some perpendicularly aligned structure, slightly lowering the PRS. Even so, the overall parallel-alignment character of the ^{12}CO remains.

The effect of changing from LTE to LVG differs among the high-density tracers. The CO isotopologues (^{13}CO and C^{18}O) both show very little change, both visually and in terms of the PRS values. However, the CS produces a significantly different result, with the LVG map becoming much more opaque and revealing less of the high density filamentary material. In turn, this leads to an increase in the PRS, with the densest sightlines (top 10%) flipping from overall perpendicular alignment to parallel alignment. The top row of Figure 3.12 shows the impact on the CS optical depth. The LVG calculation produces a $\tau = 1$ surface that is on-average closer to the front of the cloud, with respect to the observer. This agrees well with the analysis performed above in Section 3.7.1. Of note, the ^{12}CO $\tau = 1$ surface also moves closer to the observer when LVG is employed. This does not translate to an increase is Z_x, however, because even in LTE the ^{12}CO was already quite opaque.

We found that in LTE, the occupation of the upper and lower levels of the of the $J = 1 - 0$ transition for CS were 25% and 11%, respectively. In LVG this increased to 44% and 28%, which is comparable to the LTE values for the ^{12}CO $J = 1 - 0$ transition (43% and 25%). This higher occupation, particularly in the upper level, leads to more emission and, in the case of CS, an increase in the optical depth of the transition.

Here, we have briefly highlighted that the physical method for simulating the radiative transfer can have some impact on the results for a given molecular tracer, with the operative effect being that the redistribution of level populations can produce

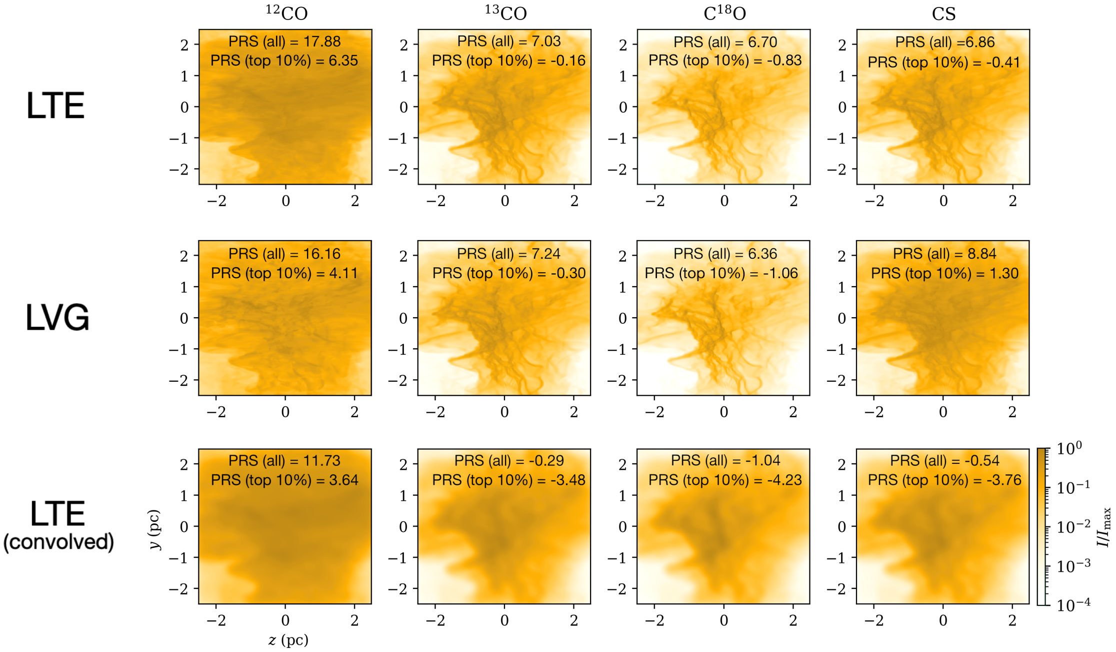

Figure 3.11: The effects of changing the radiative transfer mode (middle row: LVG) and beam size (bottom row: 0.2 pc FWHM Gaussian convolution) on (normalized) Moment 0 maps for a sub-set of the molecules we simulated. Note that the switch to LVG is not uniform across the tracers; it has obvious effects on the ^{12}CO and CS emission, but there is virtually no change for ^{13}CO and C^{18}O.

emission with higher optical depth if the occupation of the upper level of the transition is increased (or lower optical depth if the occupation of the upper level is decreased). The overall physical interpretation of the PRS and its relationship to opacity (i.e., that optical depth is a key driver of the Z_x value, as it dictates whether the high density filaments are visible) remains unchanged. Future work may include a more detailed exploration of the specific impact of radiative transfer mode on the HRO results for a wider variety of physical situations and tracers.

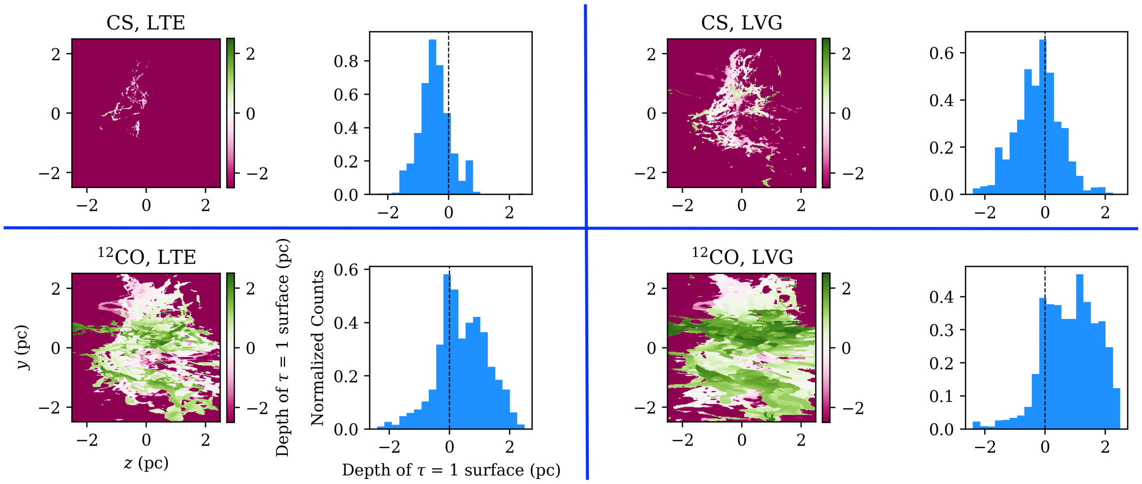

Figure 3.12: Comparison of the depth of the $\tau = 1$ surface in LTE vs. LVG, for ^{12}CO and CS. In both cases, switching the radiation transfer mode to LVG brings the $\tau = 1$ surface closer to the observer on average. This translates to a higher Z_x in the CS, as it transitions from optically thin to optically thick in some sub-regions.

3.7.4 Beam Convolved Results & Comparison with BLASTPol Vela C Observations

In Fissel et al. (2019), BLASTPol polarization results and Mopra molecular line observations were used to calculate the PRS for the Vela C molecular cloud. Though our MHD simulation setup was not specifically tailored to Vela C (rather, it is meant to be a generic collapsing cloud), it can still be useful as a point of comparison for the results in Fissel et al. (2019). To generally replicate observational conditions, we convolve our (LTE) line radiative transfer intensity maps and polarization maps with a variety of Gaussian beam sizes ranging from 0.2 to 0.6 pc (FWHM), then recompute the HRO and PRS.

These data are presented in Figure 3.13, alongside a comparison to the PRS results obtained from Vela C. (adapted from Fissel et al. (2019)). In addition to the 10%-intensity cut used for the main set of models, we also present results with softer cuts of 30%, and 50% of sightlines (see Table 3.3 for cutoff values). This is designed to resemble the sensitivity limitations in real observations. These results show that beam convolution does have some impact on the outcome of the HRO calculations. Particularly, it tends to reduce $|Z_x|$ across all tracers, especially for the hardest (10%) and softest (50%) cuts. In the 50% case, it is possible that this effect is partially enhanced by the fact that the beam convolution tends to emphasize the edge of the cloud (this can be seen visually in the bottom row of Figure 3.11).

Our results for the multiple intensity cuts provide a potential explanation for the wide range of Z_x computed for the different tracers in Vela C. Higher abundance molecular like ^{12}CO and ^{13}CO tend to be observable across the whole cloud, whereas the lower abundance ("high-density") molecules require greater sensitivity, and can only reach the sensitivity threshold in the highest column density regions of the observer space. Accordingly, the Z_x computed for softer cut (50%) is in reasonably good agreement with the Vela C results for ^{12}CO and ^{13}CO, and the high-density tracers agree better when the calculation is restricted to only the top 10% of pixels. It is worth emphasizing again, however, that our simulation is not tailored to mimic Vela C, and some of the discrepancy between the observational and synthetic results may also be due intrinsic physical differences between the physical set-up of our model and the underlying physical conditions in Vela C. More broadly, this experiment demonstrates that the sensitivity of an observation can have an important effect on the observed HRO results. The very brightest pixels correspond to the highest column density, where structures preferentially align perpendicular to the magnetic field. Therefore, lower sensitivity observations will tend to bias the results toward negative Z_x, because the lower column density regions are excluded.

One additional important caveat for this analysis is that all of the radiative transfer simulations performed in this work assumed uniform relative abundance. A variable

Table 3.3: The values corresponding to the 50th, 70th, and 90th percentile intensity cuts for each molecular tracer simulated in this work, as taken from the fiducial frame in Model S.

Species	50th (K km/s)	70th (K km/s)	90th (K km/s)
^{12}CO	12.84	18.91	28.64
^{13}CO	2.29	5.22	13.17
C^{18}O	0.70	1.70	4.66
N_2H^+	0.26	0.63	1.70
HNC	0.41	0.96	2.59
HCO^+	6.18	12.54	25.09
HCN	0.33	0.78	2.11
CS	1.89	4.40	11.40
NH_3	0.41	1.04	2.81

prescription, particularly one that assumes higher relative abundance at higher volume density, would likely produce results that further emphasize the perpendicular character of the high-density tracers. Likewise, in the very lowest density regions of our simulation box (including the ambient gas outside the main cloud) there is no taper in the abundance. This is probably unrealistic, as molecular gas does not form as readily in the lower density ISM. Therefore, our results that only use 50% of the pixels may be generally more useful for observational comparison than the results using all the pixels.

3.8 Conclusions

In this work, we performed synthetic dust polarization and molecular line observations of 3-dimensional MHD data to investigate the relationship between the magnetic field and gas density structure in a collapsing molecular cloud using the HRO technique. We observed our cloud at multiple stages of evolution over ∼1 Myr,

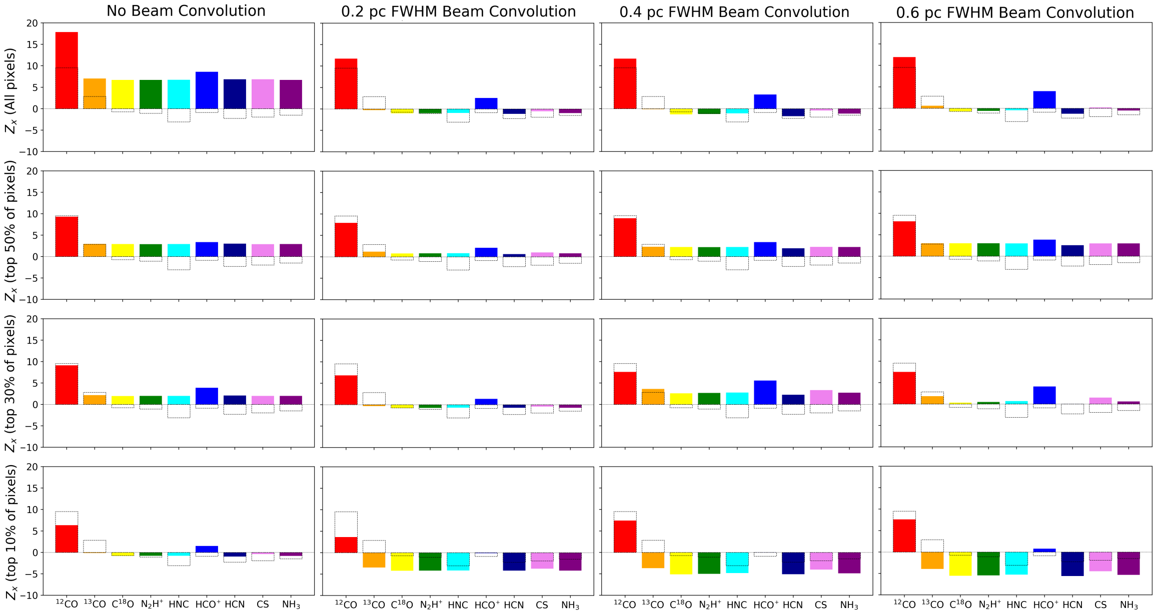

Figure 3.13: PRS results from the fiducial frame for Model S, for a matrix of Gaussian beam sizes and sensitivity cuts. For comparison, the PRS values for the Vela C molecular cloud computed by Fissel et al. (2019) are included in each plot (as dashed bars). Generally, the Vela C results for ^{12}CO and ^{13}CO are best reproduced by our lower sensitivity models (top 50% or all pixels), and the results for the remaining tracers (all of which have negative PRS values in Vela C) are best reproduced by our lower sensitivity models (top 30% or top 10% of pixels). Beam convolution tends to decrease the value of the Z_x, especially in the highest intensity pixels.

and from a variety of viewing geometries. Additionally, we tested how the results were affected by changing the global magnetic field strength, the abundance of our selected species, and the chosen radiative transfer mode (LTE vs. LVG). To link our theoretical exploration to the current observational state of the field, we also compared selected results with the analysis of Vela C performed by Fissel et al. (2019). Our main conclusions are as follows:

1. Analysis of our magnetized turbulent cloud simulations shows that the relative orientation between the 3D magnetic field and density structures depends on the cloud-scale magnetic field strength (see Figure 3.2). The super-Alfvénic simulation (Model W) showed significantly more magnetic field tangling, and as a result had relatively little alignment preference compared to the trans-Alfvénic simulation (Model S), especially at high densities. In Model S the mean magnetic field remained relatively rigid, leading to the formation of orthogonal elongated filaments. In the lower density regions, thin streams of gas formed along the the field lines (Figure 3.3). These structures are visible in slice plots of our simulations, and are similar to the striations seen in observations. In Model S, the transition from parallel alignment to perpendicular alignment occurs at $n \gtrsim 4 \times 10^3$ cm^{-3} for the $t = 0.75$ Myr timestep. Notably, this is in close agreement with the transition value of ~1000 cm^{-3} estimated for Vela C (Fissel et al., 2019).

2. The intrinsic relative gas-magnetic field orientations observed in 3D are also visible in the HRO analysis using our synthetic molecular line observations (Figure 3.5). Excluding the very earliest times, the PRS results with no intensity cut ("all pixels") generally show (for both Model S and Model W) parallel alignment when the mean magnetic field is in the plane-of-the-sky. This is

because the overall observer-space is dominated by low density sightlines. The situation changes when we consider only the highest intensity (top 10%) pixels. For Model W, each of the tracers show a PRS value close to zero in this cut. Meanwhile, for Model S there is some stratification; most show a $Z_x \lesssim 0$ across all times, however ^{12}CO has a positive value.

3. In the $B_{\rm POS}$ view (i.e., the viewing orientation with the mean magnetic field in the plane-of-the-sky), the difference in HRO result between ^{12}CO and the high density tracers is closely linked to optical depth effects. The $\tau = 1$ surface for ^{12}CO is on average closer to the front of the cloud (from the observer's point of view) than the $\tau = 1$ surface for CS (Figure 3.12). This results in the ^{12}CO emission mainly probing the low-density gas where alignment preference is dominated by the magnetic field-aligned striations, instead of the denser filaments which align orthogontal to the mean magnetic field. This is the case even in the highest intensity pixels. Though this discussion is primarily framed as a distinction between molecular lines, it is also the case that if we drastically vary the abundance for a given tracer, both positive Z_x and negative Z_x results can be produced (Figure 3.10). This demonstrates that for a given observation it is the optical depth itself that is the essential quantity in determining which regions of the cloud are probed.

4. When the mean magnetic field is inclined away from the plane-of-the-sky (we define the $B_{\rm POS}$ view to have $i = 90°$ in this work), the absolute value of Z_x tends to decrease (Figure 3.7). At intermediate inclinations of $i = 60°$ and $i = 30°$, there is still moderate differentiation between the PRS for ^{12}CO and the high-density tracers, but this vanishes when $i \rightarrow 0°$. This produces some degeneracy between the results for a weak magnetic field (Model W) and a

strong magnetic field oriented along (or nearly along) the line-of-sight.

5. Our main set of results used synthetic line radiative transfer observations that were generated assuming LTE at $T = 10$ K. For a subset of our tracers (^{12}CO, ^{13}CO, C^{18}O, and CS), we also computed results using the the (non-LTE) LVG method (Figure 3.11). For ^{13}CO and C^{18}O, the Moment 0 maps (and HRO outcomes) were unaffected. However, for ^{12}CO and CS there was some change. Particularly, the optical depth of the CS map increased, resulting in an increase in the PRS value (including a transition from negative to positive Z_x in the top 10% of pixels). Meanwhile, the ^{12}CO emission (which was already optically thick in LTE) became somewhat less uniform. These results, though slightly different from the LTE case, are generally consistent with our main conclusion that the value of Z_x is strongly linked to the optical depth of the observation. Future work is required for a more detailed assessment of how taking into account non-LTE effects generally affects the results for each tracer.

6. The introduction of a Gaussian beam convolution (Figure 3.13) to our synthetic maps tended to decrease the value of Z_x, though this effect is somewhat counterbalanced for larger (0.4 pc, 0.6 pc FWHM) beams due to washing out of some high density structures perpendicular to the mean magnetic field. Also of note, the sensitivity of an observation (as studied by testing intensity-based cuts at the top 50%, 30%, and 10% of pixels) can have an important effect on the value of Z_x. The effects of beam convolution and sensitivity limit need to be taken into account when using numerical simulations to interpret observations, such as those from Fissel et al. (2019) for Vela C.

CHAPTER 4

THE ZEEMAN EFFECT IN PROTOSTELLAR ENVELOPES

This chapter is adapted from Mazzei et al. 2024, Monthly Notices of the Royal Astronomical Society, 527, 8618, with minimal modification.

4.1 INTRODUCTION

Magnetic fields are pervasive across many scales in star formation environments and are expected to play an important role in regulating gas flows and structure formation at a variety of stages of the star formation process. On the molecular cloud scale ($\gtrsim$1 pc), magnetic fields both restrict gas flows and provide opposition to gravitational collapse (Mestel & Spitzer, 1956; Mouschovias & Spitzer, 1976). Cloud-scale fields are well studied with far-infrared/sub-mm polarimetry experiments such as Planck, BLASTPol, and SOFIA (Planck Collaboration Int. XIX, 2015; Galitzki et al., 2014; Fissel et al., 2016; Chuss et al., 2019). These experiments leverage the well-established “radiative torques" (RAT) grain alignment theory, wherein spinning, effectively oblate dust grains preferentially align with their short axes parallel to the local magnetic field direction (Lazarian & Hoang, 2007), yielding linear polarization that is perpendicular to the magnetic field (Davis & Greenstein, 1951).

While dust grain alignment with the magnetic field is understood to be the dominant source of linearly polarized far-IR emission at larger scales, at smaller scales (∼100s-1000 au), however, the interpretation of linear polarization as a magnetic field tracer is more tenuous because other sources of polarization become important. In disks particularly, self-scattering of thermal dust emission (Kataoka et al., 2015; Yang et al., 2016), gas flow alignment (Kataoka et al., 2019), and "k-RAT" radiation field alignment (Kataoka et al., 2017; Tazaki et al., 2017) may all produce linear polarization signatures. Nonetheless, observing magnetic fields on these smaller scales remains of great interest. In older sources (Class II), magnetic fields are predicted to launch jets and winds along the disk axis (Blandford & Payne, 1982), generate magneto-rotational instability (MRI; Balbus & Hawley, 1991), and produce flows that contribute to the formation of rings and gaps (Suriano et al., 2017) or planetesimals (via zonal flows; Johansen et al., 2009). In younger (Class 0/I) protostars, magnetic fields may also hinder disk growth on 100+ au scales through magnetic braking, especially when the magnetic field aligns with the rotation axis of the surrounding envelope (Mellon & Li, 2008; Hennebelle & Fromang, 2008).

Another method for accessing magnetic fields in small-scale sources is to observe molecular line transitions in species that are sensitive to the Zeeman Effect (e.g., CN, OH, HI). In the presence of a magnetic field, the energy levels of these lines are split into higher and lower energy circularly polarized components, and the degree of splitting is proportional to the line-of-sight magnetic field strength (Crutcher et al., 1993). Historically, Zeeman observations have mainly been performed using single-dished telescopes to probe core-scale (∼0.1 pc) line-of-sight magnetic field strengths (see, e.g., Heiles & Troland, 2004; Falgarone et al., 2008; Troland & Crutcher, 2008;

Crutcher et al., 2010). However, in recent years with the advent of a circular polarization observing mode on the Atacama Large Millimeter/submillimeter Array (ALMA), higher resolution ($\lesssim 1''$) Zeeman observations are now possible. Disk-scale observations have proven challenging, with programs to-date yielding upper limit constraints only (Vlemmings et al., 2019; Harrison et al., 2021). Though disk-scale magnetic field strengths of up to ∼3 mG or more are predicted, the line-of-sight strength is likely suppressed in many disks due to cancellation within the torodial $\boldsymbol{B}$-field component (Mazzei et al., 2020; Lankhaar & Teague, 2023).

Given the complicated situation inside disks, an alternative approach for searching for magnetic field signatures in protostellar environments is to probe the inner envelope regions beyond the edge of the disk. The advantages of the envelope are two-fold. First, the inner envelope-scale magnetic field is expected to be almost as strong as in a disk, while still remaining relatively unaffected by disk-scale tangling and toroidal wind-up. Linear dust polarization studies of these environments have revealed polarization percentages up to ∼5%, with relatively uniform geometry in some cases (Cox et al., 2018). Second, some envelope sources have been observed to have bright emission of Zeeman-sensitive molecules such as CN (see, e.g., Tychoniec et al., 2021).

In this work, we conduct 3D radiative transfer simulations to produce simulated emission maps of circularly polarized emission of the CN $J = 1 - 0$ transition for two different simulated protostellar envelope sources. Our first test case is a protostellar disk around a low-mass protostar, and the second the envelope around a massive protostar. For each simulation, we calculate the Stokes I and Stokes V obtained from many beams across the envelopes of our sources. We report the percentage polarization (V/I) and compare the implied line-of-sight magnetic field strength (B_{LOS}) from the Zeeman fitting with the actual mean (density-weighted) B_{LOS}. There is substantial variability in the results for different beams due to non-uniform local magnetic field structure, but in some cases we find percentage polarization values $\gtrsim$2%.

Given the nominal ALMA sensitivity limit of 1.8%, this suggests that Zeeman experiments with current instruments can be a useful way to study magnetic fields in (proto)stellar envelopes. However, program success depends critically on source selection and beam placement. It should be noted that our comparisons in this work are based strictly on radiative transfer simulations; we do not use the ALMA simulator to produce simulated observable products. Direct observational comparison of simulations to ALMA program data should involve use of the CASA simulator (McMullin et al., 2007). This is outside the scope of our work here. Nonetheless, from our results we are able to identify some general criteria for setting up observations to maximize detectability. Particularly, we find that regions some distance away from the central star at intermediate line-center optical depth ($\tau_{LC} \sim 0.1 - 1$) tend to be favorable. Furthermore, our results suggest that continued improvement of circular polarization instruments will be extremely fruitful; we predict that a factor of ten improvement in sensitivity (i.e., to a 0.18% limit) will make sightlines across nearly the entire inner envelope detectable for sources with typical magnetic field strengths (i.e., $\gtrsim$ 1 mG, comparable to those found in our simulations).

This paper is organized as follows. In Section 4.2 we introduce the two model types we consider in this work, then in Section 4.3 we discuss our methods for making our simulated Zeeman emission maps. Section 4.4 presents the results of our simulations, including maps of the observables (Sec. 4.4.1), computations of percentage polarization values through the envelopes of our sources (Sec. 4.4.2), and comparisons of our pixel-by-pixel percentage polarizations to other associated observables as well as the underlying magnetic field information from our MHD simulations (Sec. 4.4.3). We then provide some discussion in Section 4.5 on some additional criteria that can affect whether a given sightline or location is favorable for Zeeman experiments, including some auxiliary observational factors of which observers should also be aware (Sec. 4.5.4). Finally, the main conclusions of this work are summarized in Section 4.6.

4.2 Numerical Simulations

Both sets of simulations studied in this work were performed using 3D grid-based MHD codes.

4.2.1 Low-Mass Protostellar Disk Envelope Simulation

Our first model type is an envelope and disk system around a low-mass protostar (henceforth known as `lmde`). The turbulent, non-ideal MHD model we used was the reference model of Tu et al. (2023). Here we highlight a few salient features of the model and refer the reader to Tu et al. (2023) for details. We use the `ATHENA++` code (Stone et al., 2008, 2020), and include adaptive mesh refinement (AMR) and full multigrid (FMG) self-gravity (Tomida & Stone, 2023).

The physical setup is similar to that used in Lam et al. (2019). We initialize a pseudo-Bonner-Ebert sphere prescribed by

$$\rho(r) = \frac{\rho_0}{1 + (r/r_c)^2} \,. \tag{4.1}$$

We set the central density $\rho_0 = 4.6 \times 10^{-17}$ g cm^{-3}, and characteristic radius $r_c = 670$ au. The sphere is embedded in a diffuse low-density gas ($\rho_{\rm amb} = 4.56 \times 10^{-20}$ g cm^{-3}). The total box size of the simulation domain is 10,000 au per side length, and the total gas mass is 0.56 $M_\odot$. The simulation is initialized with k^{-2} power spectrum turbulence (Kolmogorov, 1941; Gong & Ostriker, 2011) with an rms Mach number of unity, solid body rotation rate $\boldsymbol{\omega} = (\omega_x, \omega_y, \omega_z) = (0, 0, 6.16 \times 10^{-13}\ \mathrm{s}^{-1})$, and uniform magnetic field $\boldsymbol{B} = (B_x, B_y, B_z) = (0, 0, 2.2 \times 10^{-4}\ \mathrm{G})$. The rotation rate corresponds to a ratio of rotational to gravitational energies of 0.03, which is in the range of the values inferred observationally by Goodman et al. (1993) and Caselli et al. (2002) through velocity gradients across dense cores. However, what fraction of the measured gradient is contributed by rotation remains uncertain. The adopted field strength corresponds to a dimensionless mass-to-flux ratio of 2.6, close to the median value for dense cores inferred by Troland & Crutcher (2008) through OH Zeeman measurements after geometric corrections. We note that although the magnetic field is initially uniform, it is significantly distorted by the imposed turbulence, gravitational collapse, and rotation at later times, particularly in the inner envelope surrounding the disk [see, e.g., Fig. 4a of Tu et al. (2023)].

Ambipolar diffusivity η_A is prescribed as

$$\eta_A = \eta_0 \frac{B^2}{4\pi\rho^{3/2}} \,. \tag{4.2}$$

Based on cosmic ionization rate calculations from Shu (1991), we set $\eta_0 = 95.2\ \mathrm{g}^{1/2}\ \mathrm{cm}^{-3/2}$, corresponding to a standard reference value.

We perform our polarization analysis on a simulation frame at $t = 3 \times 10^4$ yr. By this time in the simulation, a stable disk has formed. The disk remains stable for a while after this as well, but slowly decreases in mass at later times (Tu et al., 2023). Our chosen frame corresponds roughly to the time of maximum disk mass. Column density plots of the `lmde` model for each the $x-$, $y-$, and $z-$lines-of-sight are shown in Figure 4.1, along with 2-dimensional histograms of magnetic field strength versus gas density and distance from the (central) sink particle[1].

---

[1] We note that the field strength in the inner protostellar envelope depends in a complex way on several factors, including the initial core mass and field strength, level of turbulence, and magnetic diffusivities. For example, Mignon-Risse et al. (2021) simulated magnetized disk formation in more

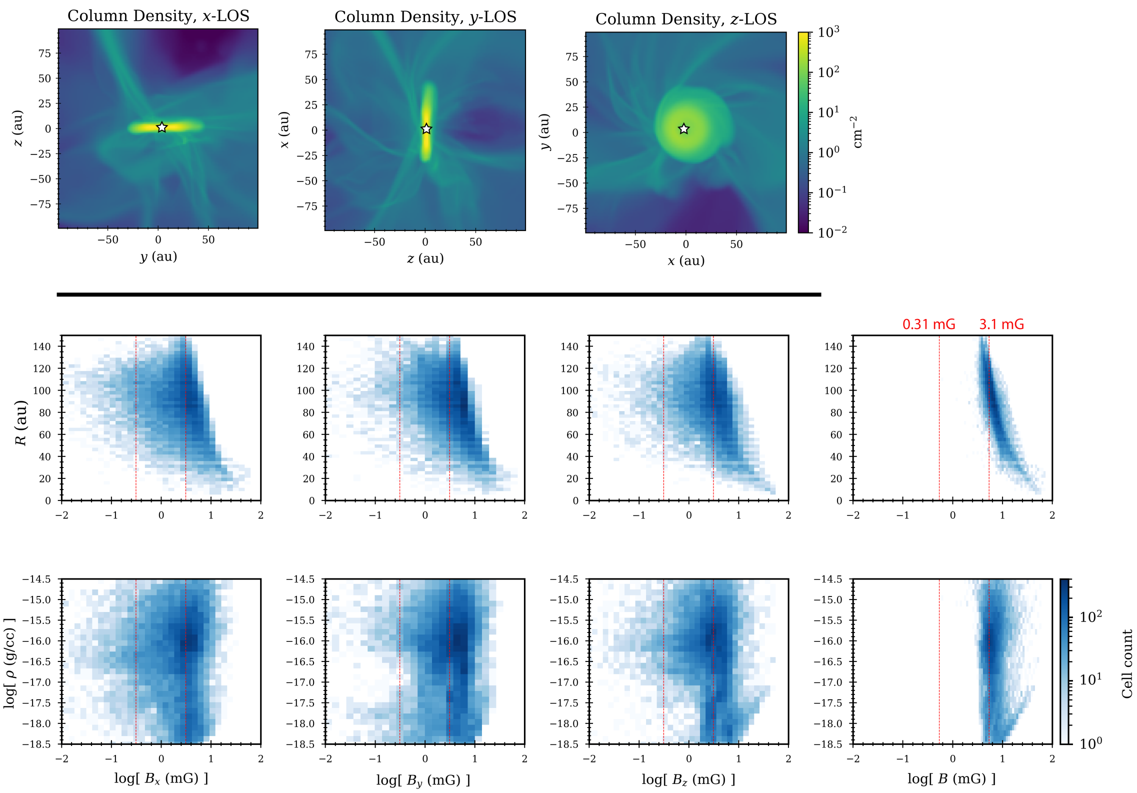

Figure 4.1: ***Top row:*** Column density plots for each of the Cartesian axis views of our `lmde` model. ***Middle row:*** 2-dimensional histogram plots of local magnetic field component strengths (in the final column, $B = \sqrt{B_x^2 + B_y^2 + B_z^2}$) versus distance from the central sink particle. Annotated in red are lines corresponding to 3.1 mG and 0.31 mG line-of-sight magnetic field strength (Section 4.3 discusses why these values are highlighted). ***Bottom row:*** 2-dimensional histogram plots of local magnetic field component strengths versus local density.

In Figure 4.2, we provide a 3-dimensional view of the magnetic field lines in the envelope. Whereas the magnetic field inside the disk is dominated by the toroidal component because of rotational wrapping [not shown here, but see discussion in Tu et al. (2023)], there are regions in the envelope where the field lines are more uniform and well-behaved.

---

massive cores with turbulence. They found milli-Gauss (mG) magnetic fields up to 1000 au, with the field strength reaching 100 mG or more on the inner ∼100 au scale (see their Fig. 13). Their magnetic field is stronger than ours, making it more detectable in principle. We postpone a detailed exploration of parameter space to a future investigation.

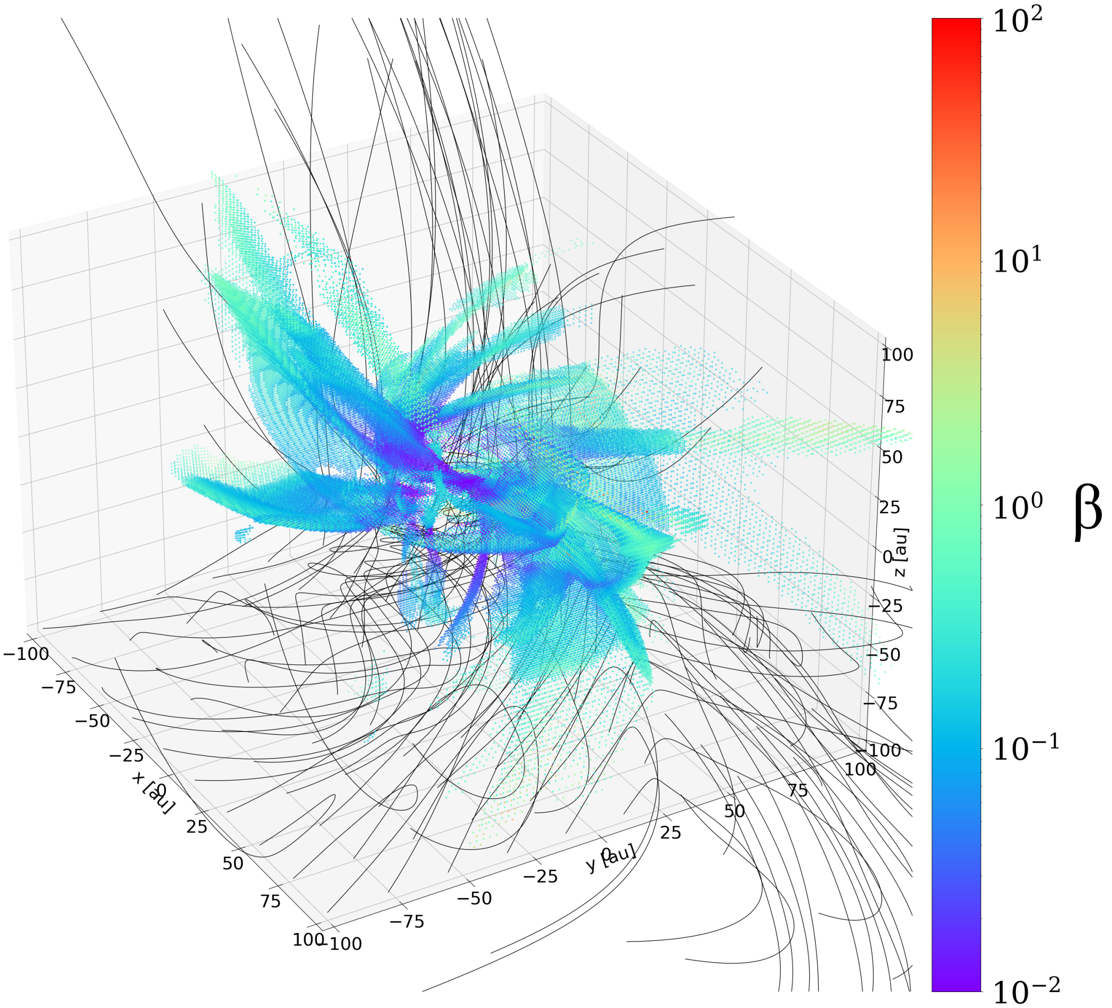

Figure 4.2: 3-dimensional view of magnetic field lines in the inner protostellar envelope region of our `lmde` model. Also included are 3D contours of the dimensionless plasma-β to highlight the flattened dense demagnetized structures that dominate the dynamics of the inner envelope [see Tu et al. (2023) for detailed discussion].

4.2.2 Massive Star-forming Envelope (MSEnv) Simulation

The massive star formation simulation (henceforth referred to as model `MSEnv`) considered here was conducted using the Radiation-Magnetohydrodynamic (RMHD) code ORION2 (Li et al., 2021) with 5 levels of AMR (highest resolution $\Delta x \approx 18\,\mathrm{au}$). The setup is similar to those described in Cunningham et al. (2011) but now with magnetic fields. The simulation was initialized as a massive cloud core of mass $M_{\mathrm{core}} = 10^3\,\mathrm{M}_\odot$ with a power-law density profile $\rho(r) \propto r^{-3/2}$ up to the radius of the core $R_{\mathrm{core}} = 0.18\,\mathrm{pc}$, which gives an average column density of $2.0\,\mathrm{g\,cm^{-2}}$. We then add a turbulent velocity field to the core with rms Mach number $\mathcal{M} = 2.43$, which corresponds to a virial parameter $\alpha_{\mathrm{vir}} = 1.67$ for the cloud core. This value was chosen for the balance between gravity and turbulent motions during the protostellar system evolution; see McKee & Tan (2003) for more detailed discussions. The initial magnetic field strength of the core is chosen so that the dimensionless mass-to-flux ratio is 3.0 inside the core, slightly larger than those observed in high-mass star-forming clumps ($\sim$1.5 − 2; see e.g., Crutcher, 2012; Pillai et al., 2016; Motte et al., 2018) to ensure gravitational collapse. The initial gas temperature inside the core is $T_{\mathrm{gas}} = 35\,\mathrm{K}$, which is also set to be the temperature floor of the simulation box to avoid numerical rarefaction. A frequency-integrated flux limited diffusion (FLD) algorithm is adopted to approximate the radiation transport (see Cunningham et al. 2011 for more details).

In ORION2, the formation and evolution of protostars are handled by the star particle model described in Offner et al. (2009), which includes launching protostellar outflows. A tracer particle routine is implemented to record the properties of the ejected gas (Offner et al., 2009; Cunningham et al., 2011), and we utilized this function to trace the effective region of protostellar outflows in our simulated emission maps (see Sec. 4.3).

We investigate the frame when the central star is about $29.8\,\mathrm{M}_\odot$ in mass, focusing on a $L_{\mathrm{box}} = 10^4\,$au region around the massive protostar. For easier computation we reproject the AMR data to 256^3 unigrid array in `python` using `yt` (Turk et al., 2011). In Figure 4.3 we present column density plots and 2-dimensional histograms of magnetic field and density data for model `MSEnv`.

4.3 SIMULATED ZEEMAN EMISSION MAPS

To characterize the observable magnetic field strength in each of the physical environments discussed above in Section 4.2, we produce simulated circular polarization emission maps of the CN $J = 1 - 0$ molecular line at 113 GHz. This line comprises a suite of nine hyperfine components[2] that are non-blended and stackable (Mazzei et al., 2020). For the majority of this work we choose to only simulate one representative sub-transition, the 113.144 GHz component with relative intensity RI = 8 and Zeeman factor $z_B = 2.18$. In Section 4.5.4 we consider the potential signal boost that can be gained from stacking.

We perform Zeeman-splitting line emission calculations using the POLARIS raditaive transfer code with the ZRAD extension (Brauer et al., 2017b), which incorporates data from the Leiden Atomic and Molecular DAtabase (LAMDA; Schöier et al., 2005) and the JPL spectral line catalog (Pickett et al., 1998). A Faddeeva function solver[3] is used to compute the final line shape, and included in the calculations are considerations for natural, collisional, and Doppler broading, as well as the magneto-optic effect (Larsson et al., 2014).

---

[2] See Falgarone et al. (2008) for a full list of these components, including their rest frequencies, relative intensities, and Zeeman factor values.

[3] `http://ab-initio.mit.edu/wiki/index.php/Faddeeva_Package`, Copyright ©2012 Massachusetts Institute of Technology

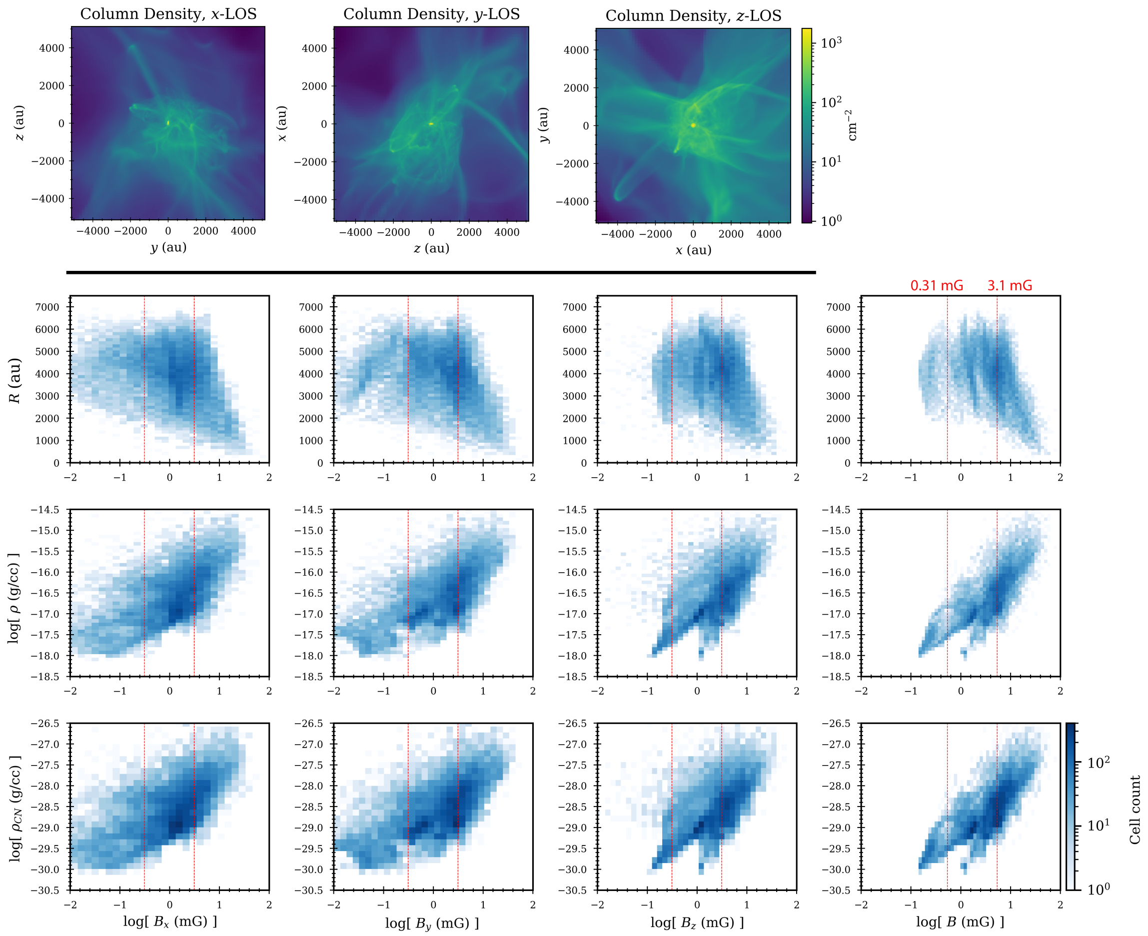

Figure 4.3: ***Top row:*** Column density plots for each of the Cartesian axis views of our `MSEnv` model. ***2nd row:*** 2-dimensional histogram plots of local magnetic field component strengths (in the final column, $B = \sqrt{B_x^2 + B_y^2 + B_z^2}$) versus distance from the central sink particle. Annotated in red are lines corresponding to 3.1 mG and 0.31 mG line-of-sight magnetic field strength (Section 4.3 discusses why these values are highlighted). ***3rd row:*** 2-dimensional histogram plots of local magnetic field component strengths versus local density. ***Bottom row:*** 2-dimensional histogram plots of local magnetic field component versus density, only including cells that are given a factor of 1000 enhancement in CN abundance in our model (from $X_{\mathrm{amb}} = 10^{-12}$ to $X_{\mathrm{shell}} = 10^{-9}$).

Our POLARIS line radiative transfer calculations are computed on 128^3 and 256^3 fixed resolution grids for models `lmde` and `MSEnv`. These translate to resolutions of 1.56 au and 39.1 au, respectively. For each cell, local gas density, gas velocity components, and magnetic field components are supplied from our MHD simulations. We also must specify a CN abundance value for each cell. For our `lmde` model we choose constant CN abundance $X_{\rm CN} = 10^{-9}$. This value ensures a moderately optically thin envelope beyond the disk edge at $R \sim$30 au, and is similar to estimates for CN abundances in disk modeling (Cazzoletti et al., 2018). In the massive star (`MSEnv`) model, we also set $X_{\rm CN} = 10^{-9}$, but only within a "shell" region that has cells containing tracer particles with values in a given range. This is meant to simulate a CN enhancement at the edge of a cavity blown out by a protostellar wind that is more directly exposed to the UV radiation from the central massive protostar system. Such regions are observed in some cases to be enhanced due to far-ultraviolet dissociation chemistry (Arulanantham et al., 2020). We set the range of tracer particle that define the shell by hand, choosing values that empirically produce a reasonable result. Slice and projection plots of our shell are shown in Figure 4.4. For the remainder of the massive star envelope (i.e., all cells not within the shell), we set a lower ambient CN abundance $X_{\rm CN,amb} = 10^{-12}$.

Each line emission simulation converts the position-position-position (PPP) data cube into a position-position-velocity (PPV) data cube. Values for the Stokes I, Stokes V, and optical depth τ are recorded in each pixel for 169 velocity channels in velocity range $[-3\ \rm{km/s}, 3\ \rm{km/s}]$ with respect to the rest frame of source. For all of our simulated emission, we assume local thermodynamic equilibrium (LTE) and set $T = 10$ K. A total number of 10^5 unpolarized background photons are initialized in each run, which are ray-traced to a 256^2 detector. For simulations of our `lmde` model, we place the detector at a distance $d = 150$ pc from the box center, and for

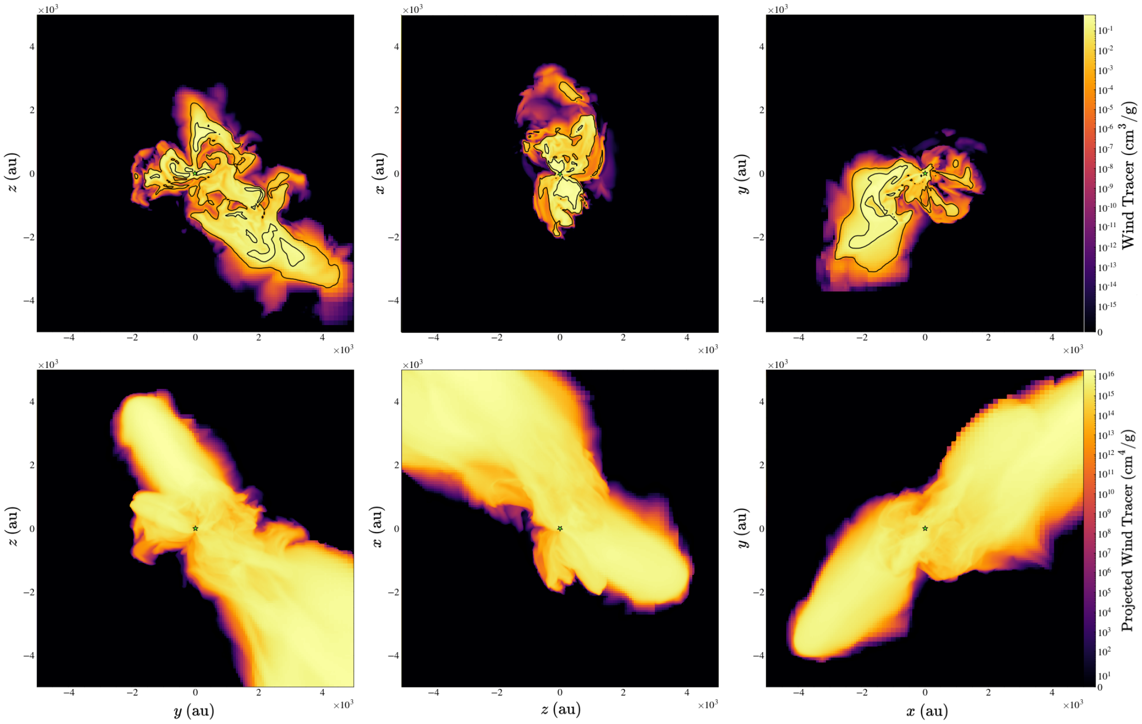

Figure 4.4: ***Top row:*** Midplane slice plots of the wind tracer value for the `MSEnv` model, as viewed from the $z-$, $y-$, and $x-$ lines-of-sight (left-to-right). Black contours are placed at wind tracer values of 0.001 and 0.2 cm^3 g^{-1}, the limits that define our CN enhanced shell. ***Bottom row:*** Projection plots of the line-of-sight integrated wind tracer value.

simulations of our `MSEnv` model we use $d = 1$ kpc. These values are based on typical distances to nearby regions of low-mass star formation (e.g., the Taurus molecular cloud) and massive star formation, respectively.

For a locally uniform magnetic field that is weak enough such that any Zeeman splitting is unresolved (Crutcher et al., 1993), the following relationship applies:

$$V = \frac{dI}{d\nu} z_B B_{\mathrm{LOS}} \,, \tag{4.3}$$

where B_{LOS} is the line-of-sight component of the magnetic field. Using this relationship, we may compute the line-of-sight magnetic field strength required (under uniform magnetic field conditions) to achieve the nominal ALMA percentage polarization limit of 1.8%. For this, we ran a sample POLARIS simulation with a uniform magnetic field (oriented along the line-of-sight) in a box with uniform gas density. We then calculated $dI/d\nu$ from the Stokes I profile and found its maximum value, $(dI/d\nu)_{\mathrm{max}}$, as well as the maximum value of the Stokes V profile, V_{max}. Under uniform conditions, the required line-of-sight magnetic field for 1.8% is then

$$B_{\mathrm{LOS}} = 0.018 \times V_{\mathrm{max}} (\frac{dI}{d\nu})^{-1}_{\mathrm{max}} (z_B)^{-1} \,, \tag{4.4}$$

which yields a value of $B_{\mathrm{LOS}} \approx 3.1$ mG in our case. Throughout this work, we refer to this 3.1 mG estimate (in addition to the 1.8% observational limit) as guidance for assessing potentially detectable magnetic field conditions in our simulations. We also sometimes refer to a hypothetical factor-of-ten improved limit at 0.18% and 0.31 mG, respectively. This exercise is undertaken to evaluate the potentially improved utility of conducting Zeeman observations with a next generation circular polarization instrument of the future.

In Table 4.1, we report the fraction of cells in each of our grids with magnetic field component values above 3.1 mG and 0.31 mG.

4.4 Results

Presented in this section are our circular polarization results for both the `lmde` and `MSEnv` models. We include integrated emission maps (Section 4.4.1) and computations of the local polarization percentage in locations across different cuts of the simulated observer-space (Section 4.4.2). We also use 2-dimensional histograms to relate our polarization data to local magnetic field information (Section 4.4.3).

4.4.1 Maps

In Figure 4.5 and Figure 4.6 we show maps (for each of the $x-$, $y-$, and $z-$sightlines) of the observable data obtained from our POLARIS simulations of model `lmde` and model `MSEnv`, respectively. Included are the velocity-integrated Stokes I and Stokes V, the CN optical depth at line-center (τ_{LC}), and a derived percentage polarization quantity that we refer to as the "Median V/I". To calculate this value, we bin down our data from 169 channels to 13 channels, resulting in a velocity resolution of 0.46 km/s that is comparable to that which is typical of Zeeman observations with ALMA. For each pixel in the observer space, we then calculate the ratio of the Stokes V to the Stokes I in each of the 13 re-binned channels. The "Median V/I" for a given pixel is then the 7th highest of these 13 values. Functionally, this parameter produces similar percentage polarization values to comparing the peaks of the Stokes V versus Stokes I, while also imposing the requirement that the majority of channels must have detectable emission (which is a soft criterion for being able to reasonably estimate the local line-of-sight magnetic field strength, e.g., by applying equation 4.3).

Generally, the maps for both models show that the percentage polarization is

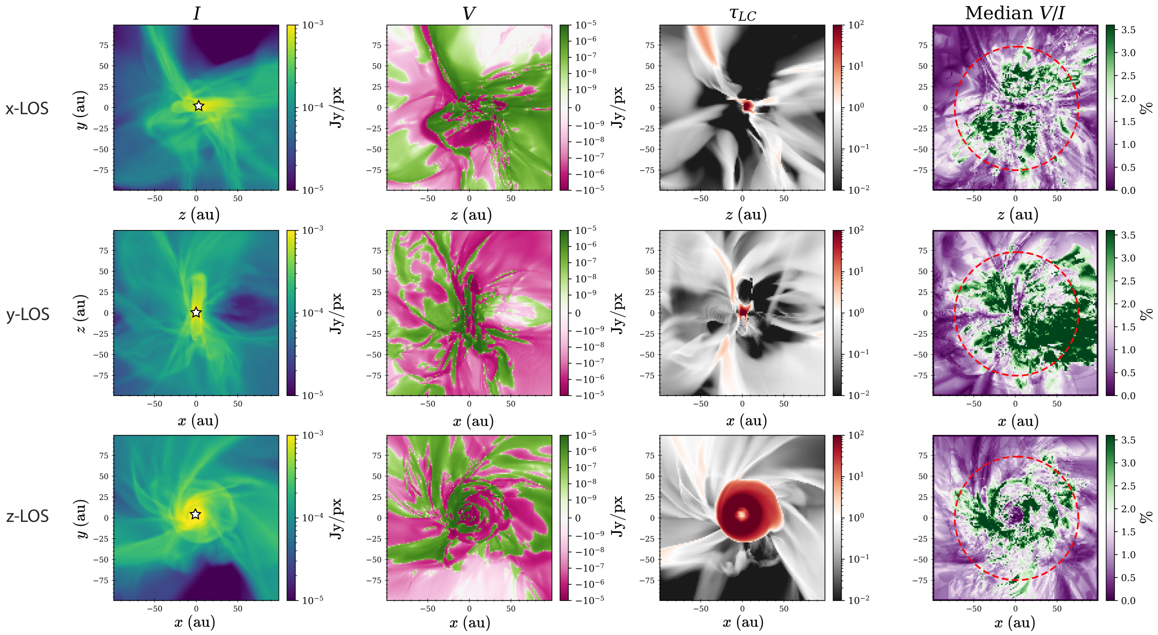

Figure 4.5: Velocity-integrated Stokes I and Stokes V, line center optical depth τ_{LC}, and derived polarization quantity "Median V/I" for each Cartesian view of the `lmde` model. The circle annotated on the last column corresponds to $R = 75$ au.

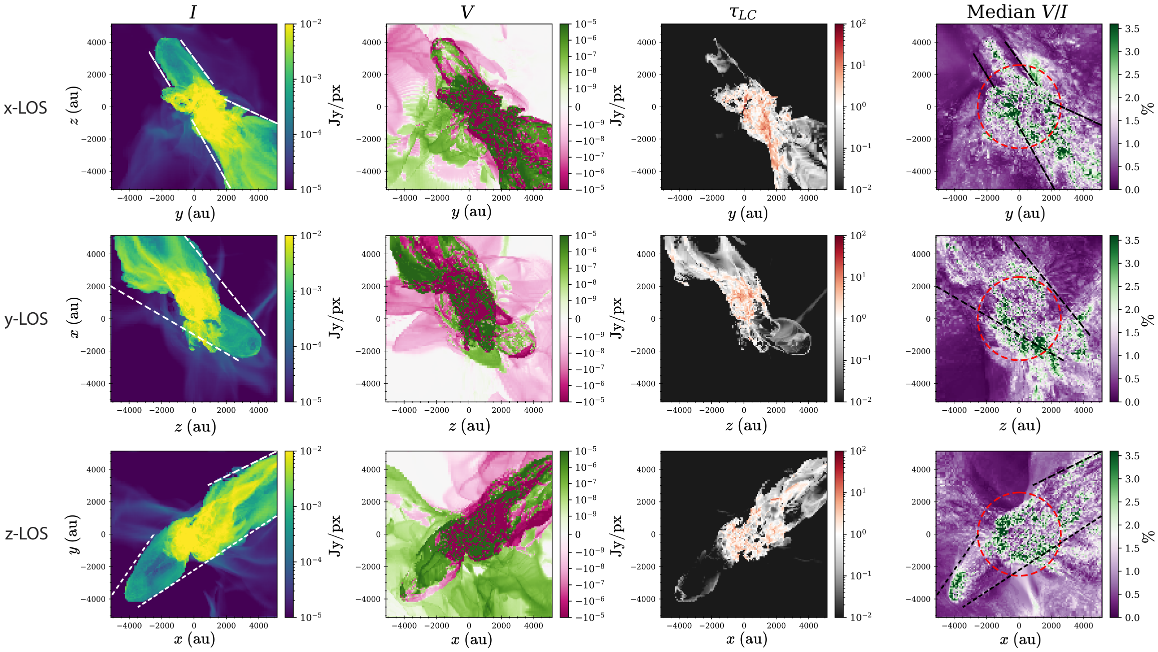

Figure 4.6: Same as Figure 4.5, but now for the `MSEnv` model. The circle annotated on the last column corresponds to $R = 2500$ au. We also draw additional reference lines on the Stokes I panels (in white) and on the Median V/I panels (in black). These sets of lines are co-located with each other and are drawn in by hand to guide visual inspection of the polarization in the CN enhanced shell and its nearby surroundings.

Table 4.1: Percentage of 3D cells on our re-projected fixed grids that have magnetic field component values above 3.1 mG and 0.31 mG. In addition to the full domain, we also perform computations that only include cells within a given radius; the chosen radii are the same we use for cuts in our polarization analysis in Section 4.4.2. For model `MSEnv`, we also report values when only the cells within our CN enhanced shell are considered.

		Percentage of cells above...							
Model	Cutoff	3.1 mG				0.31 mG			
(lr)3-6(lr)7-10		B_x	B_y	B_z	B_{tot}	B_x	B_y	B_z	B_{tot}
`lmde`	-	44.8	61.1	49.1	73.3	93.4	96.9	96.0	99.9
	$R < 75$ au	60.9	77.9	70.6	98.0	95.8	98.4	97.3	100
`MSEnv`	-	24.2	31.4	43.9	42.2	82.1	82.6	92.1	92.3
	$R < 2500$ au	57.2	62.9	72.1	81.2	93.3	91.4	94.0	96.6
	In shell	70.0	68.6	72.2	86.5	97.2	97.3	97.5	99.9

maximized in at an intermediate distance from the central protostar. In model `MSEnv`, for all three viewing angles there is a low polarization "hole" near the star (within $R \lesssim 500$ au) where the line-center optical depth is high ($\tau_{LC} > 1$). Moreover, the locations of high polarization are spatially correlated with the location of the enhanced CN outflow shell defined by our tracer particle constraint.

Our results from model `lmde` also reveal that there is polarization sub-structure when we focus in on the $R \lesssim 100$ au scale near the disk. In this case, however, rather than a roughly spherically symmetrical low polarization "hole," the low polarization region is defined by the shape of the (optically thick) disk. For the edge-on views (i.e., the $x-$ and $y-$sightlines), the percentage polarization is low along the disk midplane, with pixels that exceed 1.8% polarization fraction mainly occurring between $5-75$ au above or below the midplane. In the y line-of-sight, there is also clearly a region of high polarization that spatially overlaps with the location of a disk wind ($z \gtrsim 10$ au along the disk axis). Looking face-on at the disk (z line-of-sight), there is a circular low polarization region near disk center, again corresponding to where $\tau_{LC} > 1$. From this view, pixels in excess of 1.8% tend to occur in a radial band $R \sim [30\text{ au}, 50\text{ au}]$ surrounding the edge of the optically thick disk.

The polarization percentage is also, unsurprisingly, low in the outskirts of the box domains, in the areas far beyond the CN enhanced shell or disk edge, for models `MSEnv` and `lmde` respectively, where the magnetic field tends to be weaker in general.

4.4.2 Percentage Polarization Statistics

As a corollary to Table 4.1, where we listed the fraction of 3D cells with magnetic field strengths above 3.1 mG and 0.31 mG, in Table 4.2 we calculate the fraction of pixels from our simulated emission maps that have percentage polarization ("Median V/I") values above 1.8% and 0.18%. For both simulation types we perform these computations for the full observer-space, as well as for cuts that restrict the domain to more favorable sub-regions (from a percentage polarization perspective). The locations of these cuts are also noted in Table 4.2.

For the low mass disk model `lmde`, we find that across the whole observer space the fraction of cells with fractional polarization above 1.8% is between $\sim$20 − 40% depending on viewing geometry. Interestingly, the y line-of-sight in this case has a higher fractional polarization value largely due to a swath of high polarization pixels along a disk wind. When Cut 1 is applied (i.e., the highest column density cells corresponding to the high τ disk are removed from consideration), there is effectively no change in the fraction of cells with percentage polarization above 1.8%. This is sensible, since the disk only accounts for a small area of the observer space. Visually, as we see in Figure 4.5, it is clear however that the inner disk has quite low polarization. When we add in the restriction to limit the probed space to $R < 75$ au (Cut 2), the percentage polarization increases by factors of $\sim$2, 1.5, and 2 for the $x-$, $y-$, and $z-$lines-of-sight, respectively. This calculation aligns well with what is suggested in the maps; that the regions of high polarization tend to lie spatially in an intermediate range just beyond the disk edge, where the magnetic field is relatively strong and the optical depth is not too high.

The results for the massive star case are qualitatively similar, in that the fraction of pixels above 1.8% polarization is highest when only an annulus is considered. For the whole domain, the percentage of high polarization (>1.8%) pixels is about $\sim$15% for all three Cartesian sightlines. This value increases by about a factor of 2 up to $\sim$30-35% when only pixels within 2500 au of the central star are included (Cut 1). We also define a cut (Cut 2) that additionally removes the polarization "hole" in the x line-of-sight view. The location of this mask is set manually to be centered on the lowest polarization pixel in that region, with a radius of 900 au. Removing the hole from consideration increases the fraction of pixels with percentage polarization above 1.8% from 35% to 41% for the x line-of-sight.

Finally, it is also worth noting that for both models and all cuts, the fraction of cells with percentage polarization above 0.18% always exceeds 90%. This suggests that a hypothetical factor of ten improvement in sensitivity to the fractional circular polarization would result in the vast majority of the envelopes becoming accessible with Zeeman observations.

4.4.3 2-Dimensional Histograms

Here we relate our percentage polarization V/I results to the underlying magnetic field information as well as other observable quantities of interest (i.e., Stokes V and CN τ_{LC}). Two-dimensional histogram plots for models `lmde` and `MSEnv` are presented in Figure 4.7 and Figure 4.8, respectively.

Each plot has significant scatter, suggesting that high polarization can in principle be obtained under a wide variety of envelope conditions. However, there are also some trends apparent in our data that show some characteristics are more favorable than others. As expected, Median V/I scales positively with the density weighted average line-of-sight magnetic field strength (first column of Figures 4.7 and 4.8). Moreover, for both simulations the associated mean trend line tends to pass through a polarization percentage of 1.8% at roughly 3.1 mG. This suggests that this equivalent value for a uniform magnetic field we calculated in Section 4.3 is a useful guide for interpreting envelope Zeeman signatures. That is to say, it is reasonable to expect that robust detections with ALMA should require average magnetic fields strengths $\gtrsim 3$ mG. Note, however, that this value applies only in envelope regions like those we simulate here, where the magnetic field is mostly uniform or only moderately tangled. In regions with more complex (i.e., tangled or wound-up) magnetic field geometry, larger

Table 4.2: Computations of the fraction of pixels in each of our simulated emission maps with percentage polarization values above 1.8% and 0.18%. We report values for the entire box domain for each of the Cartesian lines-of-sight, as well as for some selected cuts within the observer-space.

				Percentage of pixels above...		
Model	LOS	Inner cutoff	Outer cutoff	1.8%	0.18%	Notes
`lmde`	x	-	-	21.8	94.5	Full observer-space
	y	-	-	40.9	95.6	
	z	-	-	24.2	95.9	
	x	$N > 60$ g cm^{-2}	-	21.9	94.6	Cut 1
	y	$N > 60$ g cm^{-2}	-	41.3	95.7	
	z	$N > 60$ g cm^{-2}	-	23.1	96.1	
	x	$N > 60$ g cm^{-2}	$R < 75$ au	39.9	99.8	Cut 2
	y	$N > 60$ g cm^{-2}	$R < 75$ au	62.2	99.8	
	z	$N > 60$ g cm^{-2}	$R < 75$ au	45.3	99.6	
`MSEnv`	x	-	-	17.7	96.4	Full observer-space
	y	-	-	17.6	89.2	
	z	-	-	14.1	96.6	
	x	-	$R < 2500$ au	34.7	97.9	Cut 1
	y	-	$R < 2500$ au	30.6	97.9	
	z	-	$R < 2500$ au	38.8	97.9	
	x	$R > 900$ au	$R < 2500$ au	41.3	99.5	Cut 2

average field strengths will be required to achieve the same polarization percentage. It is also the case that the maximum magnetic field strength (along the line-of-sight) scales positively with median V/I (second column of Figures 4.7 and 4.8). For pixels with percentage polarization greater than 1.8%, this maximum value always exceeds 3.1 mG and can reach as high as ∼10-30 mG, which is consistent with the expectation that the Zeeman-inferred field strength is a lower limit to the maximum field strength found along the line-of-sight.

Another notable trend is that pixels with strong velocity-integrated $|V|$ signals tend to also have large V/I. This is especially true at large $|V|$. This result is convenient for observers, because it means that locations with high percentage polarization will also be the most likely to have a detectable Stokes V signal.

For both model types, there is also a turnover in percentage polarization at an intermediate radius. The peaks occur at approximately ∼30 au for model `lmde` and ∼1500 au for model `MSEnv`. As we touched on in Section 4.4.1, visual inspection of the maps of the observables reveal that these radii correspond approximately to the edge of the optically thick disk and the polarization "hole" for the two model types, respectively.

Assessing percentage polarization trends with line-center optical depth is less clear. Overall, there is a wide range of τ_{LC} values that can produce potentially detectable percentage polarization levels in both envelopes. In model `lmde` there tends to be a moderate anti-correlation between optical depth and V/I, especially in the opacity regime where the majority of the pixels tend to be located ($\log[\tau_{LC}] \sim [-2, 0]$). For the face-on case, there is also a local maximum (in the mean curve) around $\tau_{LC} \sim 0.1$, which lends some credence to the idea the intermediate optical depth may sometimes be favorable. For model `MSEnv` there tends to be low polarization at very small $\tau_{LC} \sim -4$. This is due to low-density ambient region far outside the CN

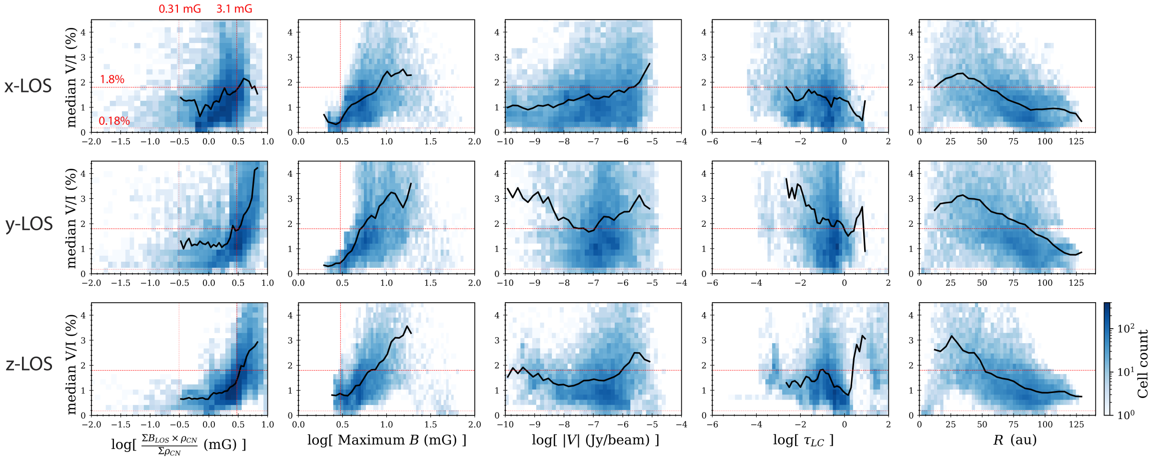

Figure 4.7: Model `lmde` 2-dimensional histograms (for each Cartesian line-of-sight) comparing the median V/I quantity (vertical axis) in each pixel with several other quantities derived from the same pixel. For each pixel these quantities include, from left-to-right, the density weighted average line-of-sight magnetic field strength, the maximum magnetic field strength in any 3D cell along that sightline, the absolute value of the velocity-integrated Stokes V signal, the line-center optical depth, and the distance (in observer space) from the central sink particle.

enhanced shell. Within and near the shell (where $\log[\tau_{LC}] \sim [-2, 1]$) the percentage polarization tends to be close to 1.8% with very little discernible trend, except for a downturn at the highest opacities ($\log[\tau_{LC}] \gtrsim 0$) for the x and y lines-of-sight. This modest anti-correlation corresponds to the polarization "hole," which is evidently not as visible in the $z-$view.

One further caveat that we should note about optical depth is that our simulations are tailored toward the optically thin scenario; we chose our CN abundances such that we would generally have $\tau_{LC} < 1$ throughout the envelopes of our modeled sources. This is in part because we expect modeled optically thin emission to be more directly comparable to observations than optically thick emission. In practice, optically thick regions are subject to additional line effects that make drawing comparisons to modeled emission more tenuous, such as continuum over subtraction and absorption by resolved-out, cold outer envelope material.

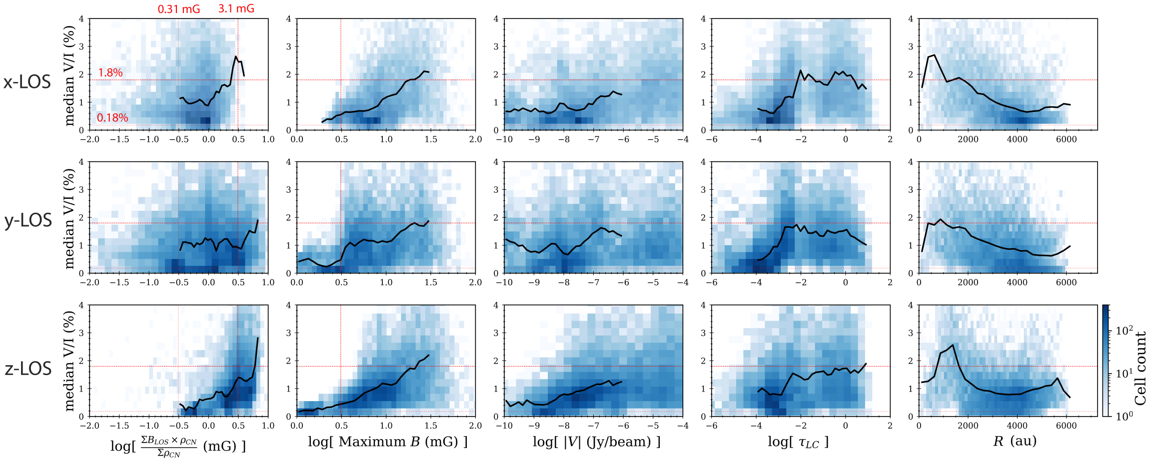

Figure 4.8: Same as Figure 4.7, but now for model `MSEnv`.

4.5 Discussion

Generally, the results of our simulations suggest that observable V/I signals (with e.g., ALMA) are available in both massive and low-mass protostellar envelopes. Therefore, probing magnetic fields in these environment with the Zeeman effect is a tractable goal. Our results also show, however, that there is significant variation in percentage polarization across the envelopes; that is to say, some sight-lines are more favorable than others.

In this discussion, we investigate more deeply some factors that can influence whether a given location is a good candidate to have high percentage polarization: optical depth (Section 4.5.1), CN enhancement on a wind-blown shell (Section 4.5.2), and disk inclination (Section 4.5.3). We then highlight in Section 4.5.4 some additional technical factors that observers should be mindful could also affect the percentage polarization results. Finally, for our `lmde` simulation we provide example lines (Stokes I and Stokes V profiles) from a selected envelope location to give a sense of typical line morphology and linewidth in this model (Section 4.5.5). We also compare the magnitude of the integrated flux found in this simulation to TMC-1, an example

Class I source that is a good candidate for inner envelope Zeeman observations.

4.5.1 Optical Depth

From our 2-dimensional histogram analysis in Section 4.4.3 we concluded that global trends in V/I versus line-center optical depth are not especially clear for either model type. Here, we re-visit the topic with an alternative approach. In Figure 4.9 we plot the radial profiles of two quantities, the fraction of cells with polarization percentage above 1.8% and the average τ_{LC}, within thin annuli of radial size $[R - \Delta r/2, R + \Delta r/2]$. For model `lmde` we set $\Delta r = 6$ au and for model `MSEnv` we set $\Delta r = 300$ au.

Our plots for the model `lmde` show different trends depending on line-of-sight. For the edge-on disk views ($x-$ and $y-$ lines of sight), the percentage of pixels above 1.8% polarization percentage is relatively low at small radius ($R \lesssim 15$ au) then peaks around $R = 20 - 50$ au. In this radial range the average optical depth hovers around $\tau_{LC} \sim 0.2 - 0.4$. Visual inspection of the maps (top two rows of Fig. 4.5) shows us that these results are due to high polarization swaths above and below the disk midplane. The face-on view of model `lmde`, by contrast, shows that the annuli with the highest fraction of high polarization cells also have the highest optical depth. While it is certainly the case that some pixels in the optically thick disk have high polarization, taken at face value this result is perhaps somewhat misleading. Looking at Figure 4.5 again (bottom row), we can see that most of the pixels with median $V/I > 1.8\%$ are either in the transition region near the disk edge (where τ is rapidly decreasing) or further away. Furthermore, in the face-on view of the disk there are opposing radial asymmetries in both the optical depth map and the V/I map in the range $R \sim 30 - 50$ au. Particularly, there is a lobe of high τ_{LC} at positive x, whereas the high V/I extension is at negative x where the CN optical depth is actually lower,

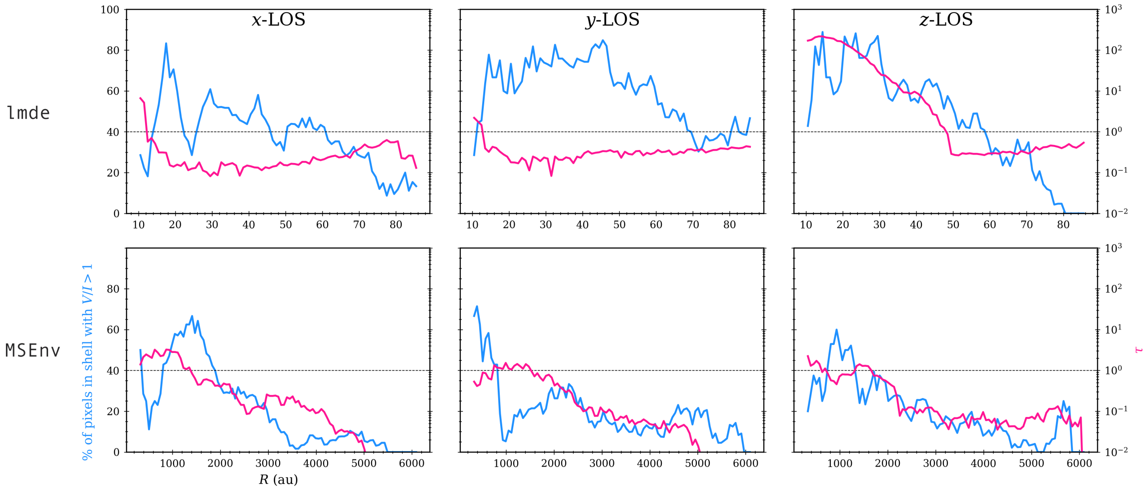

Figure 4.9: Percentage of pixels with median polarization percentage above 1.8% (blue curve) and average (mean) optical depth (pink curve) calculated in thin radial shells, computed for both of our models as observed along each Cartesian line-of-sight. A horizontal line corresponding to a CN line-center optical depth of unity is also annotated on each plot.

at around $\tau_{LC} \sim 0.1 - 1$.

For model `MSEnv`, all three lines-of-sight show similar trends. Though at small R there is some difference in where the high polarization regions lie as a function of radius (this is due to slight differences in the location of the central polarization "hole" for each projection), within $R \lesssim 2500$ au it is generally the case that peaks of the fraction of pixels with $V/I > 1.8\%$ are accompanied by dips in the average line center optical depth (to $\tau_{LC} \lesssim 1$). Outside $R = 2500$ au, both quantities gradually taper off toward the outskirts of the envelope.

4.5.2 CN Enhancement

In our simulations of model `MSEnv` we included a non-uniform abundance prescription, with 3D cells lying within a prescribed shell region (see Fig. 4.4) being supplied with a CN abudance a factor of 1000 larger ($X_{\mathrm{shell}} = 10^{-9}$) than the surrounding ambient material ($X_{\mathrm{shell}} = 10^{-12}$). The results of our radiative transfer simulations for this model therefore give us some opportunity to comment on how the locations of CN enhanced regions, particularly those which may be driven by UV irradiation on the cavity wall from a protostellar wind, can inform observational choices when designing a Zeeman experiment.

In our plot of the observable data from the massive star simulation (Figure 4.6), we annotate reference lines on the Stokes I maps (white dashes) and median V/I maps (black dashes). These lines are co-located and drawn in by hand strictly for visual reference. From inspection of the maps it is clear that the regions of high polarization are well-correlated with the CN enhanced shell. Particularly high polarization occurs near the shell edges surrounding the central polarization "‘hole" or in its lower-intensity (as measured by Stokes I value) fringes. For example, the blown out "tip" of the shell located at $(x, y, z) \sim (-3000 \text{ au}, -1000 \text{ au}, 3000 \text{ au})$ contains many high polarization pixels. These results suggest that interfaces between outflow structures and ambient gas (e.g., due to outflow-swept shells) are prime areas to target, due both to favorable CN abundances and relatively low to intermediate optical depth compared to (low polarization) central regions.

4.5.3 Disk Inclination

So far in this work we have only considered simulations viewed from the Cartesian lines-of-sight (with respect to the frame of our MHD simulations). While this may be sufficient to obtain a good understanding of the `MSEnv` model, which is more-or-less spherically symmetric in its interior region, our results for the `lmde` model show significant contrast in polarization map morphology between the face-on and edge-on disk views.

Figure 4.10 presents percentage polarization results for a series of intermediate disk inclination views of our low mass protostar simulation. The general picture is

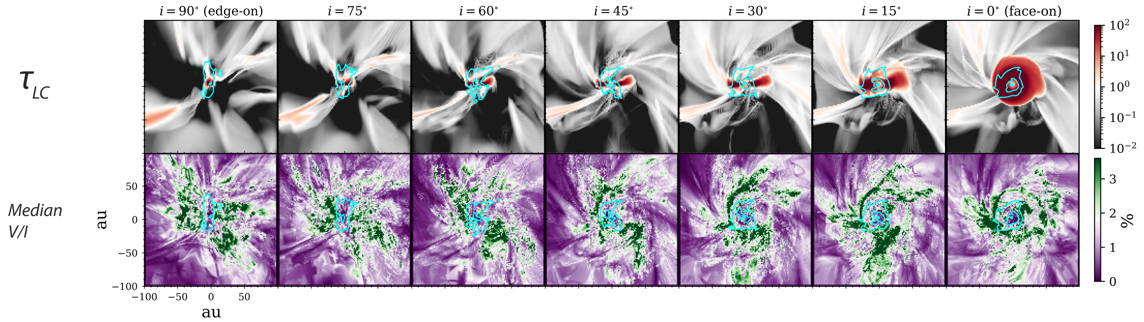

Figure 4.10: Line-center optical depth and median V/I calculated for several intermediate inclination views of model `lmde`. Over-plotted on each panel in cyan are contours corresponding to 5×10^{-4} and 10^{-3} Jy/px, which trace out the brightest parts of the central disk. For all viewing angles, these brightest parts of the disk tend to have low polarization and are immediately surrounded by high polarization regions. For views that are close to edge-on (∼60°-90°) the high polarization regions tend to be above and below the disk midplane, and for views close to face-on (∼0-30°) the high polarization regions roughly form a ring around the optically thick disk.)

similar for all viewing orientations; there is a central (highest intensity in Stokes I and highest optical depth) region that is low in polarization, and it is surrounded by a relatively high polarization envelope. The shapes of the regions with large V/I vary as a function of inclination. As the angle is adjusted from $i = 90^\circ$ (edge-on) to $i = 0^\circ$ (face-on), the high polarization swaths gradually progress from appearing shaped like blocks above and below the disk midplane into a ring near the disk edge. From this experiment we can see that intermediate inclination low mass protostellar envelopes are potential targets for Zeeman experiments, as they also contain many high polarization pixels. They just perhaps have more complex morphology, with the high polarization regions appearing as some combination of "block-like" and "ring-like."

4.5.4 Additional Observational Considerations

In Sections 4.5.4 and 4.5.4 below, we briefly assess the impact beam convolution and stacking of sub-transitions can have on our observational results by considering a few case studies.

Beam Convolution

We test the effect of applying $0.5''$ FWHM beam convolution to the x line-of-sight view of our `MSEnv` model. For this experiment we bin our 169 channels of Stokes I and V data to 13 channels (corresponding to an observed velocity resolution of 0.46 km/s) as usual, then at that stage apply a Gaussian filter to each of those 13 channels. We then use those data to compute velocity-integrated I and V, line-center CN optical depth, and the median V/I.

A side-by-side comparison of our high resolution maps (i.e., with no beam convolution) and our $\theta_{\rm FWHM} = 0.5''$ maps are presented in Figure 4.11. We also include histograms of each observable to compare their values in aggregate. In addition to the obvious morphological changes from Gaussian smoothing, the main effect is in the V/I map. Clearly, the values of the pixels with the highest percentage polarization are significantly reduced. This is an expected result, as beam convolution effectively averages adjacent pixels. Therefore, any high polarization regions that are smaller than the beam size will have some contribution from low polarization pixels post-convolution. This effect is captured in the histograms as well. The overall Stokes I and V distributions are similar in shape, but the convoluted V/I distribution is notably narrower than the unconvolved version. The percentage of pixels above 1.8% fractional polarization is $\sim$15% for the unconvolved map and $\sim$3% for the convolved map. Meanwhile, the percentage of pixels above 0.18% fractional polarization is $\sim$94% for the unconvolved map and $\sim$99% for the convolved map. It should also be noted that the two V/I distributions peak at roughly the same value, $V/I \sim 0.8\%$.

These results suggest that either high sensitivity (V/I limit $< 1.8\%$) or high resolution ($\theta_{\rm FWHM} < 0.5''$), or a combination of both, would be of great advantage for

Zeeman experiments in this type of environment.

Stacking Sub-Transitions

The CN $J = 1 - 0$ molecular line comprises nine velocity-resolved hyperfine sub-transitions. For the preceding sections of this work we only considered one representative transition, the 113.144 GHz component. Here, we perform simulations of all seven[4] of the sub-components that are available by default in POLARIS. We run these computations on the face-on (z line-of-sight) view of our low mass disk envelope simulation, which serves as a good test case because it contains a wide variety of optical depth conditions.

We find that each of the seven components have nearly identical Stokes I, V, and τ morphology, so the main effect of stacking is a boosted gain in signal. In Figure 4.12 we compare velocity-integrated I and V, and median V/I maps obtained from the stacked transitions versus those from the representative transition. We also compute the ratio between the stacked value and representative transition value for each of these quantities. Stacking produces a (per pixel) boost in the I signal by a factor of ~7-10, with the distribution strongly peaked at roughly factor of 8. The V signal is boosted by roughly the same factor on average, but the distribution is a bit broader; some pixels reach as high as a factor of ~25 brighter. Finally, the median V/I is about the same for the stacked data as it is for the single sub-transition. Interestingly, the regions with the lowest values for this quantity $[(V/I)_{\rm stacked}/(V/I)_{\rm Rep.} \sim 0.8]$ tend to be located within the optically thick disk, and the regions where stacking increases V/I tend to be in the envelope.

---

[4] These are the seven "main" transitions in the CN $J = 1 - 0$, the other two have much lower intensity.

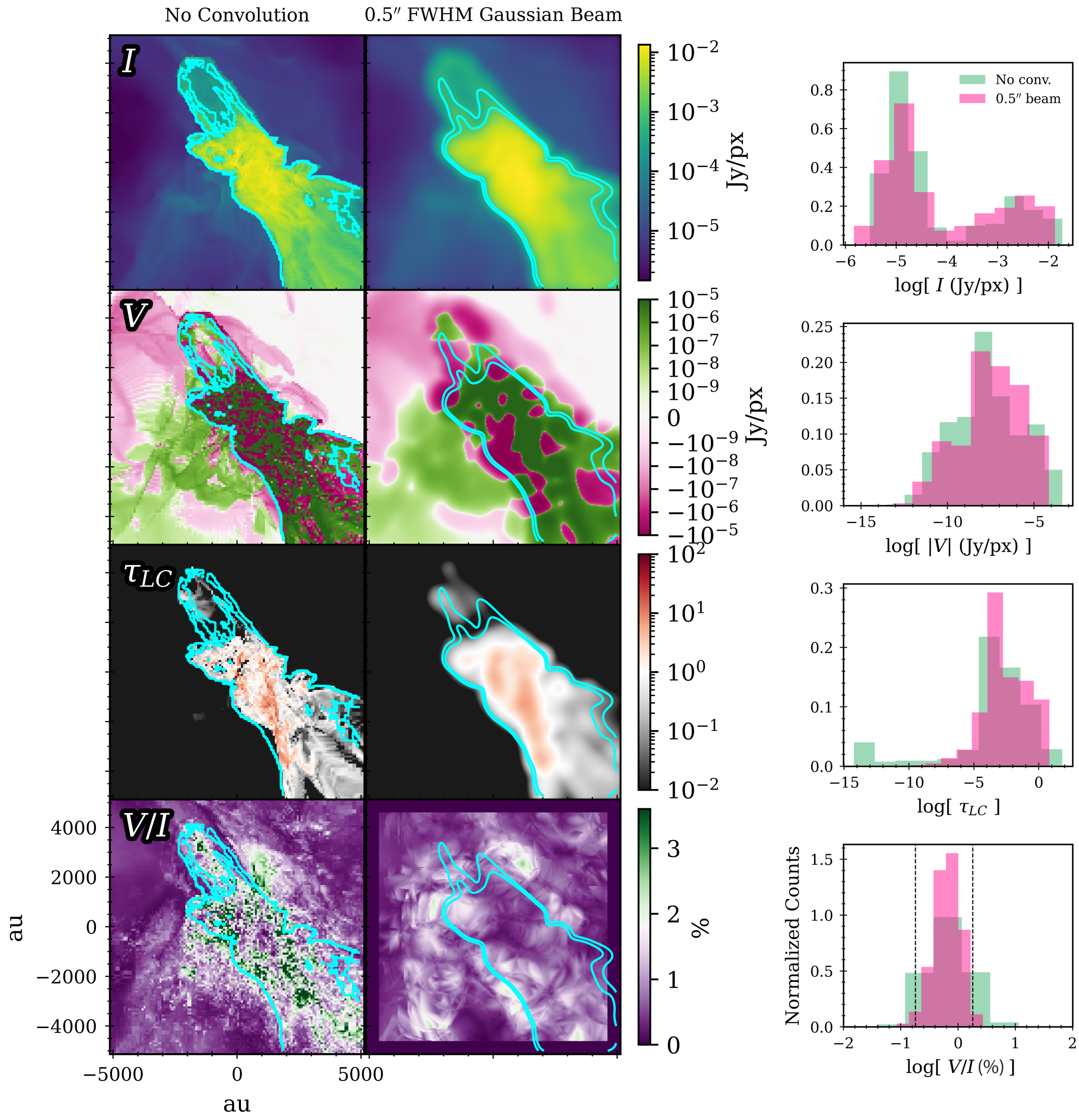

Figure 4.11: ***Left:*** Comparison of velocity-integrated Stokes I and V, line-center optical depth, and median polarization percentage between pixel resolution and $\theta_{\mathrm{FWHM}} = 0.5''$ beam convolved cases, for model `MSEnv` as viewed from the x line-of-sight. The cyan contours correspond to Stokes I values of 5×10^{-4} and 10^{-3} Jy/px. ***Right:*** Histogram plots comparing the distribution of each observable for the unconvolved versus convolved cases. The main effect of applying beam convolution is that the V/I distribution narrows, resulting in fewer pixels having percentage polarization values above 1.8%. The distribution remained peaked at roughly the same value, however ($V/I \sim 0.8\%$).

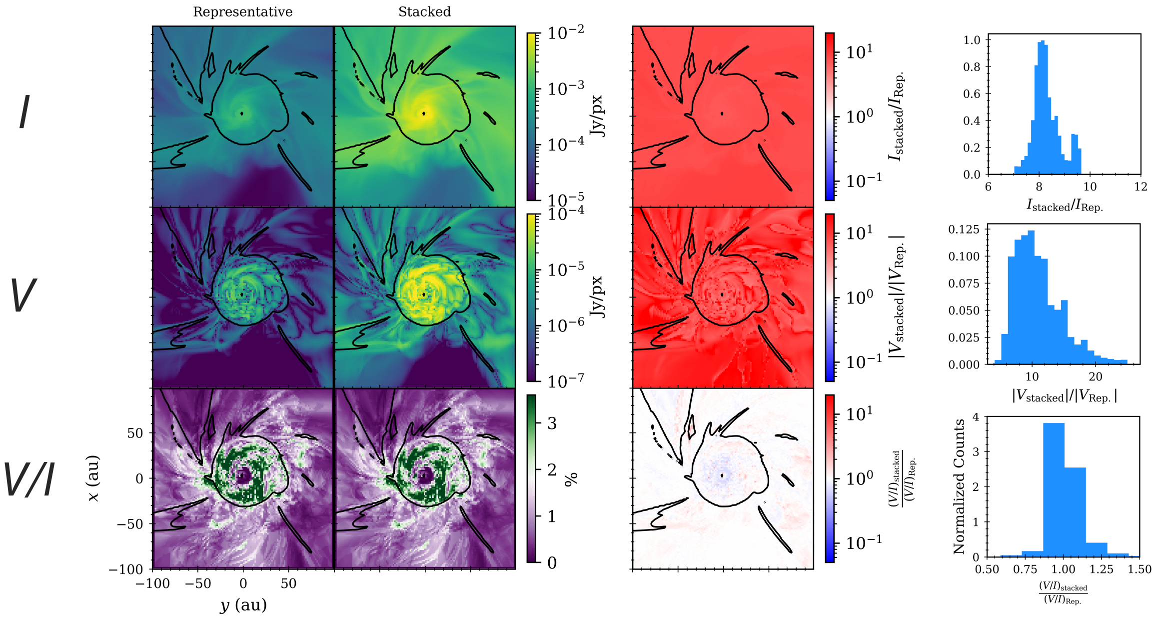

Figure 4.12: ***Left:*** Comparison of the velocity-integrated I and V signals and median polarization percentage calculated from the single 113.144 GHz representative transition versus those calculated after sub-transition stacking. Over-plotted contours correspond to $\tau_{LC} = 1$. ***Center***: Pixel-by-pixel ratios of the observables for the stack versus the representative transition. ***Right***: Histogram plots of the same ratios. We generally find that the amount of signal boost gained from stacking has some modest pixel-by-pixel variation, with both distributions centered on a factor of ∼8.

4.5.5 Example lines in model `lmde` and comparison of integrated Stokes I flux to TMC-1

From the perspective of an observer, it is also useful to get a sense of what the Stokes I and V line profiles look like in a typical envelope beam. In Figure 4.13, we provide the velocity-integrated brightness temperature (in K km s^{-1} units) for each pixel from the face-on view of model `lmde`, as well as Stokes I and V profiles taken from an example location in the envelope.

The line shapes observed in this location are generally representative of what we see across the envelope, with roughly Gaussian Stokes I emission (the particular shape of the line, however, will of course depend on the velocity structure of the chosen location, and the viewing angle). Notably, the Stokes V morphology matches well with the $dI/d\nu$ fit, which is consistent with the expectation of a fairly uniform, well-behaved line-of-sight magnetic field in the envelope (see e.g., Fig. 4.2). Incidentally, the percentage polarization we obtain at this particular location is $\sim$1%.

Using the velocity-integrated surface brightness in each pixel (i.e., the left panel of Figure 4.13), we can also compare the fluxes obtained in our modeling with real observed fluxes. Particularly, TMC-1 is a Class I source with known bright CN emission (Tychoniec et al., 2021). It has been observed to have CN $J = 2 - 1$ ($\nu_0 = 226$ GHz) emission with velocity-integrated surface brightness values between $\sim$50-150 mJy beam^{-1} km s^{-1} in its inner envelope. Since the line transition with which TMC-1 was observed is different from that we used in our modeling (CN $J = 1 - 0$, with $\nu_0 = 113$ GHz), we convert to velocity-integrated brightness temperature for this comparison. Noting that the observation of TMC-1 in Tychoniec et al. (2021) used a beam size of $\approx$0.16 arcsec^2, we calculate the velocity-integrated specific intensity and then use the Rayleigh-Jeans equation to compute the corresponding velocity-

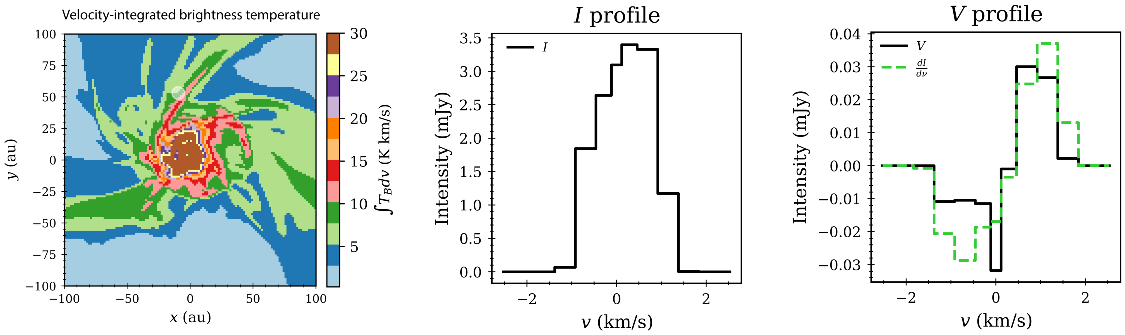

Figure 4.13: ***Left***: Velocity-integrated brightness temperature for each pixel in the face-on view of our `lmde` model, expressed in K km s^{-1} units. Also annotated on the plot is a translucent white circle, which represents an example beam location. ***Middle and Right***: Stokes I and Stokes V profiles calculated from the annotated example beam, to demonstrate the line morphology and linewidth for a typical envelope location. Also included on the V profile plot is a fit curve using $dI/d\nu$. For this particular location, we obtain a polarization percentage of ~1%.

integrated brightness temperature. The result we obtain is that 50-150 mJy beam^{-1} km s^{-1} corresponds to approximately 8-25 K km s^{-1}. These values are roughly comparable to those found in our simulated disk-envelope system, which has velocity-integrated brightness temperatures of ~8-20 K km s^{-1} in the inner envelope. The modeling we've conducted throughout this work suggests that envelope locations with CN surface brightnesses in this general range are able to yield detectable emission with fractional polarization of order ~2%. Sources with known bright CN emission (such as TMC-1) should be prioritized when considering targets for envelope Zeeman experiments.

4.6 SUMMARY

In this work, we produced simulated Zeeman emission maps of the CN $J = 1 - 0$ molecular line transition from MHD simulations of low-mass star formation and massive star formation regions. We calculated the V/I percentage polarization throughout the envelopes of each environment and then placed these results in context by comparing them with the local magnetic field data supplied from the 3-dimensional inputs. We also compared our results with nominal instrumental limits to assess the current and future feasibility of using Zeeman observations of protostellar envelopes to broadly diagnose magnetic field character during the early embedded phase of star formation. Our principal conclusions are summarized below:

1. In 3D, both models contain cells with magnetic field strengths that are in principle sufficiently large to produce circularly polarized emission that may be detectable with current instruments (Table 4.1). Intrinsically, roughly ∼45-60% of cells (depending on viewing orientation) in our low mass disk envelope system and ∼25-45% of cells in our massive star envelope system have local line-of-sight magnetic field strengths that exceed 3.1 mG, the line-of-sight magnetic field strength we estimate to in principle be needed to reach a polarization percentage of 1.8%, the nominal ALMA limit. Furthermore, if we ignore the low density diffuse outskirts (by placing cuts at $R < 75$ au and $R < 2500$ au for models `lmde` and `MSEnv`, respectively), these percentages increase to ∼60-70%.

2. Our simulated emission maps yield pixel-by-pixel polarization results that vary significantly across the observer space. Each simulation contains some regions with very low polarization and others that well exceed 1.8% (see, e.g., the final column of Figures 4.5 and 4.6). Broadly, the low polarization regions tend to be near the edges of the simulation box or in the central, highest intensity and optical depth sight lines. This leaves an intermediate range (in both radius and optical depth) where high polarization cells are preferentially located. For our low mass disk envelope model this favorable area corresponds to the regions just beyond the optically thick disk, and for our massive protostar envelope model it mainly corresponds to the regions just surrounding the central low-polarization

"hole." Though it is difficult to identify a clearly optimal optical depth that maximizes V/I, overall it appears that $\tau_{LC} \sim 0.1 - 1$ tends to produce the best conditions for a protostellar envelope Zeeman experiment.

3. For both model types, there are significant portions of the respective envelopes that produce percentage polarizations that in principle are accessible with current instruments (i.e., above the nominal ALMA limit, see Table 4.2). For our low mass disk envelope model, we found the percentage of pixels above 1.8% fractional polarization to be between $\sim$20 − 40% (depending on line-of-sight). This increases to $\sim$40 − 60% when the low intensity ambient material outside $R = 75$ au is excluded. Meanwhile, for the massive protostellar envelope model the percentage of pixels above 1.8% fractional polarization is $\sim$15% overall, and $\sim$30 − 40% when we consider only pixels within $R = 2500$ au. Furthermore, both models have $> 90\%$ pixels above 0.18% polarization, meaning that a factor of ten improvement in sensitivity to the magnetic field strength beyond the current ALMA limit would in principle make essentially the entirety of these envelopes accessible to Zeeman experiments. One caveat that should be noted, however, is that in this work we study emission maps produced directly from radiative transfer software. This type of simulation is useful for offering theoretical guidance, but a true direct observational comparison would require producing synthetic observations [e.g., using the CASA observing tool (McMullin et al., 2007)], which is outside the scope of this work.

4. We find that the percentage polarization in a given pixel is positively correlated with the density weighted average line-of-sight magnetic field strength (first column of Figures 4.7 and 4.8). For each of our simulations the associated mean trend line passes through a polarization percentage of 1.8% at roughly

3.1 mG, the reference value we predicted using Eq. 4.3.

5. We find that percentage polarization is positively correlated with the magnitude of the Stokes V signal, especially at large $|V|$ (third column of Figures 4.7 and 4.8). This suggests that the regions that are most favorable in terms of polarization percentage are also the most favorable in terms of raw Zeeman signal.

6. Some regions of high polarization in our massive protostar model are spatially correlated with the location of the shell we included to simulate a cavity from a protostellar wind (see first and last columns of Figure 4.6). Such sites are predicted to be locations of CN enhancement due to far-ultraviolet dissociation chemistry, and may therefore be good targets for Zeeman experiments with CN.

7. Stacking the seven main sub-components of the CN $J = 1 - 0$ transition in our low mass disk envelope simulation yielded an average signal boost of a factor of about 8, with some pixel-to-pixel variation (between about ∼6-10 for the Stokes I and ∼7-25 for the Stokes V). Stacking affects the percentage polarization results only modestly, decreasing V/I in some parts of the optically thick disk and increasing V/I in parts of the envelope by up to ∼20% (Figure 4.12).

8. Convolution of the emission from our massive protostellar envelope with a $\theta_{\mathrm{FWHM}} = 0.5''$ beam resulted in a narrower distribution of observed V/I values, reducing the fraction of pixels with percentage polarizations above 1.8% (Figure 4.11). Both the unconvolved and convolved maps have an average $V/I \sim 0.8\%$. These results indicate that high-resolution observations offer significant advantages to detection prospects for Zeeman experiments in protostellar envelope environments.

CHAPTER 5

CONCLUSION

In this section I present a non-comprehensive summary of the main outcomes of the three works that comprise this thesis. I also provide some notes on potential continuations of these works and possible future projects.

5.1 SUMMARY

In this thesis we performed modeling of polarized emission to study the role of magnetic fields in a variety of star forming environments, ranging in scale from a molecular cloud, to stellar envelope systems, to a protoplanetary disk. This work produces new intuition on how physical conditions and observing geometry affect the nature of the incoming polarization data, and our results will help guide the interpretation of future polarization observations in each of these regimes.

In Chapter 2, we focused our attention on circularly polarized Zeeman emission in a protoplanetary disk. We modeled the CN $J = 1-0$ suite of hyperfine line transitions in an AS 209-like source and computed the Stokes I and V profiles and channel maps for several different simulation setups. One of our notable conclusions was that the morphology of the emission depends strongly on the morphology of the disk magnetic field, with torodial and vertical (poloidal) configurations giving distinct polarization patterns. We also tested the effects of varying the inclination of the disk, as well as the shape and abundance of the CN emitting region within the disk. Overall, the goal of this project was to produce a grid of many results that can be used as a point of comparison for future Zeeman observations of disks, as the circular polarization mode on ALMA continues to ramp up in its use for scientific programs.

In Chapter 3, we shifted gears to the molecular cloud environment. We ran two realizations of a five parsec turbulent cloud simulation, one with a weaker magnetic field ($M_A = 4$) and one with a stronger magnetic field ($M_A = 1$). For each case we then performed synthetic polarimetric observations to calculate mock polarization vectors, used to trace the plane-of-the-sky magnetic field orientation across the cloud. These calculations were paired with radiative transfer modeling of low-, intermediate-, and high-density molecular gas tracers to model molecular gas structure observations. We then applied the histogram of relative orientations (HRO) technique (Soler et al., 2013) to compare the orientation of the magnetic field with the orientation of molecular gas structure. Our analysis proceeded much in kind with the work by the BLAST team in their study of the Vela C molecular cloud. Particularly, in Fissel et al. (2019) the team applied the same HRO technique to BLASTPol data (magnetic field information) and Mopra data (molecular gas information).

In our theoretical work, we found that the HRO outcomes were quite different for the weaker and stronger magnetic field cases. Whereas the weak field simulation showed little to no differentiation between high- and low-density molecular tracers (i.e., none of them had any preferred orientation relative to the magnetic field), the strong field simulation showed a preference for the perpendicular alignment in the high-density tracers (e.g., $C^{18}O$, CS) and parallel alignment in the low density tracers (e.g., ^{12}CO). Overall, the BLASTPol results were much more consistent with our strong magnetic field results, suggesting that Vela C has a dynamically important magnetic field. As the BLAST team continues to work toward the development of a next generation ballooning experiment, this picture will eventually be clarified further not only for Vela C, but several other molecular cloud targets as well.

Finally, in Chapter 4, true to the thesis title, we bridged the small-scale (disk) and large-scale (molecular cloud) work from the previous two chapters by performing polarization modeling at an intermediate (protostellar envelope) scale. One of the outcomes of our work in Chapter 2 was the result that disks are expected to have highly suppressed Zeeman emission, due to cancellation in the toroidal magnetic field component. This makes directly detecting magnetic fields in disks a challenging task given the current sensitivity limits of ALMA. A potentially fruitful alternative approach for accessing magnetic field information in prototstellar objects, then, is to instead target the envelope of a Class 0/I source. Though the total strength of the magnetic field in such a source is expected to be weaker than in a Class II disk, we also generally expect there to be less field line tangling (and therefore, less cancellation). To test the veracity of this idea, we performed CN $J = 1 - 0$ Zeeman synthetic observations of the envelopes of a stellar mass protostar and a massive ($M_{\rm star} \approx 15\ M_\odot$) protostar. In both cases, we found that large swaths of the envelopes produced percentage polarization values above the nominal ALMA limit (1.8%). As predicted, the fractional polarization in the stellar mass protostar was largest in the inner envelope, just beyond the edge of the disk. The results of our work therefore suggest that these envelope regions are in principle accessible with current instruments, and ALMA programs that aim to target such sources may be a useful way to study magnetic fields in protostellar objects.

5.2 FUTURE WORK

The work performed in this thesis naturally lends itself to future projects, in both the theoretical and observational domains. Though our work in Chapter 2 was a quite comprehensive study of the Zeeman emitting CN gas in a disk, we only considered a single optically thin dust prescription. One potential way to alleviate the cancellation caused by a toroidal magnetic field would be an optically thick midplane dust layer. In a moderately inclined disk, such a layer could block out the far side. Since the cancellation we saw in our model was largely caused the sign flip in the magnetic field direction across the midplane, this could substantially boost the signal seen by an observer. A project more carefully examining this possibility would be useful to help us better understand if sources with optically thick dust midplanes are good targets to consider for Zeeman experiments.

In terms of Zeeman observations, there are a few paths forward. First, one of the main criteria available for selecting good disks to observe is the strength of the CN signal; brighter CN regions of course increase the prospects for a detection. Therefore, a useful observing program would be a comprehensive survey of CN in nearby disks to establish which are (from a Stokes I signal perspective) the best sources to consider pursuing. The outcome of such a survey, in combination with the theoretical intuition driven from my PhD projects, can then be used to develop future circular polarization observing programs. Second, our work in Chapter 4 established that the envelopes of Class 0/I objects can potentially produce Zeeman emission that is detectable with ALMA. Our group has used this result to motivate an ALMA proposal to observe CN $J = 2 - 1$ circularly polarized emission in the envelope of TMC-1, a nearby Class I source with known bright CN emission (Tychoniec et al., 2021). This proposed program was accepted, and will hopefully be observed in the near future.

There is also much work that can be done in cloud- and filament-scale linear polarization science. In Chapter 3 we showed that optical depth played an important role in producing different HRO results for different molecular tracers, with the optically thick ^{12}CO tracing the outer layers of the cloud and optically thin tracers probing into the high-density midplane layers. A more comprehensive study of this effect would be useful. This could be accomplished by, for example, re-scaling a single ideal-MHD simulation to several different box sizes (and therefore, densities), then performing radiative transfer calculations for each realization. Such an experiment would help diagnose how the HRO results might change for similar clouds with different overall opacity conditions.

Previous work by the BLAST theory team has also focused on so-called "joint correlations" between various quantities (such as polarization fraction, column density, and the local dispersion of polarization angles) to develop tools for diagnosing how the magnetic field characteristics affect the observables. Particularly, King et al. (2018) performed this analysis on a colliding flow cloud geometry. Repeating this line of work in a collapsing-cloud simulation (like the one we used in Chapter 3) could help illuminate how this technique applies more generally, as well as highlight any important differences that may occur due to the change in geometry.

Finally, new linear polarization instruments such as the TolTEC camera at the Large Millimeter Telescope (LMT) in Sierra Negra, Mexico and Prime-Cam at CCAT-prime on Cerro Chajnantor (adjacent to the ALMA site) promise to offer new high resolution views of cloud-, filament-, and core-scale magnetic fields in the coming years.

REFERENCES

André, P., Basu, S., & Inutsuka, S. 2009, The formation and evolution of prestellar cores, ed. G. Chabrier (Cambridge University Press), 254

André, P., Di Francesco, J., Ward-Thompson, D., et al. 2014, in Protostars and Planets VI, ed. H. Beuther, R. S. Klessen, C. P. Dullemond, & T. Henning, 27

Andrews, S. M., Wilner, D. J., Hughes, A. M., Qi, C., & Dullemond, C. P. 2009, The Astrophysical Journal, 700, 1502

Andrews, S. M., Huang, J., Pérez, L. M., et al. 2018, The Astrophysical Journal Letters, 869, L41

Armitage, P. J. 2019, Saas-Fee Advanced Course, 45, 1

Arulanantham, N., France, K., Cazzoletti, P., et al. 2020, The Astronomical Journal, 159, 168

Avenhaus, H., Quanz, S. P., Garufi, A., et al. 2018, The Astrophysical Journal, 863, 44

Bai, X.-N. 2013, The Astrophysical Journal, 772, 96

Balbus, S. A., & Hawley, J. F. 1991, The Astrophysical Journal, 376, 214

Ballesteros-Paredes, J., Klessen, R. S., Mac Low, M. M., & Vazquez-Semadeni, E. 2007, in Protostars and Planets V, ed. B. Reipurth, D. Jewitt, & K. Keil, 63

Barnett, S. J. 1915, Physical Review, 6, 239

Beltrán, M. T., Padovani, M., Girart, J. M., et al. 2019, Astronomy and Astrophysics, 630, A54

Bergin, E. A., & Tafalla, M. 2007, Annual Review of Astronomy and Astrophysics, 45, 339

Bertrang, G. H. M., Flock, M., & Wolf, S. 2017, Monthly Notices of the Royal Astronomical Society, 464, L61

Bjorkman, J. E., & Wood, K. 2001, The Astrophysical Journal, 554, 615

Blandford, R. D., & Payne, D. G. 1982, Monthly Notices of the Royal Astronomical Society, 199, 883

Brauer, R., Wolf, S., & Flock, M. 2017a, Astronomy and Astrophysics, 607, A104

Brauer, R., Wolf, S., Reissl, S., & Ober, F. 2017b, Astronomy and Astrophysics, 601, A90

Caselli, P., Benson, P. J., Myers, P. C., & Tafalla, M. 2002, The Astrophysical Journal, 572, 238

Cazzoletti, P., van Dishoeck, E. F., Visser, R., Facchini, S., & Bruderer, S. 2018, Astronomy and Astrophysics, 609, A93

Chandrasekhar, S., & Fermi, E. 1953, The Astrophysical Journal, 118, 113

Chapillon, E., Guilloteau, S., Dutrey, A., Piétu, V., & Guélin, M. 2012, Astronomy and Astrophysics, 537, A60

Chen, C.-Y., King, P. K., & Li, Z.-Y. 2016, The Astrophysical Journal, 829, 84

Chen, C.-Y., Li, Z.-Y., King, P. K., & Fissel, L. M. 2017, The Astrophysical Journal, 847, 140

Ching, T. C., Li, D., Heiles, C., et al. 2022, Nature, 601, 49

Cho, J., & Lazarian, A. 2007, The Astrophysical Journal, 669, 1085

Cho, J., & Yoo, H. 2016, The Astrophysical Journal, 821, 21

Chuss, D. T., Andersson, B. G., Bally, J., et al. 2019, The Astrophysical Journal, 872, 187

Cleeves, L. I., Bergin, E. A., Qi, C., Adams, F. C., & Öberg, K. I. 2015, The Astrophysical Journal, 799, 204

Cox, E. G., Harris, R. J., Looney, L. W., et al. 2018, The Astrophysical Journal, 855, 92

Crutcher, R. M. 2012, Annual Review of Astronomy and Astrophysics, 50, 29

Crutcher, R. M., & Kemball, A. J. 2019, Frontiers in Astronomy and Space Sciences, 6, 66

Crutcher, R. M., Troland, T. H., Goodman, A. A., et al. 1993, The Astrophysical Journal, 407, 175

Crutcher, R. M., Troland, T. H., Lazareff, B., & Kazes, I. 1996, The Astrophysical Journal, 456, 217

Crutcher, R. M., Troland, T. H., Lazareff, B., Paubert, G., & Kazès, I. 1999, The Astrophysical Journal Letters, 514, L121

Crutcher, R. M., Wandelt, B., Heiles, C., Falgarone, E., & Troland, T. H. 2010, The Astrophysical Journal, 725, 466

Cunningham, A. J., Klein, R. I., Krumholz, M. R., & McKee, C. F. 2011, The Astrophysical Journal, 740, 107

Davis, Leverett, J., & Greenstein, J. L. 1951, The Astrophysical Journal, 114, 206

Draine, B. T., Roberge, W. G., & Dalgarno, A. 1983, The Astrophysical Journal, 264, 485

Dullemond, C. P., Juhasz, A., Pohl, A., et al. 2012, RADMC-3D: A multi-purpose radiative transfer tool, Astrophysics Source Code Library, record ascl:1202.015, ,

Elmegreen, B. G. 2000, The Astrophysical Journal, 530, 277

Evans, II, N. J., Dunham, M. M., Jørgensen, J. K., et al. 2009, The Astrophysical Journal Supplement Series, 181, 321

Falgarone, E., Troland, T. H., Crutcher, R. M., & Paubert, G. 2008, Astronomy and Astrophysics, 487, 247

Favre, C., Fedele, D., Maud, L., et al. 2019, The Astrophysical Journal, 871, 107

Fedele, D., Tazzari, M., Booth, R., et al. 2018, Astronomy and Astrophysics, 610, A24

Fiedler, R. A., & Mouschovias, T. C. 1993, The Astrophysical Journal, 415, 680

Field, G. B. 1956, The Astrophysical Journal, 124, 555

Fissel, L. M., Ade, P. A. R., Angilè, F. E., et al. 2016, The Astrophysical Journal, 824, 134

—. 2019, The Astrophysical Journal, 878, 110

Flaherty, K. M., Hughes, A. M., Rosenfeld, K. A., et al. 2015, The Astrophysical Journal, 813, 99

Fuente, A., Navarro, D. G., Caselli, P., et al. 2019, Astronomy and Astrophysics, 624, A105

Galitzki, N., Ade, P. A. R., Angilè, F. E., et al. 2014, in Society of Photo-Optical Instrumentation Engineers (SPIE) Conference Series, Vol. 9145, Ground-based and Airborne Telescopes V, ed. L. M. Stepp, R. Gilmozzi, & H. J. Hall, 91450R

Galli, D., & Shu, F. H. 1993, The Astrophysical Journal, 417, 243

Girart, J. M., Rao, R., & Marrone, D. P. 2006, Science, 313, 812

Gong, H., & Ostriker, E. C. 2011, The Astrophysical Journal, 729, 120

González-Casanova, D. F., & Lazarian, A. 2017, The Astrophysical Journal, 835, 41

Goodman, A. A., Benson, P. J., Fuller, G. A., & Myers, P. C. 1993, The Astrophysical Journal, 406, 528

Goodman, A. A., Crutcher, R. M., Heiles, C., Myers, P. C., & Troland, T. H. 1989, The Astrophysical Journal Letters, 338, L61

Goodman, A. A., & Heiles, C. 1994, The Astrophysical Journal, 424, 208

Harrison, R. E., Looney, L. W., Stephens, I. W., et al. 2021, The Astrophysical Journal, 908, 141

Hartmann, L., Ballesteros-Paredes, J., & Bergin, E. A. 2001, The Astrophysical Journal, 562, 852

Heiles, C., & Crutcher, R. 2005, in Cosmic Magnetic Fields, ed. R. Wielebinski & R. Beck, Vol. 664, 137

Heiles, C., & Troland, T. H. 1982, The Astrophysical Journal Letters, 260, L23

—. 2004, The Astrophysical Journal Supplement Series, 151, 271

Hennebelle, P., & Fromang, S. 2008, Astronomy and Astrophysics, 477, 9

Hennebelle, P., & Pérault, M. 2000, Astronomy and Astrophysics, 359, 1124

Hoang, T., & Lazarian, A. 2009, The Astrophysical Journal, 697, 1316

Hu, Y., Yuen, K. H., & Lazarian, A. 2019a, The Astrophysical Journal, 886, 17

Hu, Y., Yuen, K. H., Lazarian, A., et al. 2019b, The Astrophysical Journal, 884, 137

Hueso, R., & Guillot, T. 2005, Astronomy and Astrophysics, 442, 703

Inoue, T., Inutsuka, S.-i., & Koyama, H. 2007, The Astrophysical Journal Letters, 658, L99

Johansen, A., Youdin, A., & Klahr, H. 2009, The Astrophysical Journal, 697, 1269

Jow, D. L., Hill, R., Scott, D., et al. 2018, Monthly Notices of the Royal Astronomical Society, 474, 1018

Kalugina, Y., & Lique, F. 2015, Monthly Notices of the Royal Astronomical Society, 446, L21

Kataoka, A., Okuzumi, S., & Tazaki, R. 2019, The Astrophysical Journal Letters, 874, L6

Kataoka, A., Tsukagoshi, T., Pohl, A., et al. 2017, The Astrophysical Journal Letters, 844, L5

Kataoka, A., Muto, T., Momose, M., et al. 2015, The Astrophysical Journal, 809, 78

Kataoka, A., Tsukagoshi, T., Momose, M., et al. 2016, The Astrophysical Journal Letters, 831, L12

King, P. K., Fissel, L. M., Chen, C.-Y., & Li, Z.-Y. 2018, Monthly Notices of the Royal Astronomical Society, 474, 5122

Kolmogorov, A. 1941, Akademiia Nauk SSSR Doklady, 30, 301

Körtgen, B., & Banerjee, R. 2015, Monthly Notices of the Royal Astronomical Society, 451, 3340

Lada, C. J. 1987, in IAU Symposium, Vol. 115, Star Forming Regions, ed. M. Peimbert & J. Jugaku, 1–17

Lam, K. H., Li, Z.-Y., Chen, C.-Y., Tomida, K., & Zhao, B. 2019, Monthly Notices of the Royal Astronomical Society, 489, 5326

Lankhaar, B., & Teague, R. 2023, arXiv e-prints, arXiv:2304.07346

Larsson, R., Buehler, S. A., Eriksson, P., & Mendrok, J. 2014, , 133, 445

Lazarian, A. 2007, , 106, 225

Lazarian, A., & Hoang, T. 2007, Monthly Notices of the Royal Astronomical Society, 378, 910

Lazarian, A., & Yuen, K. H. 2018, The Astrophysical Journal, 853, 96

Li, P., Cunningham, A., Gaches, B., et al. 2021, The Journal of Open Source Software, 6, 3771

Li, Z. Y., Banerjee, R., Pudritz, R. E., et al. 2014, in Protostars and Planets VI, ed. H. Beuther, R. S. Klessen, C. P. Dullemond, & T. Henning, 173

Lopez-Rodriguez, E., Dowell, C. D., Jones, T. J., et al. 2020, The Astrophysical Journal, 888, 66

Lucy, L. B. 1999, Astronomy and Astrophysics, 344, 282

Mac Low, M.-M., & Klessen, R. S. 2004, Reviews of Modern Physics, 76, 125

Mac Low, M.-M., Smith, M. D., Klessen, R. S., & Burkert, A. 1998, , 261, 195

Maret, S., Bergin, E. A., & Lada, C. J. 2006, Nature, 442, 425

Mathis, J. S., Rumpl, W., & Nordsieck, K. H. 1977, The Astrophysical Journal, 217, 425

Mazzei, R., Cleeves, L. I., & Li, Z.-Y. 2020, The Astrophysical Journal, 903, 20

McKee, C. F., & Ostriker, E. C. 2007, Annual Review of Astronomy and Astrophysics, 45, 565

McKee, C. F., & Tan, J. C. 2003, The Astrophysical Journal, 585, 850

McMullin, J. P., Waters, B., Schiebel, D., Young, W., & Golap, K. 2007, in Astronomical Society of the Pacific Conference Series, Vol. 376, Astronomical Data Analysis Software and Systems XVI, ed. R. A. Shaw, F. Hill, & D. J. Bell, 127

Mellon, R. R., & Li, Z.-Y. 2008, The Astrophysical Journal, 681, 1356

Mestel, L., & Spitzer, L., J. 1956, Monthly Notices of the Royal Astronomical Society, 116, 503

Mignon-Risse, R., González, M., Commerçon, B., & Rosdahl, J. 2021, Astronomy and Astrophysics, 652, A69

Morgan, L. K., Moore, T. J. T., Allsopp, J., & Eden, D. J. 2013, Monthly Notices of the Royal Astronomical Society, 428, 1160

Motte, F., Bontemps, S., & Louvet, F. 2018, Annual Review of Astronomy and Astrophysics, 56, 41

Mouschovias, T. C., & Spitzer, L., J. 1976, The Astrophysical Journal, 210, 326

Myers, P. C., Goodman, A. A., Gusten, R., & Heiles, C. 1995, The Astrophysical Journal, 442, 177

Nakamura, F., & Li, Z.-Y. 2005, The Astrophysical Journal, 631, 411

—. 2008, The Astrophysical Journal, 687, 354

Ober, F., Wolf, S., Uribe, A. L., & Klahr, H. H. 2015, Astronomy and Astrophysics, 579, A105

Öberg, K. I., Qi, C., Fogel, J. K. J., et al. 2011, The Astrophysical Journal, 734, 98

Offner, S. S. R., Klein, R. I., McKee, C. F., & Krumholz, M. R. 2009, The Astrophysical Journal, 703, 131

Ostriker, E. C., Stone, J. M., & Gammie, C. F. 2001, The Astrophysical Journal, 546, 980

Pickett, H. M., Poynter, R. L., Cohen, E. A., et al. 1998, , 60, 883

Piétu, V., Dutrey, A., & Guilloteau, S. 2007, Astronomy and Astrophysics, 467, 163

Pillai, T., Kauffmann, J., Wiesemeyer, H., & Menten, K. M. 2016, Astronomy and Astrophysics, 591, A19

Planck Collaboration, Ade, P. A. R., Aghanim, N., et al. 2015a, Astronomy and Astrophysics, 576, A105

—. 2015b, Astronomy and Astrophysics, 576, A105

—. 2016, Astronomy and Astrophysics, 594, A19

Planck Collaboration Int. XIX. 2015, A&A, 576, A104

Planck Collaboration Int. XXXV. 2016, A&A, 586, A138

Purcell, E. M. 1979, The Astrophysical Journal, 231, 404

Reissl, S., Wolf, S., & Brauer, R. 2016, Astronomy and Astrophysics, 593, A87

Ripple, F., Heyer, M. H., Gutermuth, R., Snell, R. L., & Brunt, C. M. 2013, Monthly Notices of the Royal Astronomical Society, 431, 1296

Romanova, M. M., Ustyugova, G. V., Koldoba, A. V., & Lovelace, R. V. E. 2012, Monthly Notices of the Royal Astronomical Society, 421, 63

Scalo, J. M. 1985, in Protostars and Planets II, ed. D. C. Black & M. S. Matthews, 201–296

Schöier, F. L., van der Tak, F. F. S., van Dishoeck, E. F., & Black, J. H. 2005, Astronomy and Astrophysics, 432, 369

Segura-Cox, D. M., Looney, L. W., Stephens, I. W., et al. 2015, The Astrophysical Journal Letters, 798, L2

Shu, F. 1991, The Physics of Astrophysics: Gas dynamics, Series of books in astronomy (University Science Books)

Shu, F. H., Adams, F. C., & Lizano, S. 1987, Annual Review of Astronomy and Astrophysics, 25, 23

Simon, J. B., Bai, X.-N., Armitage, P. J., Stone, J. M., & Beckwith, K. 2013, The Astrophysical Journal, 775, 73

Soler, J. D., & Hennebelle, P. 2017, Astronomy and Astrophysics, 607, A2

Soler, J. D., Hennebelle, P., Martin, P. G., et al. 2013, The Astrophysical Journal, 774, 128

Soler, J. D., Ade, P. A. R., Angilè, F. E., et al. 2017, Astronomy and Astrophysics, 603, A64

Stephens, I. W., Looney, L. W., Kwon, W., et al. 2014, Nature, 514, 597

Stephens, I. W., Yang, H., Li, Z.-Y., et al. 2017, The Astrophysical Journal, 851, 55

Stone, J. M., Gardiner, T. A., Teuben, P., Hawley, J. F., & Simon, J. B. 2008, The Astrophysical Journal Supplement Series, 178, 137

Stone, J. M., Tomida, K., White, C. J., & Felker, K. G. 2020, The Astrophysical Journal Supplement Series, 249, 4

Suriano, S. S., Li, Z.-Y., Krasnopolsky, R., & Shang, H. 2017, Monthly Notices of the Royal Astronomical Society, 468, 3850

Tan, J. C., Shaske, S. N., & Van Loo, S. 2013, in IAU Symposium, Vol. 292, Molecular Gas, Dust, and Star Formation in Galaxies, ed. T. Wong & J. Ott, 19–28

Tazaki, R., Lazarian, A., & Nomura, H. 2017, The Astrophysical Journal, 839, 56

Tazzari, M., Testi, L., Ercolano, B., et al. 2016, Astronomy and Astrophysics, 588, A53

Teague, R. 2019, The Journal of Open Source Software, 4, 1632

Terebey, S., Shu, F. H., & Cassen, P. 1984, The Astrophysical Journal, 286, 529

Tomida, K., & Stone, J. M. 2023, The Astrophysical Journal Supplement Series, 266, 7

Troland, T. H., & Crutcher, R. M. 2008, The Astrophysical Journal, 680, 457

Troland, T. H., & Heiles, C. 1982, The Astrophysical Journal Letters, 260, L19

Tu, Y., Li, Z.-Y., Lam, K. H., Tomida, K., & Hsu, C.-Y. 2023, arXiv e-prints, arXiv:2307.16774

Turk, M. J., Smith, B. D., Oishi, J. S., et al. 2011, The Astrophysical Journal Supplement Series, 192, 9

Turner, N. J., Fromang, S., Gammie, C., et al. 2014, in Protostars and Planets VI, ed. H. Beuther, R. S. Klessen, C. P. Dullemond, & T. Henning, 411

Tychoniec, Ł., van Dishoeck, E. F., van't Hoff, M. L. R., et al. 2021, Astronomy and Astrophysics, 655, A65

Verschuur, G. L. 1968, , 21, 775

Vlemmings, W. H. T., Lankhaar, B., Cazzoletti, P., et al. 2019, Astronomy and Astrophysics, 624, L7

Ward-Thompson, D., Pattle, K., Bastien, P., et al. 2017, The Astrophysical Journal, 842, 66

Xu, S., Ji, S., & Lazarian, A. 2019, The Astrophysical Journal, 878, 157

Yang, H., Li, Z.-Y., Looney, L., & Stephens, I. 2016, Monthly Notices of the Royal Astronomical Society, 456, 2794

Yang, H., Li, Z.-Y., Stephens, I. W., Kataoka, A., & Looney, L. 2019, Monthly Notices of the Royal Astronomical Society, 483, 2371

Yen, H.-W., Koch, P. M., Hull, C. L. H., et al. 2021, The Astrophysical Journal, 907, 33

Zanni, C., Ferrari, A., Rosner, R., Bodo, G., & Massaglia, S. 2007, Astronomy and Astrophysics, 469, 811

Zweibel, E. G. 1988, The Astrophysical Journal, 329, 384